RICE UNIVERSITY

**Development and Study of Charge Sensors for**

**Fast Charge Detection in Quantum Dots**

by

**Madhu Thalakulam**

A THESIS SUBMITTED
IN PARTIAL FULFILLMENT OF THE
REQUIREMENTS FOR THE DEGREE

**Doctor of Philosophy**

Approved, Thesis Committee:

---

Douglas Natelson, Chair
Associate Professor, Physics and Astronomy

---

Alexander J. Rimberg, Supervisor
Associate Professor, Physics and Astronomy
Dartmouth College, Hanover, NH 03755

---

Junichiro Kono
Associate Professor, Electrical and
Computer Engineering

---

Jason Hafner
Assistant Professor, Physics and Astronomy

Houston, Texas
May 2007

To

*Damodaran, Devaki and Mini*

# ABSTRACT

Development and Study of Charge Sensors for
Fast Charge Detection in Quantum Dots

by

Madhu Thalakulam

Charge detection at microsecond time-scales has far reaching consequences in both technology and in our understanding of electron dynamics in nanoscale devices such as quantum dots. Radio-frequency superconducting single electron transistors (RF-SET) and quantum point contacts (QPC) are ultra sensitive charge sensors operating near the quantum limit. The operation of RF-SETs outside the superconducting gap has been a topic of study; the sub-gap operation, especially in the presence of large quantum fluctuations of quasiparticles remains largely unexplored, both theoretically and experimentally. We have investigated the effects of quantum fluctuations of quasiparticles on the operation of RF-SETs for large values of the quasiparticle cotunneling parameter $\alpha = 8E_J/E_c$, where $E_J$ and $E_c$ are the Josephson and charging energies. We find that, for $\alpha > 1$, sub-gap RF-SET operation is still feasible despite quantum fluctuations that wash out quasiparticle tunneling thresholds. Such RF-SETs show linearity and signal-to-noise ratio superior to those obtained when quantum fluctuations are weak, while still demonstrating excellent charge sensitivity.

We have operated a QPC charge detector in a radio frequency mode that allows fast charge detection in a bandwidth of several megahertz. The noise limiting

the sensitivity of the charge detector is not the noise of a secondary amplifier, but the non-equilibrium device noise of the QPC itself. The noise power averaged over a measurement bandwidth of about 10MHz around the carrier frequency is in agreement with the theory of photon-assisted shot noise. Frequency-resolved measurements, however show several significant discrepancies with the theoretical predictions. The measurement techniques developed can also be used to investigate the noise of other semiconductor nanostructures such as quantum dots in the Kondo regime.

A study of the noise characteristics alone can not determine whether the device is operating at the quantum limit; a characterization of back action is also necessary. The inelastic current through a double quantum dot system (DQD) is sensitive to the spectral density of voltage fluctuations in its electromagnetic environment. Electrical transport studies on a DQD system electrostatically coupled to an SET shows qualitative evidence of back-action of SET. The design and fabrication of a few electron DQD device with integrated RF-SET and QPC charge sensors for the study of back action of the sensors and real-time electron dynamics in the DQD are also discussed.

# Acknowledgments

"O Lord, that lends me a life, lend me a heart replete with thankfulness".

–*Shakespere*, *Henry VI – Part 2*.

Alex has been a great advisor. His endless stream of ideas and the passion to do clean and fundamental physics has always been and will be a motivation to me. He has always been approachable, and it is his presence and encouragement, if there is anything, I am going to miss in my future academic life. With great privilege, I thank him for revolutionizing my understanding of experimental mesoscopic physics, and for my metamorphosis from an undergraduate to a post-doctoral candidate.

Prof. Doug Natelson has been always been very helpful with valuable suggestions and also whenever I had some problem with the experimental setups such as dilution fridge or SEM machine, especially in the absence of Alex. I thank him for assuming the responsibility of advisor-of-record when our group moved from Rice university to Dartmouth college, and doing the needful to facilitate my graduation.

Wei and Zhongqing has been terrific collegues. I thank them for showing me the ropes around the lab. Zhongqing has also been a very good friend-in-need whenever I had tough times.

Tim has been a wonderful friend and guide to my North-American cultural expeditions, which to a great extent made me feel home away from home. He has always been available with helping hands and suggestions in and outside the laboratory and I thank him from the bottom of my heart for all the help and

company I enjoyed. I also want to thank Ravi for his helping hands and wonderful company.

Thanks are due to Joel, Weiwei, Feng and Mustafa for their great company, support, and interesting discussions on various topics including physics, during my stay at Dartmouth College. I also thank Joy Sarkar for his company and helping hands in and out side the lab during my stay at Rice. I am also grateful to Martha Alexander for her friendship, hospitality and also for providing moral support on various occasions during my stay at Rice.

This acknowledgment will fall far from complete with out mentioning the help and support received from the machine shop personnel Rich and Fred, electronic shop personnel Dave, and SEM lab personnel Angelo (Rice university) and Chuk (Dartmouth college). They have been always approachable and their suggestions and help played a significant role in making my academic life easier and smoother. Finally I thank all my friends and relatives for making my personal life lot more interesting and joyful.

# Contents


Abstract . . . . . iii

Acknowledgments . . . . . v

List of Figures . . . . . ix

**1 Introduction** **1**

1.1 Two-dimensional electron gas . . . . . 2

1.1.1 Modulation doping, deep level donors and persistent photoconductivity . . . . . 3

1.2 Transport in one dimension . . . . . 9

1.3 Split gate technique & quantum point contacts . . . . . 13

1.4 Quantum dots . . . . . 17

1.4.1 SETs as ultrasensitive electrometers . . . . . 24

1.4.2 Superconducting single electron transistors . . . . . 29

1.4.3 Double quantum dots . . . . . 39

1.5 The RF-SET as a quantum amplifier . . . . . 45

1.6 Double quantum dot broad-band spectrum analyzer . . . . . 47

**2 Experimental Techniques** **52**

2.1 Sample fabrication . . . . . 52

2.1.1 Pattern generation by e-beam lithography . . . . . 53

2.1.2 Shadow evaporation . . . . . 56

2.1.3 Etching . . . . . 56
2.1.4 Ohmic contacts . . . . . 58
2.2 Low temperature techniques . . . . . 60
2.3 Sample wiring . . . . . 64
2.4 Measurement techniques . . . . . 67

**3 Radio-Frequency Superconducting Single Electron Transistor 74**
3.1 Optimizing the charge sensitivity of RF-SET . . . . . 74
3.2 Effect of quantum fluctuations on the performance of radio-frequency superconducting single electron transistor . . . . . 81

**4 Radio-Frequency Quantum Point Contact Charge Sensor 94**

**5 Double Quantum Dot System Coupled to Superconducting Single Electron Transistor for Back-Action Studies 108**
5.1 The story so far . . . . . 108
5.2 New experiments on DQD/RF-SET system . . . . . 112

**6 Conclusion and Future Works 118**

## List of Figures


1.1 Schematic diagram of the conduction band of an n-AlGaAs/GaAs heterostructure showing carrier separation, (a) before (b) after the formation of a 2DEG . . . . . 3

1.2 A plot of lattice constant vs minimum energy gap for various semiconductors. A dashed line indicates an indirect energy gap [6, 7]. . 4

1.3 Configuration coordinate diagram for a Si-doped AlGaAs showing various energy-scales associated with DX centers; adapted from [9]. 7

1.4 Conduction band of a modulation doped GaAs/$Al_xGa_{1-x}As$ heterostructure around the interface. . . . . 8

1.5 Wafer architecture of a typical GaAs/$Al_xGa_{1-x}As$ hetero-structure. 9

1.6 Schematic diagram of the conduction band of a selectively doped GaAs/AlGaAs heterostructure for (a) wider doped region (b) for a thinner doped region for the same dopant concentration [13]. . . . 10

1.7 1D barrier in the middle of a Fermi-sea of electrons with an applied bias $V$ . . . . . 11

1.8 Schematic of a QPC defined by the standard split gate technique. 15

1.9 Potential energy contours of a 1D constriction explaining the quantized conductance. (b) Energy of transverse modes as function of the longitudinal position along the constriction; adapted from[6]. . 16

1.10 Conductance plateaus of a QPC defined by the split gate technique 17

1.11 Schematic diagram of a gated QD weakly coupled to the leads. . . 18
1.12 Potential landscape of QD explaining (a) CB and (b) & (c) single electron tunneling. . . . . 20
1.13 A schematic of CBO of QD. The shaded area represents the range of gate voltages for which the conductance of the QD is sensitive to its electromagnetic environment. . . . . 22
1.14 Temperature dependence of CBO (a) for classical CB for $k_BT/E_c$=0.075 [a] , 0.15 [b], 0.3 [c], 0.4 [d], 1.0 [e] and 2.0 [f] (b) for quantum CB for $k_BT/\triangle E$=0.5 [a], 1.0 [b], 7.5 [c] and 15.0 [d]. [21, 22] . . . . . 23
1.15 (a) Schematic of an SET embedded in a tank circuit (b) corresponding circuit diagram. . . . . 26
1.16 A cartoon of $I$-$V$ curves when the SET in the CB (red) and out of CB (blue) (b) corresponding rf resonance curves. . . . . 28
1.17 Semiconductor style band diagram of an SIS tunnel junction. (a) at the quasi-particle tunneling threshold (b) at the Cooper pair resonance. . . . . 31
1.18 (a) Circuit diagram of a double tunnel junction system. (b) a cartoon of typical $I$-$V$ curves in (red) and out of (blue) CB for an SSET. . . . . 32
1.19 A collection of $I$-$V$ curves of an SSET taken at various gate voltages illustrating various energy scales and sub-gap transport processes. Inset: The supercurrent branch. . . . . 35
1.20 A schematic of (a) JQP and (b) DJQP transport cycles. . . . . 36
1.21 The realization of coupled quantum dot system by split gate geometry 39

1.22 Equivalent circuit of a coupled quantum dot system. . . . . 40

1.23 Schematic stability diagram of a DQD; adapted from [36]. . . . . 43

1.24 (a) A plot of the free energy of the coupled dot system versus the common gate voltage. (b) The conductance through the double dot system when the inter-dot coupling is negligible. (c) The conductance through the dot when the inter-dot coupling is substantial [40] . . . . . 46

1.25 Equivalent circuit of a linear voltage amplifier. $Z_{\text{in}}$ is the input impedance and $Z_{\text{out}}$is the out put impedance. $V_n$ and $I_n$ are the voltage and current noise sources associated with the amplifier; adapted from [23]. . . . . 47

1.26 Inelastic transitions of a two level DQD system showing (a)$\varepsilon < 0$, absorption (b) $\varepsilon > 0$ emission . . . . . 51

2.1 A schematic of the experimental setup of the electron beam lithography. . . . . 53

2.2 Schematic illustration of the fabrication of gold gates by electron-beam lithography. . . . . 55

2.3 Schematic illustration of the fabrication of SET using electron beam lithography followed by shadow evaporation of aluminum. . . . . 57

2.4 (a) Optical micrograph of the device after the fabrication of alignment marks. (b) Optical micrograph of the device after etching. (c) SEM micrograph of the sample after the fabrication of gold gates. (d) SEM micrograph of the final device after the fabrication of an SET. . . . . 59

2.5 A bar chart listing of various techniques used to attain low temperature against various temperature ranges. . . . . 61
2.6 $^3$He/$^4$He phase diagram [46]. . . . . 62
2.7 Schematic diagram of a dilution refrigerator. . . . . 63
2.8 SEM micrographs depicting devices damaged by static electric discharge. (a) and (c) before and (b) and (d) after the discharge. . . 65
2.9 Sample wiring using Indium sandwich technique. (a) SET wiring pads. (b) Stick a small piece of fresh cut indium on to the pads using fine point anti-static tweezers. (c) Stick the wire on to the indium. (d) Press another small piece of indium on to the wire so that he wire is sandwiched between two Indium pieces. (e) A completed DQD/RF-SET device. . . . . 66
2.10 Schematic diagram of the $I$-$V$ measurement setup using four-probe method. . . . . 67
2.11 Schematic diagram of an SET embedded in a tank circuit. . . . . 68
2.12 Schematic diagram of $I$-$V$ measurement setup for devices embedded in the tank circuit. The current measurement is accomplished by measuring the voltage across a standard resistor. . . . . 69
2.13 Schematic diagram of $I$-$V$ measurement setup for devices embedded in the tank circuit using a floating current amplifier. . . . . 70
2.14 Schematic diagram of $I$-$V$ measurement setup for devices embedded in the tank circuit. In this setup the unity gain voltage buffer acts as a floating voltage source . . . . . 71
2.15 Schematic diagram of rf scan setup. . . . . 72

3.1 $I$-$V$ characteristics of SSET with $R_n = 29\text{k}\Omega$. Different curves correspond to different voltages on a nearby gate. . . . . 75

3.2 (a). Reflected rf voltage from the tank circuit while the SSET in CB (blue) and out of CB (red). The vertical dashed-line with arrows represents the frequency of best response. (b) Representative power spectrum of a reflected carrier wave amplitude modulated by a 70kHz voltage oscillation on a nearby gate. . . . . 76

3.3 (a) SNR v/s $V_{\text{dc}}$ with the input rf power optimized for best SNR at each operating point (b) Optimized rf input power v/s $V_{\text{dc}}$ to get the best SNR in (a). (c) $I$-$V$ characteristic of the SSET showing the different sub-gap features. Shaded regions represent the operating points with best SNR. . . . . 78

3.4 False-color plot of dc current through SSET in the $V_{\text{dc}} - Q_0$ plane. Blue dash-line represents the gate voltage at which the SNR is maximum on the DJQP side and the white dashed-line on the JQP side of the $I$-$V$ characteristic. . . . . 80

3.5 (a) Schematic diagram of RF-SET operation. A voltage $v_{\rm in}$ consisting of dc and rf biases $V_{\rm dc}$ and $v_{\rm rf}$ is incident on a tank circuit comprising an inductor $L$, a capacitor $C_p$, and the SET, with junction resistances and capacitances $R_{1(2)}$ and $C_{1(2)}$. A charge oscillation $q_0 cos\omega_m t$ modulates the reflection coefficient $\Gamma$ of the tank circuit and the reflected voltage $v_r$. (b) Post-measurement electron micrograph of S2. Gates G1 and G2 were used vary the SET offset charge. (c) Power spectrum of $v_r$ for $q_0 = 0.063$e rms and $\omega_m/2\pi = 100$ kHz. The charge sensitivity and SNR of the RF-SET were determined from the sideband power and noise floor; the latter, dominated by the white noise of a cryogenic amplifier, was independent of sample, bias, and offset charge. . . . . 83

3.6 $I-V$ characteristics for (a) S1 (b) S2 and (c) S3 (note scale change), were chosen for $Q_0$ showing the DJQP process (red or gray), the JQP process (blue or dark gray), and an intermediate value of $Q_0$ (green or light gray). The arrows and vertical hash mark show the peak-to-peak rf amplitude $2Qv_{\rm rf}$ and dc bias $V_{\rm dc}$ for optimal RF-SET operation. (d) Variation in the measured charging energy $E_c$ relative to the bare charging energy $E_c^o$ for S1 (solid triangle), S2 (circle) and S3 (square). Error bars indicate uncertainty in $E_c^o$. Solid line: theoretical prediction. . . . . 86

3.7 Various JQP cycles. Here J2(1) is on the left (right) and $V_{dc} > 0$. Solid (empty) circles indicate quasielectrons (quasiholes) created during a cycle. The grey circles (white rectangles) indicate the SET island (leads) and their vertical separation the free energy difference for the transition. Cooper pair, quasiparticle, and virtual tunneling are indicated by double, single, and dashed arrows. (a) JQP cycle. Beginning in the state $n = 0$ ($n = 1$), where n is the number of excess electrons on the SET, the transition $0 \rightarrow 1$ ($1 \rightarrow 0$) is allowed, bringing Josephson tunneling through J1(2) into resonance. Cooper pair tunneling $1 \Leftrightarrow -1$ ($0 \Leftrightarrow 2$) is interrupted by QP tunneling through the opposite junction $-1 \rightarrow 0$ ($2 \rightarrow 1$), completing the cycle. (b) DJQP cycle. When Josephson tunneling is resonant for both J1 and J2, transport occurs via the sequence $0 \Leftrightarrow 2$, $2 \rightarrow 1$, $1 \Leftrightarrow -1$, $-1 \rightarrow 0$. (c) Proposed VJQP cycle. If the transition $0 \rightarrow 1$ ($1 \rightarrow 0$) is forbidden, it may still occur virtually. The remaining JQP transitions are allowed for relevant $V_{\rm dc}$. . . . 87

3.8 False color images of $I(V_{\rm dc}, n_g)$ for (a) S2 at T=20mK (b) a simulation at T=200mK assuming an electromagnetic environment with impedance $R_{\rm env} = 50\Omega$ and temperature $T_{\rm env} = 1K$. Cooper pair resonance lines $0 \Leftrightarrow 2$ ($-1 \Leftrightarrow 1$) and QP tunneling thresholds $1 \rightarrow 0$ ($0 \rightarrow 1$) are indicated by the dashed and solid lines. . . . . 90

3.9 Charge sensitivity $\delta q$ and SNR (linear scale) versus $q_0$ in $e$ rms for (a) S1, above gap, (b) S1, subgap, and (c) S3, subgap. Charge sensitivity (solid red symbols) is plotted on the left axis and SNR (open blue symbols) on the right. For reference, the SNR for linear response is plotted as the dashed lines for $\delta q$ measured at the smallest $q_0$. . . . . 92

4.1 Schematic circuit diagram of RF-QPC showing the $LC$ tank circuit and the QPC. Both dc/low-frequency and rf bias can be applied to the sample with the use of a bias tee. A sinusoidal modulation can be applied to either of the gates to modulate the QPC conductance for charge sensitivity measurements. . . . . 95

4.2 (a) Conductance of the QPC vs gate voltage showing well defined plateaus. Inset: Conductance vs gate voltage after shining an LED on the sample. (b) Non-linear transport data showing the differential conductance as a function of $V_{\rm dc}$ and the gate voltage. . . . . 97

4.3 Reflected rf voltage from the tank circuit while the QPC is pinched off (blue) and while the conductance $\approx 0.5G_0$ (red). Inset: Representative power spectrum of reflected carrier wave amplitude modulated by a 97kHz voltage oscillation on one of the QPC gates. The blue curve represents the noise floor of the cryogenic HEMT amplifier. . . . . 98

4.4 (a) Reflected noise power spectrum for $P_n = -98$dBm (red) and -88dBm (green) curve. The blue curve shows the noise floor of the cryogenic HEMT amplifier. Inset: The asymmetry observed for low input powers while the electron concentration/pinch-off voltage was very low. (b) A plot of the noise power integrated over a frequency band of 4.8MHz (blue open circles) and charge oscillation signal $P_s$ induced by a sinusoidal oscillation on one of the QPC gate (red open squares) vs input power $P_{\rm in}$. The red and blue straight lines are a guide to the eye. Inset: Linearity of RF-QPC amplifier; plot of SNR vs input conductance modulation. . . . . 99

4.5 (a) The noise power spectra while the QPC is completely pinched off, (b) while the conductance is $\approx 0.5G_0$ and, (c) while the conductance is $2e^2/h$. (d) Integrated noise power from $P_{\rm in}$=-93dBm (blue) and for -88dBm (green). The amplitude of the rf bias at these two input powers are highlighted by blue and green vertical dashed-lines in Fig. 4.2 (b). . . . . 101

4.6 Nonlinear transport through the QPC at (a) 25 mK, (b) 115 mK, (c) 255 mK, (d) 420 mK, and (e) 550 mK showing differential conductance as a function of drain source voltage $V_{\rm dc}$ for various gate voltages. (f) Conductance vs gate voltage at zero bias for various mixing chamber temperatures as indicated in the plot. The gradual disappearance of the ZBA and the strengthening of 0.7 shoulder with rise in temperature can be noticed. . . . . 103

4.7 (a) Nonlinear transport: Conductance versus the source drain voltage $V_{\rm dc}$ extracted from Fig. 4.6 for QPC conductance $\approx 0.5G_0$ at various mixing chamber temperatures. Inset: QPC conductance showing the pinch-off and the first plateau at 25mK (blue) and 500mK (brown). (b) QPC noise spectra for $P_{\rm in}$=-103dBm for various mixing chamber temperatures. . . . . 105

4.8 (a) Plot of the QPC conductance vs the source drain bias $V_{\rm dc}$ at a few selected gate voltages, at 25mK (blue) and at 550mK (red). (b) The noise power integrated over a narrow band of 150kHz close to the carrier wave vs $P_{\rm in}$ at 550mK. (c) The noise power integrated over a narrow band of 150kHz close to the carrier wave vs $P_{\rm in}$ at 25mK . . . . . 106

5.1 SEM micrograph of DQD/RF-SET device. . . . . 109

5.2 $I$-$V$ characteristics of SSET shown in Fig. 5.1. . . . . 110

5.3 Current through the DQD vs the voltage on the common gate. while SET bias is (a )0.0mV, (b) 0.45mV, (c) 0.65mV, (d)1.25mV. 111

5.4 (a) A plot of current through the SET in the $V_b$-$V_g$ plane. (b) $I$-$V$ characteristics of the SET shown in Fig. 5.8. The arrow-marks are color-coded with the curves in the inset to Fig. 5.6. . . . . 112

5.5 (a) A cartoon showing a few electron DQD. (b) $I$-$V$ characteristics of QD1 showing the 0D levels. (c) $I$-$V$ characteristics of QD2 showing the 0D levels. . . . . 113

5.6 Resonant tunneling current through DQD: dc current through the DQD vs QD1 gate voltage while the SET is biased at various operating voltages as represented by the arrows in Fig. 5.4. The curves are color-coded with the arrows in Fig. 5.4 and are offset in the y-axis for clarity. . . . . 114

5.7 (a) CB oscillations of QD1. (b) Current through the SET vs the voltage on gate D1 while the QD1 is formed for the device shown in Fig. 5.1.(c) Current through the SET vs the voltage on gate D1 while the QD1 is formed for the device shown in Fig. 5.1. The faster oscillations are due to the single electron charging of the QD1 while the slower ones are due to the direct coupling of the gate to the SET.116

5.8 (a) SEM micrograph of the DQD/RF-SET device. (b) An enlarged view of the SET island which shows a break in the antenna coupling the QD1 and the SET. . . . . 117

6.1 An SEM micrograph of the DQD system with integrated SET and QPC charge sensors. . . . . 119

# Chapter 1

## Introduction

The drive to make increasingly miniaturized semiconductor devices coupled with the advent of micro-fabrication and characterization tools over the last few decades saw the emergence of a new area of condensed matter research, namely mesoscopics. Given the fact that the dimensions of these devices are in nanometers it is often referred to as nanoscale physics. Various exciting things happen when the size of a solid is shrunk beyond characteristic lengths such as the mean free path, coherence length or scattering length of the system. By dicing up the dimension one can create basically three classes of system [1]: Two dimensional (2D) such as thin films and two dimensional electron gas (2DEG) [2]; one dimensional (1D) such as nanowires and carbon nanotubes; and zero dimensional (0D) such as quantum dots [3, 4] . The main topics of this thesis will be the 1D and 0D systems. A brief introduction to the 2DEG is given in the next section. The physics of quantum point contacts and quantum dots are dealt with in the successive sections.

## 1.1 Two-dimensional electron gas

A major part of research on mesoscopic physics is based on GaAs/AlGaAs heterostructures in which a thin two-dimensional conducting layer called a two-dimensional electron gas (2DEG) is formed at the interface between GaAs and AlGaAs, as shown in Fig. 1.1 [2, 5, 6]. The band-gap mismatch will cause the electrons to flow from the wider gap n-AlGaAs side to the narrower gap GaAs, exposing the positively charged donors on the AlGaAs side. This positive space charge will cause the bands on either side of the interface to bend, resulting in a sharp triangular well potential for the electrons. The width of this triangular well is very small compared to other length scales in the problem such as the mean free path of the electrons. The electrons are confined to the lowest energy sub-band in the growth direction. So one can regard this as a thin 2D sheet of electrons or two dimensional electron gas (2DEG). This 2DEG is the heart of a class of field effect transistors which goes by many acronyms such as modulation doped field effect transistor (MODFET), high electron mobility transistor (HEMT) etc.

Another example of a 2DEG is the inversion layer in a Si MOSFET. The highest mobility achieved in these devices is about $4\mathrm{m}^2\mathrm{V}^{-1}\mathrm{s}^{-1}$ . The mobility in III-V heterostructures exceeds this value by over three orders of magnitude. The almost perfect crystalline quality of the interface in GaAs/AlGaAs heterostructures, the ability to separate carriers from the dopants and a lower effective mass ($0.067m_e$ in GaAs versus $\approx 0.33m_e$ in Si) are the main reason for these accomplishments.

The active region in a heterostructure is generally at or close to the interface, so a clean, perfectly lattice-matched defect-free interface is very important for attaining a high mobility 2DEG. In silicon MOSFETs the 2DEG forms at the

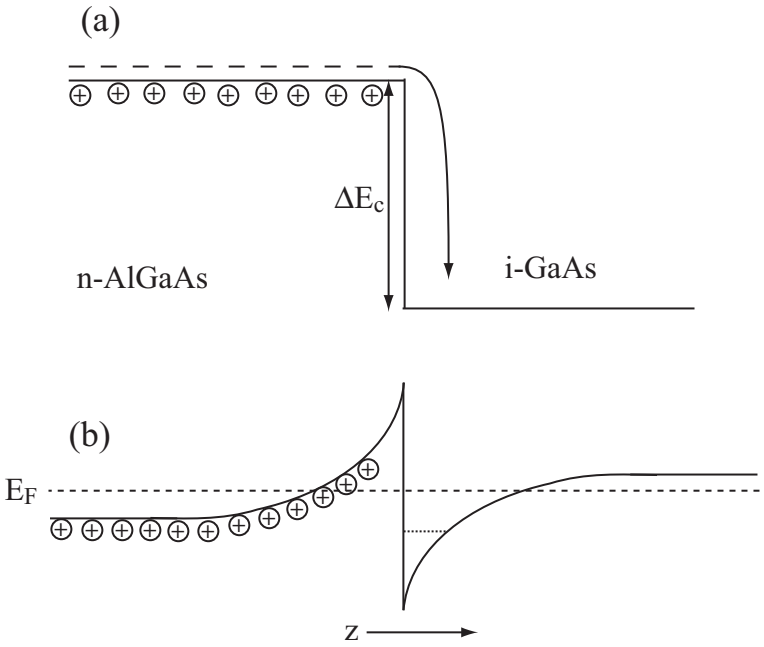


Figure 1.1 Schematic diagram of the conduction band of an n-AlGaAs/GaAs heterostructure showing carrier separation, (a) before (b) after the formation of a 2DEG

interface between Si and the $SiO_2$ interface beneath the gate electrode. It is impossible to get a perfectly lattice matched interface between the amorphous $SiO_2$ and the crystalline Si. In contrast it is clear from Fig. 1.2 why $GaAs/Al_xGa_{1-x}$ heterostructures are so popular: the lattice constant changes by less than 0.15% as a function of $x$ [6].

### 1.1.1 Modulation doping, deep level donors and persistent photoconductivity

The standard way of introducing carriers to a desired region is to introduce dopants in that region. Although this technique works for many devices, it also introduces some undesired effects. The charged donors or acceptors left behind by

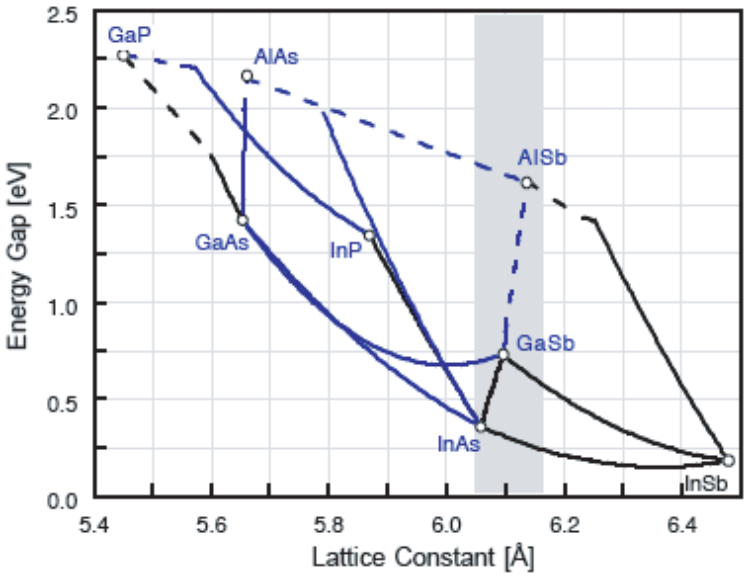


Figure 1.2 A plot of lattice constant vs minimum energy gap for various semiconductors. A dashed line indicates an indirect energy gap [6, 7].

the electrons or holes acts as charged scattering centers and degrade the mobility, blur energy levels, and spoil the interference effects between the electron wave functions which are desired for devices such as resonant tunneling devices. The solution to this problem is modulation or remote doping [6] . In this case the doping region is physically separated from the interface so that the carriers will reside where the scattering effects due to charged donor/acceptor ions are minimal. This situation is schematically represented in Fig. 1.1.

The material is neutral to begin with and flat band conditions are met if the electrons are bound to their respective donors as in Fig. 1.1(a). After being released from the donors, some of the electrons occupy the surface states while the others spill over to the GaAs side. The exposed donors create a space charge layer and the electrostatic potential due to this causes the band to bend on either

side of the interface as in Fig. 1.1(b). The electric field due to the donors pulls the electrons towards the interface and helps to create the triangular well. Modulation doping separates the carries from the donors, which greatly reduces the scattering and enhances the mobility and helps to confine electrons strongly to form the 2DEG.

Generally the donors in a semiconductor can be treated as hydrogenic impurities. By this treatment, in GaAs the binding energy $E_D \approx 5$meV and the radius $a_B \approx 10$nm. But this is not a completely accurate picture. The Si donor in compound semiconductors can also exist in a second deeper state, called DX centers [8–10]. The microscopic structure of these deep donor levels is not well understood. There are two main theories.

1. The deep donor level is a complex formed with the substitutional donor atom (D) and an unknown lattice defect (X), such as an As vacancy.

2. This level is a deep state of the substitutional donor atom that is rigidly linked to the $L$ minimum of the conduction band. According to this model, the selection rule permits the electron emission and capture via the $L$ minimum and the small capture at low temperature is simply because of the energy separation between the $L$ minimum and the bottom of the conduction band.

In $Al_xGa_{1-x}As$, the DX center is the lowest energy state of the donor atom and this level determines the conductivity of the material. The DX center binding energy varies with the alloy composition. Generally speaking, in thermal equilibrium, the free electron concentration at a given temperature is a strong function

of the donor binding energy. This is given by

$$n \simeq \frac{1}{\sqrt{2}} \frac{(N_D N_C)^{1/2}}{2} \exp(-\frac{E_d}{2k_B T}) \tag{1.1}$$

where $N_D,\ N_C,\ E_d,\ k_B$ and $T$ are the donor concentration, effective density of states in the conduction band, donor binding energy, Boltzmann's constant and the temperature in Kelvin respectively [6, 11, 12]. First consider the case of a shallow impurity with a binding energy of about $E_d \approx 10$meV. Most of the donors are ionized at room temperature. The carrier concentration reduces roughly by a factor of 4 when the temperature of the sample is lowered from 300 K through 77 K. On the other hand for a deep donor level, $E_d \approx 100$meV the carrier concentration is about two orders of magnitude lower than the donor atom concentration at room temperature and roughly about six orders of magnitude lower at 77 K. Most often when the material is cooled down to liquid He temperature, almost all the carriers associated with the deep level donors will be tied up with the donors. One obvious way to excite these electrons out of the DX centers is to give them sufficient energy by exposure to light. This is usually accomplished by the use of an infrared or red LED when the sample is cooled down to liquid He temperatures.

Another important property of GaAs/$Al_xGa_{1-x}$As is the persistent photoconductivity observed at low temperature [9]. When the sample is exposed to light at low temperature the DX centers become ionized and the conductivity shows a sharp increase. When the light is turned off the released electrons remain in the conduction band and the conductivity decays only very slowly, in most cases over a period of many days. This is due to the low capture cross-section of the DX centers. This is called persistent photoconductivity and is evidence of the fact

that the sample is not in thermal equilibrium.

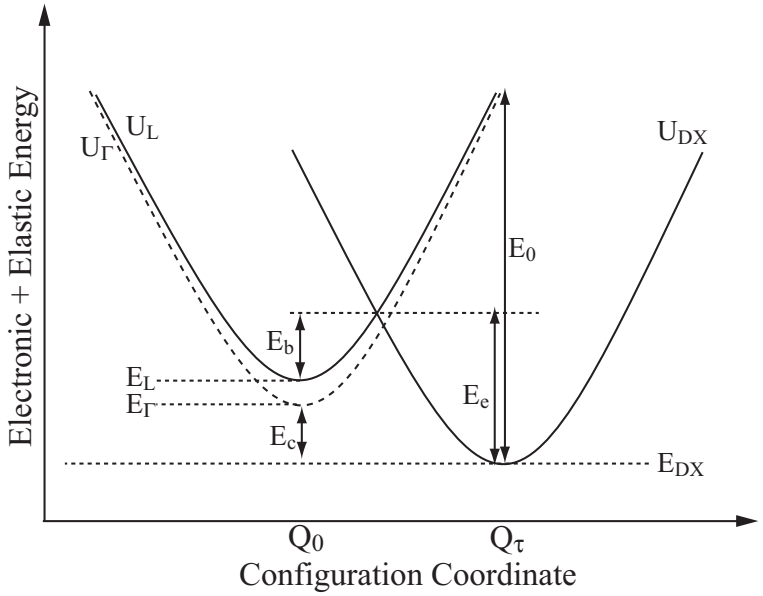


Figure 1.3 Configuration coordinate diagram for a Si-doped AlGaAs showing various energy-scales associated with DX centers; adapted from [9].

The DX center is characterized by four energies which are illustrated in the configuration coordinate diagram Fig. 1.3. The x-axis represents a shift in the configuration around the donor atom. The parabolas on the left centered around $Q_0$ represent the total energy of an electron when it lies in the conduction band and that on the right centered around $Q_\tau$ represents the total energy of the occupied DX center. $E_e$ is the activation energy for the emission of an electron from the DX center and $E_c$ is the activation energy for the capture of an electron from the bottom of the conduction band. $E_0$ is the photoionization energy of the DX center.

The architecture of GaAs/$Al_xGa_{1-x}As$ heterostructure has undergone tremendous changes over the years, thanks to dedicated researchers and technological

improvements in the growth techniques. Most often, the quality of 2DEG is reflected in its electron mobility. This is one area where a lot of progress has been made by the crystal growers over the years. Modulation doping is a major cause of improved carrier mobility in the III-V heterostructure.

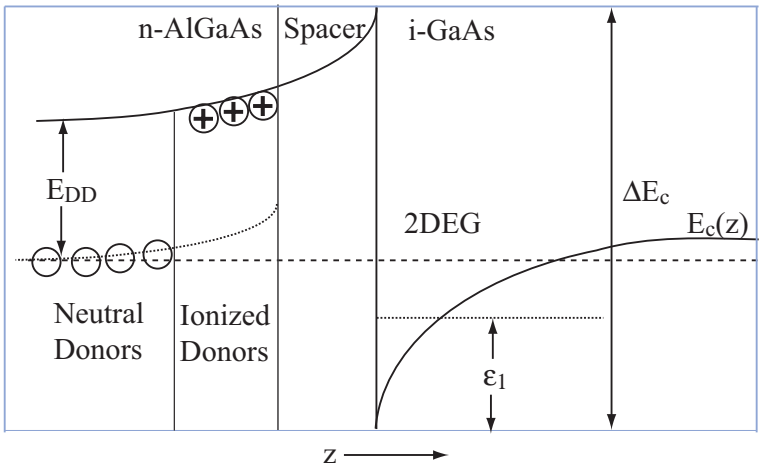


Figure 1.4 Conduction band of a modulation doped GaAs/$Al_xGa_{1-x}As$ heterostructure around the interface.

Fig. 1.5 shows a typical wafer architecture of a GaAs/$Al_xGa_{1-x}As$ heterostructure. One common doping scheme used to improve the electron mobility is $\delta$-doping. As the term suggests, the dopants are incorporated in a very thin layer far away from the interface with a spacer layer of AlGaAs [13].

Fig. 1.6 represents two different dopant distributions and the corresponding conduction band diagrams. Let $z_d$ be the thickness of the doped region and $z_c$ be the distance to the interface from the centroid of the dopant distribution. The doping concentration is given by

$$N_D(z) = \frac{N_D^{2D}}{z_d}[\sigma[z-(z_c-z_d/2)] - \sigma[z-(z_c+z_d/2)]] \tag{1.2}$$

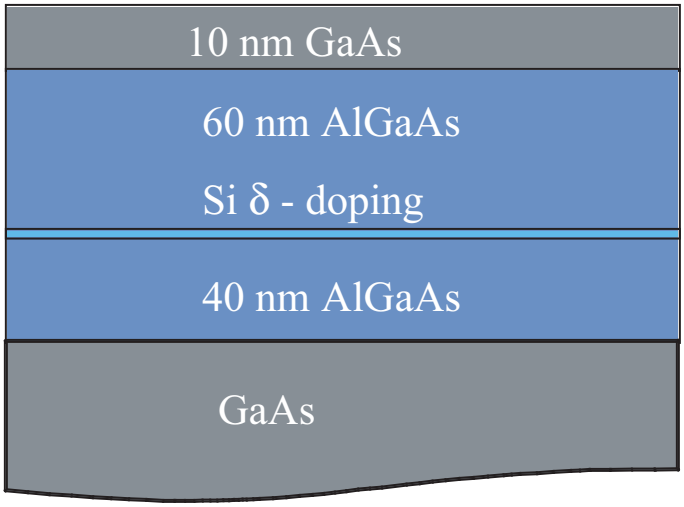


Figure 1.5 Wafer architecture of a typical GaAs/$Al_xGa_{1-x}As$ hetero-structure.

where $\frac{N_D^{2D}}{z_D} = N_D$ is the three dimensional doping concentration and $\sigma(z)$ is the step function. For a given $N_D^{2D}$ this doping concentration results in the same electric field displacement vector for different $z_d$ at the interface providing identical free carrier concentration. The total mean potential fluctuation at the interface due to the randomly distributed positively charged donor ions is minimized as $z_d \rightarrow 0$ or when the doping profile is $\delta$-function-like. This can be seen intuitively: as $z_d$ decreases, the undoped GaAs/$Al_xGa_{1-x}As$ spacer layer thickness increases which in turn reduces the effect of spatial fluctuation of the positively charged donors at the interface. This results in reduced scattering and improved mobility in the 2DEG.

## 1.2 Transport in one dimension

In this section the transport properties of a 1-D system are discussed. First let us consider a one dimensional barrier as shown in Fig. 1.7. The total current

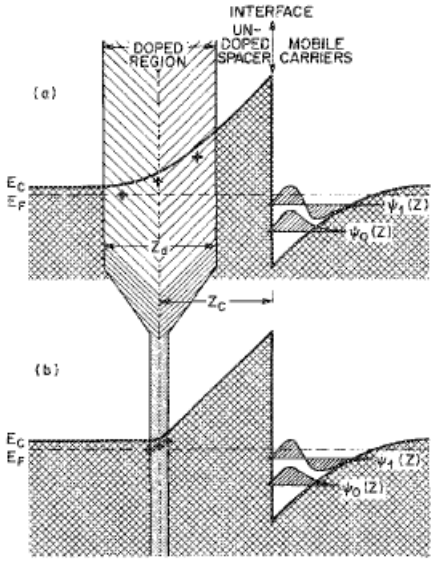


Figure 1.6 Schematic diagram of the conduction band of a selectively doped GaAs/AlGaAs heterostructure for (a) wider doped region (b) for a thinner doped region for the same dopant concentration [13].

through the barrier is the sum of the current from the left lead to the right and right lead to the left. Current due to the electrons from the left lead is given by

$$I_L = 2e \int_0^\infty f[\varepsilon(k), \mu_L] v(k) T(k) \frac{dk}{2\pi}. \tag{1.3}$$

The integral is over all available states in the $k$-space defined by the Fermi function $f[\varepsilon(k), \mu_L]$. Only positive values of the $k$ are considered since we need to consider only those electrons traveling from left to right. $T(k)$ is the transmission probability. Multiplication by $v(k)$ gives the current. The factor 2 in the front accounts for the spin degeneracy.

$$dk = \frac{dk}{dE} dE = \frac{1}{\hbar v} dE. \tag{1.4}$$

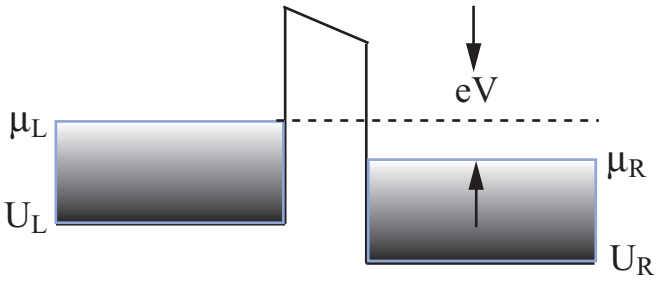


Figure 1.7 1D barrier in the middle of a Fermi-sea of electrons with an applied bias $V$

Inserting this expression into equation (1.3), we have

$$I_L = 2e \int_{U_L}^{\infty} f(E, \mu_L) v T(E) \frac{dE}{2\pi\hbar v} = \frac{2e}{h} \int_{U_L}^{\infty} f(E, \mu_L) T(E) dE. \tag{1.5}$$

The cancellation of the velocity might look a little bit surprising. The states at higher energy have higher velocity, but this contribution is canceled by their reduction in density of states. The expression for the current due to the electrons from the right lead to the left is given by

$$I_R = -\frac{2e}{h} \int_{U_R}^{\infty} f(E, \mu_R) T(E) dE, \tag{1.6}$$

and the expression for the total current is

$$I = I_L + I_R = \frac{2e}{h} \int_{U_L}^{\infty} [f(E, \mu_L) - f(E, \mu_R)] T(E) dE. \tag{1.7}$$

Electrons with energy between $U_R$ to $U_L$ can not contribute to the current since there are no propagating states on the left side corresponding to these values. So the lower limit of both integrals can be taken as $U_L$.

We are interested in calculating the current at small applied bias about the

Fermi level. For small applied bias the difference in the Fermi level can be expanded using a Taylor series, giving.

$$f(E,\mu+\frac{eV}{2})-f(E,\mu-\frac{eV}{2})\approx eV\frac{\partial f}{\partial \mu}=-eV\frac{\partial f(E,\mu)}{\partial E}. \tag{1.8}$$

The current is then given by

$$I=\frac{2e^2V}{h}\int_{U_L}^{\infty}(-\frac{\partial f}{\partial E})T(E)dE. \tag{1.9}$$

In this limit the current is proportional to the voltage across the conductor and the conductance $G=\frac{I}{V}$ is

$$G=\frac{2e^2}{h}\int_{U_L}^{\infty}(-\frac{\partial f}{\partial E})T(E)dE. \tag{1.10}$$

The prefactor $\frac{e^2}{h}=38.7\mu S$ is often referred to as the quantum of conductance and its inverse $\frac{h}{e^2}=25.8k\Omega$ as the resistance quantum $R_K$. At low temperature, the Fermi function is very sharp, and it is safe to assume $-\frac{\partial f}{\partial E}=\delta(E-\mu)$. This will reduce the above integral to

$$G=\frac{2e^2}{h}T(\mu). \tag{1.11}$$

In general, $T$ is the T-matrix whose elements are of the form $t_{mn}$ where $t_{mn}$ defines the contribution from the electrons injected in a mode $n$ but ending up in the mode $m$. Then the total conductance is given by summing over all the input and output modes,

$$G = \frac{2e^2}{h} \sum_m \sum_n |t_{nm}|^2 . \tag{1.12}$$

One can use the Hermitian conjugate matrix of $t$ given by $(t^\dagger)_{mn} = (t)^*_{nm}$ to write the above relation in a more compact form

$$G = \frac{2e^2}{h} \sum_{m,n} t_{nm} t^*_{nm} = \frac{2e^2}{h} \sum_{m,n} (t)_{nm} (t^\dagger)_{mn} = \frac{2e^2}{h} \sum_n (tt^\dagger)_{nn} = \frac{2e^2}{h} Tr(tt^\dagger), \tag{1.13}$$

where 'Tr' stands for the trace of the matrix. This is the outline of the celebrated *Landauer* formalism of conductance in 1-D which will be continued in the next section [5, 6, 14].

## 1.3 Split gate technique & quantum point contacts

As discussed in the first section the width of the triangular well formed at the GaAs/AlGaAs interface is only a few nanometers and the energy spectrum of the electrons in the 2DEG perpendicular to the interface is discrete. At low temperature, only the lowest subband is populated. The electron energy in the 2DEG is given by

$$E(k_x, k_y) = \frac{\hbar^2 (k_x^2 + k_y^2)}{2m^*} \tag{1.14}$$

where $x$ and $y$ are the directions parallel to the interface and $m^*$ is the effective mass of electrons in GaAs which is about $0.067 m_e$. The density of states $\rho$(E) can be deduced from the number density $n(E) = \frac{m^* E}{\pi \hbar^2}$ per unit area,

$$\rho(E) = \frac{dn}{dE} = \frac{m^*}{\pi\hbar^2}. \tag{1.15}$$

This means that the Fermi energy at low temperature is proportional to the sheet density $n_s$:

$$E_F = \frac{n_s}{\rho} \tag{1.16}$$

Now let's examine the change in sheet density due to a metallic gate fabricated on the surface of the wafer. From a simple capacitive coupling model one finds the change in sheet density $\delta n_s$ due to a change in the voltage $\delta v_g$ on the gate is

$$\delta n_s = \frac{\varepsilon\varepsilon_0}{ed}\delta v_g, \tag{1.17}$$

where $\varepsilon$ and the $\varepsilon_0$ are the dielectric permitivity of the GaAs and free space, $d$ is the distance to the 2DEG from the surface, and $e$ is the electronic charge. This demonstrates that the Fermi energy varies linearly with the gate voltage. In other words a negatively biased gate can be used to deplete the 2DEG beneath. This is the essential principle of the split gate technique.

Quantum point contacts (QPC) can be considered as the basic building blocks of split gate geometry devices. A schematic of a typical QPC is shown in Fig. 1.8 [15–17]. The essential idea is to create a constriction in the 2DEG in the $x, y$ plane by applying suitable voltages to the surface gates. Within the constriction the energy spectrum of the electrons is quantized in the direction perpendicular to the constriction while along the constriction the energy levels are unaffected. Confinement in the constriction is best described by a parabolic potential. The

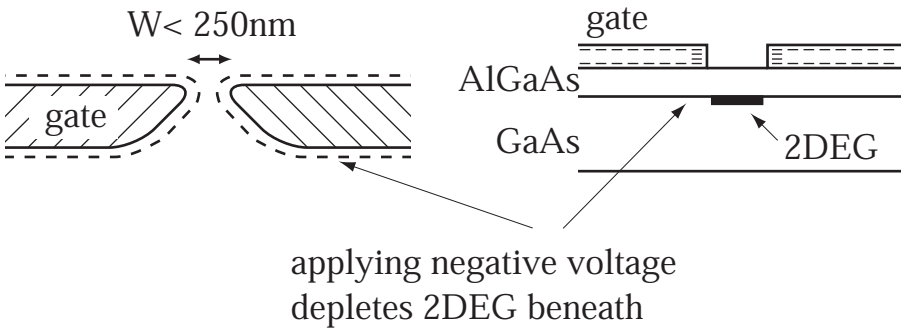


Figure 1.8 Schematic of a QPC defined by the standard split gate technique.

energy spectrum of electrons in the channel is given by

$$E_n = (n + \frac{1}{2})\hbar\omega + \frac{\hbar^2 k_y^2}{2m^*} = \varepsilon_n(x) + \frac{\hbar^2 k_y^2}{2m^*}, n = 0, 1, 2, .... \tag{1.18}$$

The energy of electrons in each sub-band $\varepsilon_n(x)$ defined by Eq. (1.18) varies along the longitudinal position in the constriction. This 1D sub-band energy has a peak at the middle of the constriction. Only those modes which satisfy $\varepsilon_n(x) \leq E$ will pass through constriction. Other modes such as modes 2 and 3 in Fig. 1.9 may tunnel through, but most of the amplitude is reflected [6]. Thus the transmission coefficient is nearly unity for modes defined by $\varepsilon_n(x) \leq E$. The contribution to conductivity from each mode is given by Eq. (1.11). For N propagating modes this is given by

$$G \approx \frac{2e^2}{h} N. \tag{1.19}$$

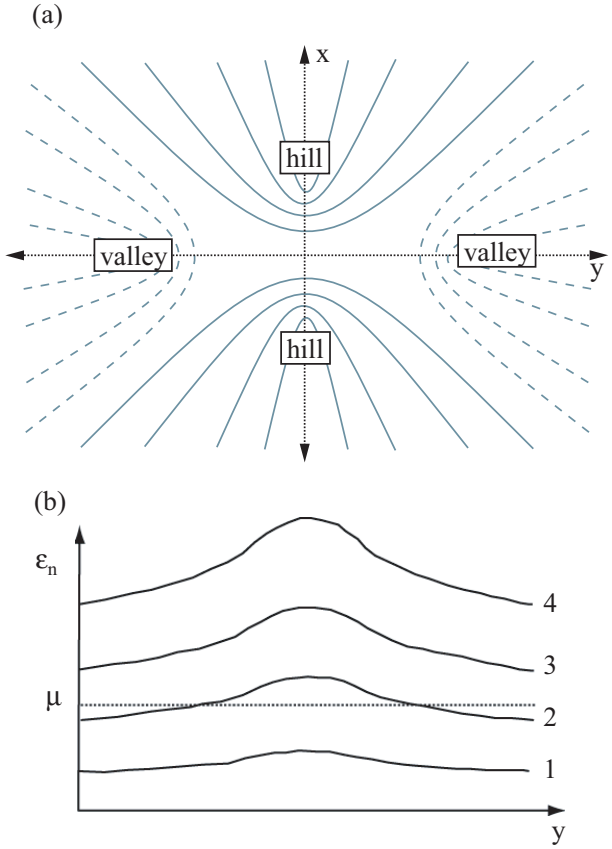


Figure 1.9 Potential energy contours of a 1D constriction explaining the quantized conductance. (b) Energy of transverse modes as function of the longitudinal position along the constriction; adapted from[6].

The conductance through the QPC is quantized in units of $\frac{2e^2}{h}$. A plot of conductance versus gate voltage $V_g$ for a device with a geometry as in Fig. 1.8 should should exhibit step-like behavior in conductance with a step size of $\frac{2e^2}{h}$, as illustrated schematically in Fig. 1.10. In the presence of a magnetic field the spin degeneracy will be lifted and the step size will be $\frac{e^2}{h}$.

The conductance characteristics of a QPC depend on factors such as the tem-

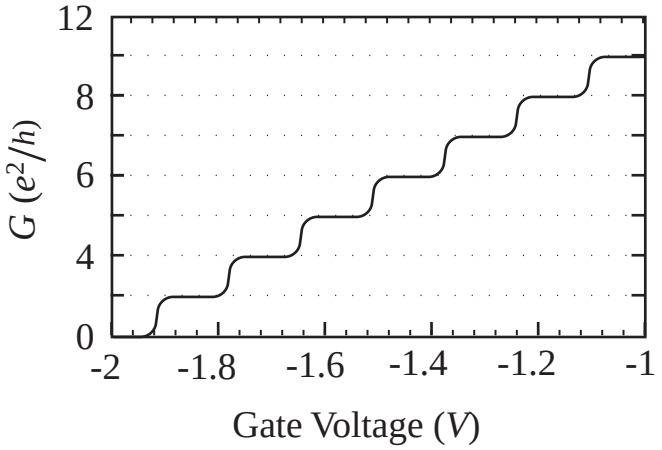


Figure 1.10 Conductance plateaus of a QPC defined by the split gate technique

perature, shape of the gate electrodes, presence of scattering centers, etc. Temperature broadens the energy levels, which in turn will result in a more rounded step edges and less sharp transitions between the steps. This can be easily understood from Fig. 1.9. Modes 2 and 3 do not have enough energy to accomplish ballistic transport through the QPC, but they can contribute to the current via tunneling or thermal activation. As a result, the contribution to the current due to the electrons in mode 2 will be significant at higher temperature due to thermal activation.

## 1.4 Quantum dots

Quantum dots (QD) are small (sub-micron) regions of semiconductors or metals that are electrically isolated from one or more electrodes by thin barriers [18–20]. They are quasi-zero dimensional structures for which the relevant length

scales in the system such as the de Broglie wave length or mean free path of the electrons well exceed the lateral dimensions. Quantum dots usually contain a few to a few thousands of conduction electrons. The simplest example of a quantum dot is a metallic granule sitting on a surface and isolated by a thin insulating coating. Fig. 1.11 is a pictorial representation of a QD weakly coupled to source and drain contacts. When there is no coupling to the source and drain leads, number of electrons on the dot is quantized. When tunneling occurs the number of electrons on the island fluctuates. The energy required to add an electron on to the quantum dot is given by the charging energy

$$E_c = \frac{e^2}{C_\Sigma}, \tag{1.20}$$

where $C_\Sigma$ is the total self capacitance of QD and $E_c$ is called the charging energy. The question one would ask at this point is what are the effects of this charging energy and under what circumstances it is significant? In other words, how small and cold must the QD be to observe its effects?

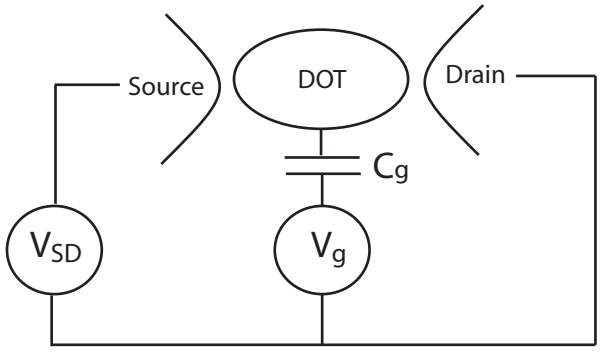


Figure 1.11 Schematic diagram of a gated QD weakly coupled to the leads.

To observe the effect of charging energy, we need to lower the thermal energy of the system. The first requirement is

$$\frac{e^2}{C_\Sigma} \gg k_B T. \tag{1.21}$$

This criterion may be met by making the dot smaller since the total capacitance of the dot is proportional to its dimensions: $C = 4\pi\epsilon_r\epsilon_0 R$ for a sphere and $C = 8\epsilon_r\epsilon_0 R$ for a disc. While this first criterion comes from classical electrostatics, the second comes from quantum mechanics. To observe the charging effects the number of electrons on the QD should be well-defined; the effect of quantum fluctuations in the charge should be minimal. This requirement translates into a restriction on the tunneling resistance of the barriers connecting to the leads as follows. From the Heisenberg uncertainty relation $\triangle E \triangle t > h$. In this situation $\triangle E$ is the charging energy and $\triangle t$ is the time constant of the tunnel junctions $R_t C$, where $R_t$ is the normal resistance of the tunnel junctions. To observe charging effects the energy uncertainty should be much smaller than the charging energy,

$$\begin{aligned} \triangle E \triangle t &= \frac{e^2}{C_\Sigma} > h, \text{ which gives} \\ R_t &\gg \frac{h}{e^2} = 25.813\text{k}\Omega. \end{aligned} \tag{1.22}$$

The tunneling of electrons in and out of the QD changes the potential energy of the island in a discrete manner. One can also change the electrostatic potential energy of the QD in a continuous manner by changing the potential $V_g$ of a nearby gate which is capacitively coupled to it. Fig. 1.12 represents the potential

landscape of a QD coupled to source and drain leads. $\mu_{\text{left}}, \mu_{\text{dot}}$ and $\mu_{\text{right}}$ are the chemical potentials of the source, QD source and drain respectively and, the source-drain voltage $V_{SD} = (\mu_{\text{left}} - \mu_{\text{right}})/e$.

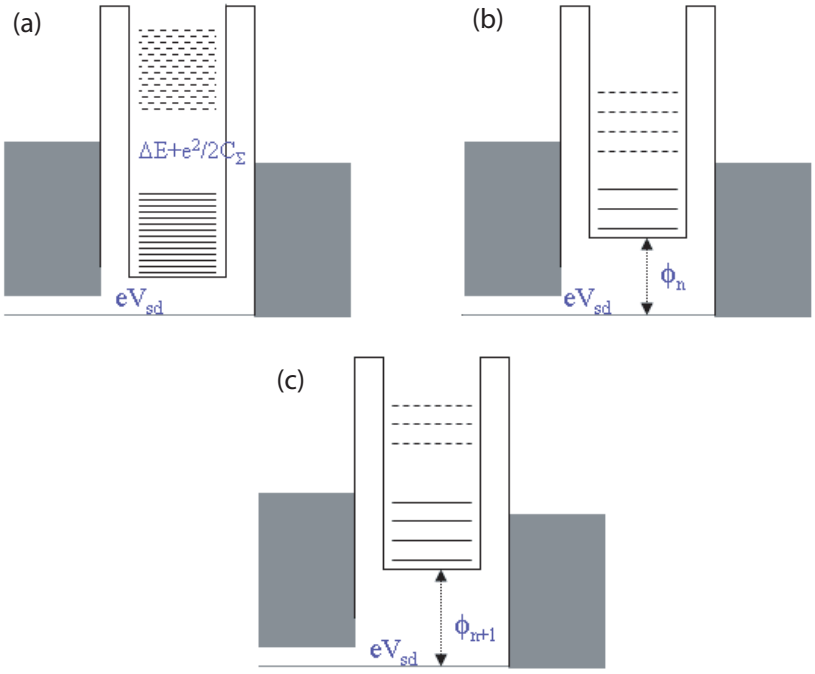


Figure 1.12 Potential landscape of QD explaining (a) CB and (b) & (c) single electron tunneling.

The chemical potential of the dot is given by

$$\mu_{\text{dot}}(N) = E_N + \frac{N - N_0 - 1/2)e^2}{C_\Sigma} - e\frac{C_g}{C_\Sigma}V_g, \tag{1.23}$$

where the first term is the contribution from the single particle nature, the second term comes from the charging energy, and the third term is the charge induced by

a voltage $V_g$ on the gate capacitor. Also $C_\Sigma = C_l + C_r + C_g$, where $C_l, C_r$ and $C_g$ are the capacitance due to the left lead, right lead, and the gate electrode respectively. The energy to add an electron to the QD is given by

$$\mu_{\rm dot}(N+1) - \mu_{\rm dot}(N) = \triangle E + \frac{e^2}{C_\Sigma}, \tag{1.24}$$

where $\triangle E$ is the 0-D level spacing. This non-zero addition energy leads to blockade of current through the QD. Until the applied voltage lifts the Fermi level of the source so as to overcome the charging energy and accommodate an available dot level between the source-drain bias window, the current through the system is blocked resulting in a state called Coulomb blockade [3, 21], as illustrated in Fig 1.12(a). Another way to remove the Coulomb blockade is to align $\mu_{\rm dot}$ between $\mu_l$ and $\mu_r$ by tuning the the gate voltage $V_g$ as in Fig. 1.12(b) and (c). For example, if $\mu_l > \mu_{\rm dot} > \mu_r$ the electron enters the dot from the left lead and leaves to the right sequentially. This is true when the bias $V_{SD} \leq E_c$ . This mode of transport for which the current is carried by discrete charging and discharging is called *single electron tunneling*. Sweeping the gate voltage $V_g$ in either direction will pull down or push up the energy levels in the dot. When there is an energy level in the bias window a peak in the conductance through the system is observed. Sweeping the gate voltage $V_g$ will result in a series of conductance peaks called Coulomb blockade (CB) oscillations, illustrated in Fig 1.13, and the period is given by

$$\triangle V_g = \frac{C_\Sigma}{eC_g}(\triangle E + \frac{e^2}{C_\Sigma}). \tag{1.25}$$

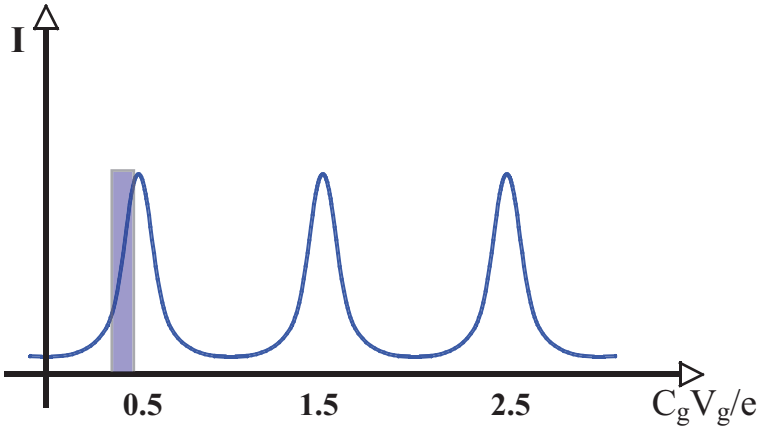


Figure 1.13 A schematic of CBO of QD. The shaded area represents the range of gate voltages for which the conductance of the QD is sensitive to its electromagnetic environment.

The line shape of the CB oscillations depends on the relative magnitude of three energy scales in the problem [22]:

1. If $\frac{e^2}{C_\Sigma} \ll k_BT$, the thermal energy overshadows everything and the discrete nature of the electrons is not observed.

2. For $\triangle E \ll k_BT \ll \frac{e^2}{C_\Sigma}$, we have the classical CB regime for which the effects of 0D levels are absent. This is the situation for metallic quantum dots and relatively large semiconductor quantum dots.

3. For $k_BT \ll \triangle E \ll \frac{e^2}{C_\Sigma}$, we have quantum CB regime for which the single particle level spacing due to size quantization plays a major role in the transport.

One assumption we made in all the above cases is that the quantum mechanical broadening of the energy levels $h\Gamma \ll k_BT$.

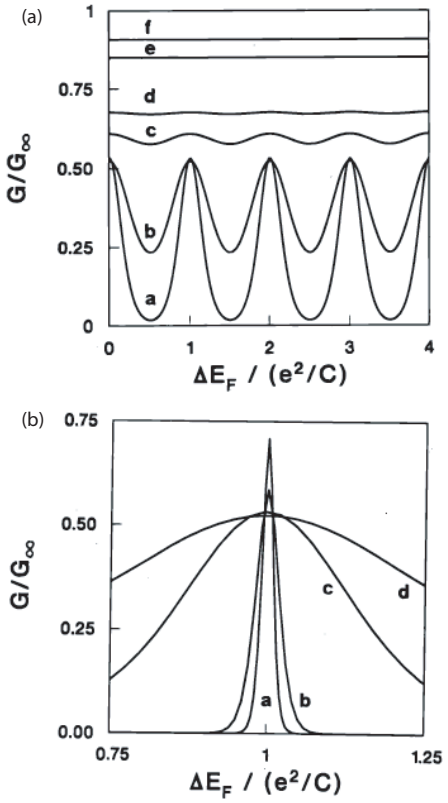


Figure 1.14 Temperature dependence of CBO (a) for classical CB for $k_BT/E_c$=0.075 [a] , 0.15 [b], 0.3 [c], 0.4 [d], 1.0 [e] and 2.0 [f] (b) for quantum CB for $k_BT/\triangle E$=0.5 [a], 1.0 [b], 7.5 [c] and 15.0 [d]. [21, 22]

Classical CB can be described by the *orthodox* Coulomb blockade theory. The line shape of the CB oscillations (CBO) is given by

$$\frac{G}{G_\infty} = \frac{1}{2}\cosh^{-2}(\frac{\delta}{2.5k_BT}) \tag{1.26}$$

where $\delta = e(C_g/C_\Sigma)|V_{g,\mathrm{res}} - V_g|^2$ where $V_{g,\mathrm{res}}$ is the gate voltage corresponding to the peak center, as shown in Fig. 1.14 (a). The width of the peaks is proportional to the temperature. Peak maximum does not change with the temperature and is

half of that at the high temperature limit $G_\infty$. Unlike the high temperature limit, an electron must first tunnel out of the dot for another one to tunnel in at low temperature, which reduces the conductance to one half. The CB oscillations are not visible for $k_BT > 0.3e^2/C_\Sigma$.

In the quantum CB regime the tunneling occurs through a single level and the temperature dependence is illustrated in Fig. 1.14 (b). Single peak conductance is given by

$$\frac{G}{G_\infty} = \frac{\triangle E}{4k_BT}\cosh^{-2}(\frac{\delta}{2k_BT}). \tag{1.27}$$

Unlike in the case of classical CB, the peak height $G_\infty(\triangle E/k_BT)$ decreases linearly with the temperature. Also the maximum peak height is close to $0.75G_\infty$ whereas in the classical case it is $0.5G_\infty$ These are the main differences between the classical and quantum CBO.

From Fig. 1.13 and Eq. 1.26 and 1.27 we can see that the current through the quantum dot coupled to a gate is a strong function of the potential of the gate electrode in analogous to that of field effect transistor. For this reason quantum dots are widely referred to as *single electron transistors*, or in short, SETs.

### 1.4.1 SETs as ultrasensitive electrometers

The detection and study of individual electrons and photons in vacuum is performed routinely by photomultiplier-based detection schemes in atomic physics. Detection of individual electrons in solid state devices has not been possible until the advent of SETs. The conductance of an SET depends on the charge on the gate electrode. Electrometers based on SETs exploit this same property. Charge

sensitivities in the range of $\approx 10^{-5}e/\sqrt{Hz}$ have been achieved routinely which is better by a clear three orders of magnitude compared to FET based electrometers [23]. This basically means that the motion of a charge of about $10^{-5}e$ can be detected in a measurement time of 1sec. In a typical measurement setup the SET is capacitively coupled to the device on which the electrometry is to be performed and the change in the conductance or voltage across of the SET is monitored. Although the SET is intrinsically very sensitive, its relatively large output resistance (about 100k$\Omega$) coupled with the stray capacitance of the wires (about 1nF), which connect the SET to the room temperature electronics limits the operational bandwidth to a few kHz. Performance of the SETs when operated in the low frequency regime is also hampered by the $1/f$ noise caused by background charge motion. Much more can be accomplished if one can detect the charge dynamics in a solid state device in real-time. This can greatly increase our understanding of electronic transport in nanoscale devices, which is currently based on average behavior deduced from conventional voltage and current measurements. This limitation has been cleverly overcome by the new generation of single electron transistors, the so called radio-frequency single electron transistor ( RF-SET) [24–27].

In this more recent generation of devices, an SET is embedded in an $L\,C$ tank circuit consisting of an inductor $L$ and a parasitic capacitance $C$ whose resonant frequency is at least few hundred MHz, as shown in Fig. 1.15 (a). The equivalent circuit is shown in Fig. 1.15 (b). The essential idea is that the reflectance of the tank circuit at resonance is a strong function of the resistance of the SET. Changes in reflected power at resonance can be translated to a change is the conductance of the SET, which in turn gives the information of charge dynamics in the device

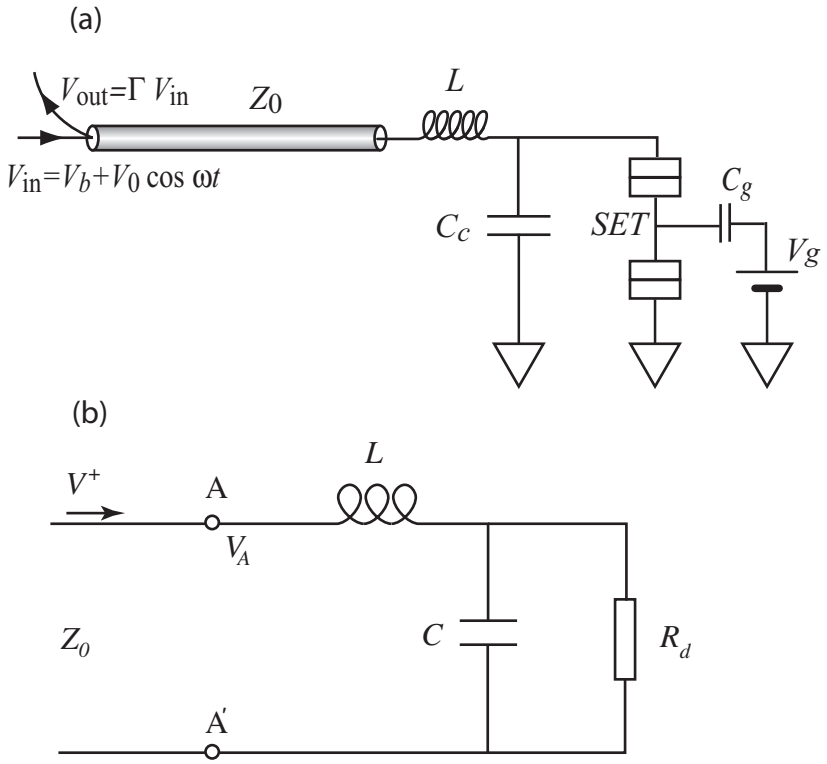


Figure 1.15 (a) Schematic of an SET embedded in a tank circuit (b) corresponding circuit diagram.

to which it is coupled. By choosing appropriate values of the tank circuit elements one can choose a higher operating frequency for the circuit so that the contribution from $1/f$ noise is almost non-existent. In addition, the bandwidth of operation is proportional to the resonant frequency. Cable capacitance in this case does not limit the operational band width as it is a part of the characteristic impedance $Z_0$. In this mode the impedance of this tank circuit at the point AA' is given by

$$\begin{aligned} Z &= i\omega L + \frac{1}{i\omega C + R_d^{-1}} \\ &= \frac{R_d}{1+\omega^2 C^2 R_d^2} + i\frac{\omega L - \omega C R_d (1-\omega^2 CL) R_d}{1+\omega^2 C^2 R_d^2} \end{aligned} \tag{1.28}$$

At resonance the imaginary part of $Z$ vanishes

$$\frac{\omega L - \omega C R_d (1-\omega^2 CL) R_d}{1+\omega^2 C^2 R_d^2} = 0, \tag{1.29}$$

which gives the resonant frequency

$$\omega_0 = \sqrt{\frac{1}{LC}}\sqrt{1-\frac{L/C}{R_d^2}}. \tag{1.30}$$

For typical values of $L$ , $C$ , and $R_d$ , $L/C \ll R_d^2$ and we can write the resonant frequency

$$\omega_0 = \sqrt{\frac{1}{LC}}. \tag{1.31}$$

The reflectance of this tank circuit at the point AA' is given by

$$\Gamma = \frac{Z - Z_0}{Z + Z_0}, \tag{1.32}$$

where $Z_0 = \sqrt{L_0/C_0}$ is the characteristic impedance of the cable where $L_0$ and $C_0$ are the cable inductance and capacitance respectively. Fig. 1.16 is a cartoon showing the essential idea behind the RF-SET. The red and blue curves in Fig. 1.16 (b) are the reflection coefficient of the tank circuit when the SET is in and outside

CB as represented in Fig. 1.16(a).

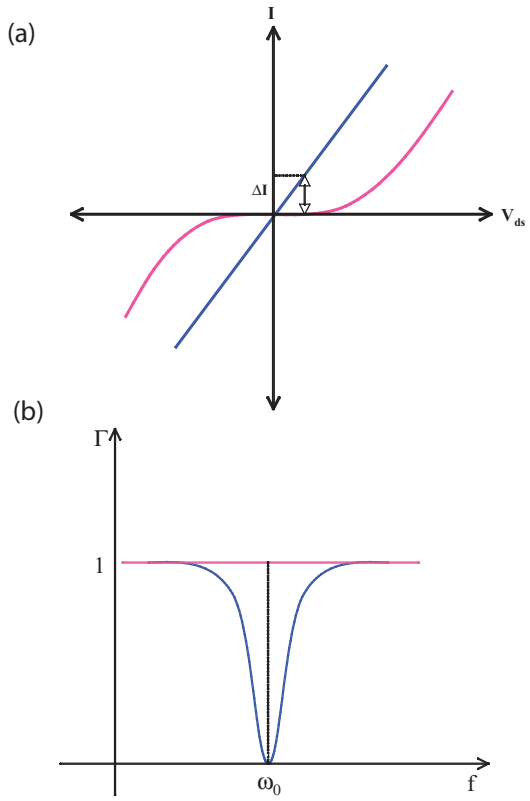


Figure 1.16 A cartoon of $I$-$V$ curves when the SET in the CB (red) and out of CB (blue) (b) corresponding rf resonance curves.

There are various design considerations one has to make when choosing the tank circuit parameters, $L$, $C$ and $R_d$. On most occasions the optimal operating frequency is determined by the cryogenic amplifier and other rf circuit elements sitting outside the tank circuit. The main focus is to operate the tank circuit with the highest possible $Q$ while maintaining a very good impedance matching between the tank circuit and the coaxial feedline of impedance $Z_0$. The tank circuit impedance at resonance is given by

$$Z = \frac{L}{CR_d} \tag{1.33}$$

and the $Q$ of the tank circuit is given by

$$Q = \frac{\sqrt{\frac{L}{C}}}{Z_0}. \tag{1.34}$$

One can see that $Q$, $\omega_0$ and $Z$ are interrelated. In practice, meeting all the requirements is a very involved problem.

### 1.4.2 Superconducting single electron transistors

One main variant of an RF-SET is its superconducting counterpart where the SET is made of superconducting materials. The operation is very similar to that for normal metal RF-SETs. The $I$-$V$ curve of a superconducting SET (SSET) has various resonant current features which makes the rf operation and noise characteristics more interesting, which forms one of the main topics discussed in this work. A brief discussion of the SSET is essential to understand the operation of radio frequency superconducting single electron transistors.

First, let us look a the transport through a normal metal/insulator/metal tunnel junction [28, 29]. Current through a normal metal/insulator/metal (NIN) tunnel junction is given by the tunneling rates. For a single tunnel junction, the tunneling rate from left to right is given by

$$\Gamma_{L\to R} = \frac{\pi}{\hbar}|T|^2 \int_{-\infty}^{\infty} \underbrace{N_L(E)f(E)}_{number\ of\ occupied\ states} \underbrace{N_R(E+eV)[1-f(E+eV)]}_{number\ of\ empty\ states} dE \quad (1.35)$$

where $|T|$ is the amplitude of the tunneling matrix element. One can write a similar equation for $\Gamma_{R\to L}$. The total current through the junction is given by

$$I_N(V) = \frac{\pi}{\hbar}|T|^2 \int_{-\infty}^{\infty} N_L(E)N_R(E+eV)[f(E)-f(E+eV)]dE. \quad (1.36)$$

This is for a normal metal tunnel junction. In a superconductor the quasiparticles are separated from the Cooper pairs by an energy gap, the superconducting gap $\triangle$. Fig. 1.17 shows a semiconductor model band diagram of SIS tunnel junction system. For a superconductor, number density of states is given by

$$\frac{N_s(E)}{N(0)} = \frac{|E|}{\sqrt{E^2-\triangle^2}} \quad (1.37)$$

for $|E| > \triangle$ and

$$\frac{N_s(E)}{N(0)} = 0 \quad (1.38)$$

for $|E| < \triangle$. The current through an SIS junction is given by

$$I_s(V) = \frac{1}{R_N e}\int_{-\infty}^{\infty} \frac{E}{\sqrt{E^2-\triangle^2}} \frac{E}{\sqrt{(E+eV)^2-\triangle^2}}[f(E)-f(E+eV)]dE \quad (1.39)$$

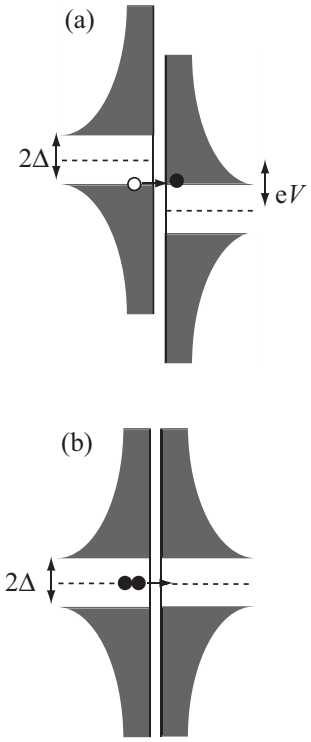


Figure 1.17 Semiconductor style band diagram of an SIS tunnel junction. (a) at the quasi-particle tunneling threshold (b) at the Cooper pair resonance.

For a double junction system when the junction resistance $R > R_K$ charging effects will come into play. At T=0 no current will flow until the bias voltage $eV > 4\triangle$. For $4\triangle < eV < 4\triangle + eV$ the quasi-particles will exhibit charging effects.

Fig. 1.18 (a) is an SSET circuit diagram and Fig. 1.18 (b) is a cartoon of representative $I$-$V$ curves exhibiting various energy scales in the problem. The lower bound for the junction resistance to observe the charging effects is determined by the energy time uncertainty relation, $\triangle E\tau > \hbar$. For an SIS junction $\tau = \frac{1}{\Gamma}$ is the time taken by the quasiparticle to tunnel through the junction and $\Gamma$ is

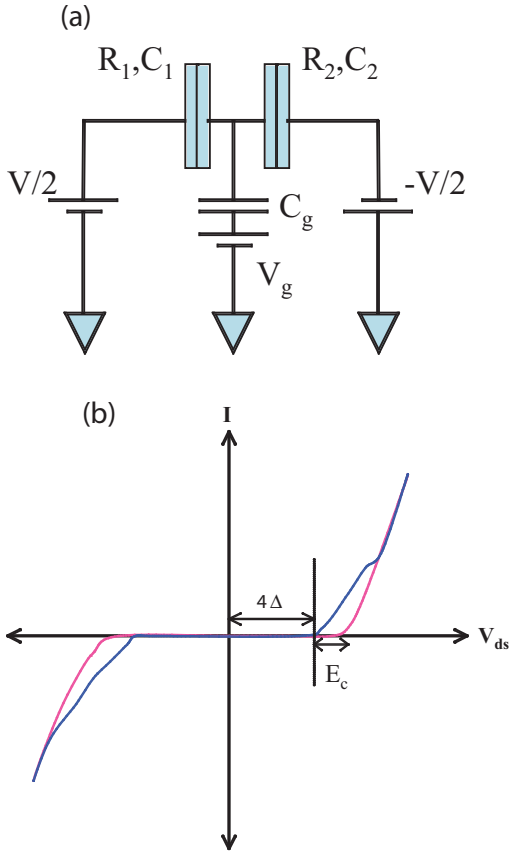


Figure 1.18 (a) Circuit diagram of a double tunnel junction system. (b) a cartoon of typical $I$-$V$ curves in (red) and out of (blue) CB for an SSET.

the quasiparticle tunneling rate. The onset of quasiparticle tunneling is around $eV \approx 2\triangle$, so

$$I_{qp} = \frac{2\triangle}{eR_i} \tag{1.40}$$

$$\tau = \frac{1}{\Gamma} = \frac{e}{I_{qp}} = \frac{e^2 R_i}{2\triangle} \tag{1.41}$$

$$\triangle E\tau = \frac{E_c e^2 R_i}{2\triangle} > \hbar, \tag{1.42}$$

where $R_i$ is the resistance of a single junction. The condition for observing charging effects is

$$\frac{E_c e^2 R_i}{2\triangle\hbar} > 1 \tag{1.43}$$

or

$$R_i > \frac{2\hbar}{e^2}\frac{\triangle}{E_c}. \tag{1.44}$$

According to a more precise result, [30, 31] the parallel resistance of both junctions is

$$(\frac{1}{R_1} + \frac{1}{R_2})^{-1} = R_\| > \frac{\pi\hbar}{e^2}\frac{\triangle}{E_c}. \tag{1.45}$$

For a symmetric SSET $R_1 = R_2 = R_N = 2R_\|$ and

$$R_N > 4\frac{\triangle}{E_c}R_Q \tag{1.46}$$

where $R_Q = \frac{h}{4e^2}$ is the resistance quantum for Cooper pairs.

According to the above relation the normal state resistance of an SSET must be $4\frac{\triangle}{E_c}$ times $R_Q$ to exhibit charging effects. For most of the samples discussed in this report $\triangle/E_c \approx 1$ and this does not bring any drastic effects. For SSETs with higher charging energies this relation allows one to reduce the resistance of the junctions below the resistance quantum $R_K$. This turns out to be very important for the rf operation of these devices due to the following facts:

1. Low junction resistances: This will result in a better impedance matching of the tank circuit to rest of the rf circuit.

2. A second consequence is that a lower resistance SET will give higher current modulation as the current scales inversely with the resistance. This will result in a better charge sensitivity.

Now let's try to look at the energetics of both Cooper pair and quasi-particle tunneling thresholds of a symmetrically biased SSET. Fig 1.18 (a) is a circuit diagram of a double tunnel junction system. The three capacitors form a voltage divider and the voltage drop across the junctions is given by [29]

$$\kappa_{1,2}eV = \frac{C_{2,1} + C_g/2}{C_\Sigma}eV \tag{1.47}$$

For quasiparticle tunneling the bias voltage must provide enough energy to break the Cooper pairs and should also overcome the charging energy requirements. In short the voltage drop across the junctions should satisfy

$$\kappa_1 eV \geq U(n-1) - U(n) + 2\triangle \tag{1.48}$$

$$\kappa_2 eV \geq U(n+1) - U(n) + 2\triangle \tag{1.49}$$

for quasiparticles, and for Cooper pairs

$$2\kappa_1 eV = U(n-2) - U(n) \tag{1.50}$$

$$2\kappa_2 eV = U(n+2) - U(n) \tag{1.51}$$

where $U(n) = \frac{Q_0 - ne}{2C_\Sigma}$ is the potential energy of the island with $n$ electrons on it. In the case of Cooper pairs the bias voltage exactly compensates the charging energy since Cooper pair tunneling is resonant .

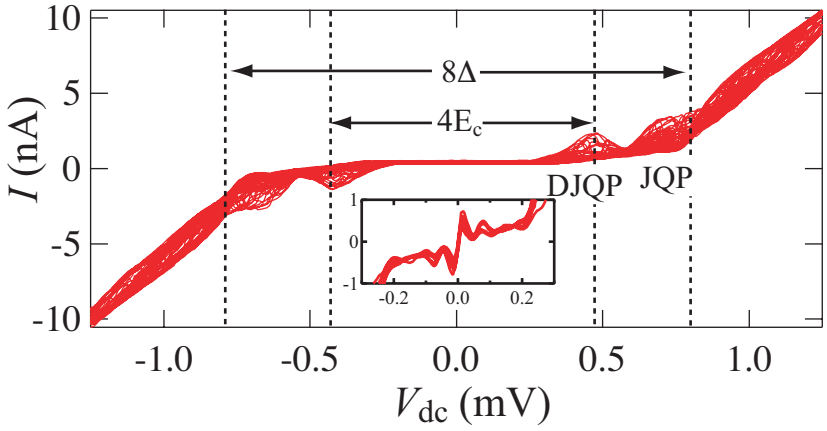


Figure 1.19 A collection of $I$-$V$ curves of an SSET taken at various gate voltages illustrating various energy scales and sub-gap transport processes. Inset: The supercurrent branch.

In actuality, unlike Fig. 1.18, a SIS double junction system also exhibits current structures for voltages less than $4\triangle$ [32]. Fig. 1.19 represents the the $I$-$V$ characteristics of an SSET with $R_N = 58\text{k}\Omega$. Apart from the sharp rise of current outside the superconducting gap, it also exhibits current peaks inside the superconducting gap. These are due to resonant current charge transfer processes involving both quasiparticles and Cooper pairs through the junctions. Sequences of these charge transport processes are schematically represented in Fig. 1.20 (a) and (b).

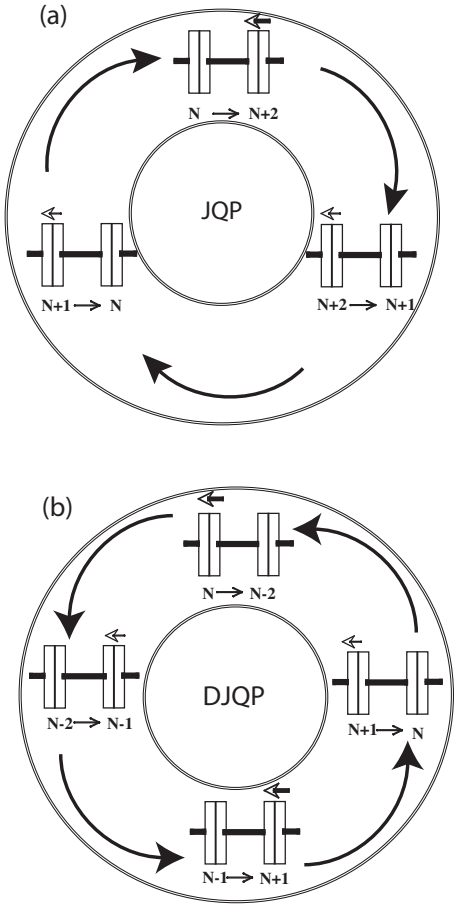


Figure 1.20 A schematic of (a) JQP and (b) DJQP transport cycles.

The processes represented in Fig. 1.20 (a) is called the Josephson quasiparticle cycle or in short JQP cycle [33, 34]. All the three processes must be energetically possible for the JQP cycle to happen. It involves a Cooper pair tunneling event at one junction followed by two quasiparticle tunneling events at the other junction.

For the Cooper pair tunneling off the island

$$2\kappa_1 eV \;=\; U(-2) - U(0) \tag{1.52}$$

$$\kappa_1 eV = 2E_c[1 + \frac{Q_0}{e}]. \quad (1.53)$$

For the next quasiparticle tunneling on to the island

$$\kappa_2 eV \geq U(-1) - U(-2) + 2\triangle \quad (1.54)$$

$$\kappa_2 \geq 2E_c[-\frac{3}{2} - \frac{Q_0}{e}]. \quad (1.55)$$

For the last quasi-particle to tunnel

$$\kappa_2 eV \geq U(0) - U(-1) \quad (1.56)$$

$$\kappa_2 eV \geq 2E_c[-\frac{1}{2} - \frac{Q_0}{e}] \quad (1.57)$$

From the above set of equations one can see that the second quasiparticle tunneling is the constraint. If that event is energetically allowed rest of the processes are allowed. Now let's determine the voltage at which these processes happen for any given value of $n$.

For Cooper pair tunneling

$$2\kappa_1 eV = U(n-2) - U(n) \quad (1.58)$$

$$\kappa_1 eV = 2E_c[1 + (\frac{Q_0}{e} - n)] \quad (1.59)$$

For the second quasiparticle tunneling

$$\kappa_2 eV \geq U(n) - U(n-1) \tag{1.60}$$

$$\kappa_2 eV = 2E_c[-\frac{1}{2} - \frac{Q_0}{e} - n] \tag{1.61}$$

From the last two sets of equations

$$(\kappa_1 + \kappa_2)eV = 2E_c[1 + \frac{Q_0}{e} - \frac{1}{2} - \frac{Q_0}{e}] \tag{1.62}$$

$$eV = E_c + 2\triangle. \tag{1.63}$$

This is the threshold for the JQP cycle.

The second sub-gap transport process happens at a lower bias voltage than the JQP process. It is called double JQP or DJQP process [35] and involves two Cooper pair and two quasi-particle tunneling processes in the sequence illustrated in Fig. 1.20 (b).

The requirement for the first Cooper pair tunneling is same as that of the JQP process, Eq. 1.58. But the second Cooper pair tunneling happens at the other junction and the energetics of that process are given by

$$\kappa_2 eV = U(n+1) - U(n-1) \tag{1.64}$$

$$\kappa_2 eV = 2E_c[1 - (\frac{Q_0}{e} - (n-1))] \tag{1.65}$$

The bias at which the DJQP process occurs is given by

$$(\kappa_1 + \kappa_2)eV = eV = 2E_c. \tag{1.66}$$

According to this result the location of the DJQP peak can be used to determine the charging energy of an SSET.

### 1.4.3 Double quantum dots

A double quantum dot (DQD) [36] can be formed when two quantum dots are coupled together as shown in Fig. 1.21 . One can develop a theoretical treatment of

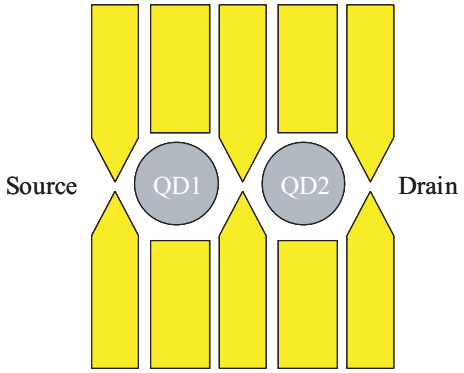


Figure 1.21 The realization of coupled quantum dot system by split gate geometry

transport through the DQD along the same lines as that of the single dot system. The first step is to develop an expression for the electrostatic energy of a coupled quantum dot system. The equivalent circuit of a DQD is shown in Fig. 1.22. We begin with a purely classical description in which the discrete quantum states of the dots are not taken into account. In the linear transport regime for which the bias voltage $V \approx 0$, the double dot electrostatic energy is given by

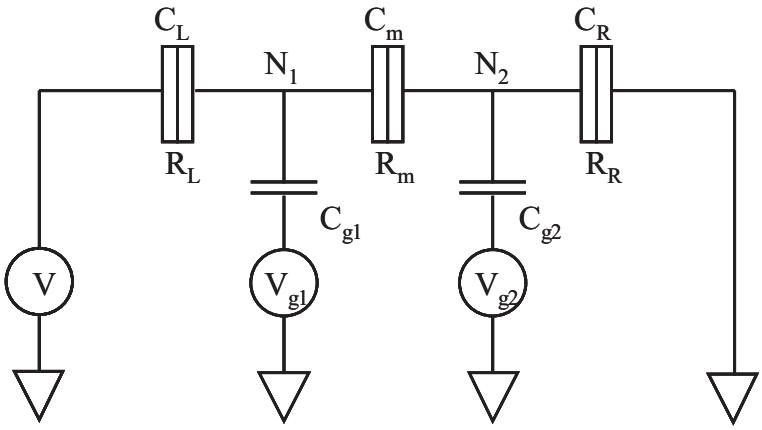


Figure 1.22 Equivalent circuit of a coupled quantum dot system.

$$U(N_1, N_2) = \frac{1}{2}N_1^2 E_{c1} + \frac{1}{2}N_2^2 E_{c2} + f(V_{g1}, V_{g2}). \tag{1.67}$$

where

$$\begin{aligned} f(V_{g1}, V_{g2}) &= \frac{1}{-\mid e \mid}\{C_{g1}V_{g1}(N_1 E_{c1} + N_2 E_{cm}) + C_{g2}V_{g2}(N_1 E_{cm} + N_2 E_{c2})\} \\ &\quad + \frac{1}{e^2}\{\frac{1}{2}C_{g1}^2 V_{g1}^2 E_{c1} + \frac{1}{2}C_{g2}^2 V_{g2}^2 E_{c2} + C_{g1}V_{g1}C_{g2}V_{g2}E_{cm}\} \end{aligned} \tag{1.68}$$

$$E_{C1} = \frac{e^2}{C_1}\left(\frac{1}{1 - \frac{C_m^2}{C_1 C_2}}\right) \tag{1.69}$$

$$E_{C2} = \frac{e^2}{C_2}\left(\frac{1}{1 - \frac{C_m^2}{C_1 C_2}}\right) \tag{1.70}$$

$$E_{Cm} = \frac{e^2}{C_m}\left(\frac{1}{\frac{C_m^2}{C_1 C_2} - 1}\right) \tag{1.71}$$

and $N_1$ and $N_2$ are the number of electrons in the QD1 and QD2 respectively. $E_{c1}$ and $E_{c2}$ are the charging energies of QD1 and QD2 respectively with a correction term which accounts for the coupling and $E_{cm}$ is the electrostatic coupling energy of the dots. When $C_m = 0$, the above equation for the total electrostatic energy reduces to the total energy of two isolated dots,

$$U(N_1, N_2) = \frac{-N_1 \mid e \mid + C_{g1}V_{g1})^2}{2C_1} + \frac{-N_2 \mid e \mid + C_{g12}V_{g2})^2}{2C_2}, \tag{1.72}$$

where $C_1$ and $C_2$ are the total capacitances of the individual dots. The electrochemical potential of QD1 is given by

$$\begin{aligned} \mu_1(N_1, N_2) &= U(N_1, N_2) - U(N_1 - 1, N_2) \\ &= (N_1 - 1/2)E_{c1} + N_2 E_{cm} - \\ &\quad \frac{1}{-\mid e \mid}(C_{g1}V_{g1}E_{c1} + C_{g2}V_{g2}E_{cm}), \end{aligned} \tag{1.73}$$

where $\mu_1(N_1, N_2)$ is defined as the energy needed to add the $N_1^{th}$ electron to the QD1 while the number of electrons on the QD2 remains unaltered. In a similar way, one can define $\mu_2(N_1, N_2)$ as the energy needed to add the $N_2^{th}$ electron to the QD2 keeping the number of electron on the QD1 fixed at $N_1$

$$\begin{aligned} \mu_2(N_1, N_2) &= U(N_1, N_2) - U(N_1 - 1, N_2 - 1) \\ &= (N_2 - 1/2)E_{c2} + N_1 E_{cm} - \\ &\quad \frac{1}{-\mid e \mid}(C_{g1}V_{g1}E_{cm} + C_{g2}V_{g2}E_{c2}), \end{aligned} \tag{1.74}$$

Also one can note that

$$\mu_1(N_1+1,N_2)-\mu_1(N_1,N_2) = E_{c1} \quad (1.75)$$

$$\mu_2(N_1,N_2+1)-\mu_2(N_1,N_2) = E_{c2} \quad (1.76)$$

$$\mu_1(N_1,N_2+1)-\mu_1(N_1,N_2) = \mu_2(N_1+1,N_2)-\mu_2(N_1,N_2) = E_{cm}. \quad (1.77)$$

For a fixed charge configuration on the dots the electrochemical potentials have to be negative. Whenever both electrochemical potentials are equal to or greater than zero the transport is activated through the dot. One can construct a surface plot by observing the above constraint plus the fact that the number of electrons on the dots must be integers. These two constraints together create hexagonal regions in the $(V_{g1}, V_{g2})$ plane within which the charge configuration is stable called the stability diagram. A schematic stability diagram is depicted in Fig. 1.23. The dimensions of this stability diagram can be determined by applying boundary conditions to the electrochemical potentials $\mu_1$ and $\mu_2$:

$$\mu_1(N_1,N_2;V_{g1},V_{g2}) = \mu_1(N_1+1,N_2;V_{g1}+\Delta V_{g1},V_{g2}) \quad (1.78)$$

$$\mu_2(N_1,N_2;V_{g1},V_{g2}) = \mu_2(N_1,N_2+1;V_{g1},V_{g2}+\Delta V_{g2}) \quad (1.79)$$

From these one can obtain

$$\Delta V_{g1} = \frac{\mid e \mid}{C_{g1}} \quad (1.80)$$

$$\Delta V_{g2} = \frac{\mid e \mid}{C_{g2}}. \quad (1.81)$$

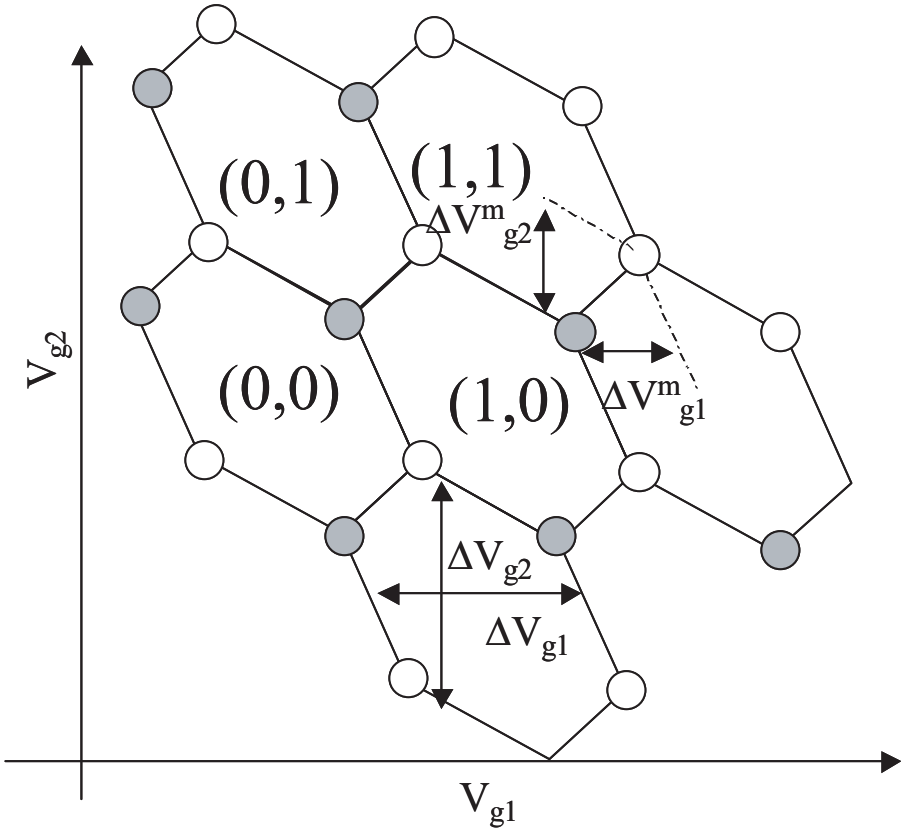


Figure 1.23 Schematic stability diagram of a DQD; adapted from [36].

Also:

$$\mu_1(N_1, N_2; V_{g1}, V_{g2}) = \mu_1(N_1, N_2 + 1; V_{g1} + \Delta V_{g1}^m, V_{g2}) \quad (1.82)$$

$$\mu_2(N_1, N_2; V_{g1}, V_{g2}) = \mu_2(N_1 + 1, N_2; V_{g1}, V_{g2} + \Delta V_{g2}^m), \quad (1.83)$$

which gives

$$\Delta V_{g1}^m = \frac{\mid e \mid C_m}{C_{g1} C_2} = \Delta V_{g1} \frac{C_m}{C_2}, \quad (1.84)$$

$$\Delta V_{g2}^{m} = \frac{\mid e \mid C_m}{C_{g2} C_1} = \Delta V_{g2} \frac{C_m}{C_1}. \tag{1.85}$$

Conductance through series coupled dots is possible when electrons can tunnel through both dots. This is possible only when three charge configurations become degenerate, i.e., when three boundaries in the hexagonal stability diagram meet. These so-called triple points are marked by solid ($\bullet$) and hollow ($\circ$) circles in Fig. 1.23. The transport at these points involves the following charge transfer sequences

$$\bullet \Rightarrow (N_1, N_2) \rightarrow (N_1 + 1, N_2) \rightarrow (N_1, N_2 + 1) \rightarrow (N_1, N_2)$$
$$\circ \Rightarrow (N_1 + 1, N_2 + 1) \rightarrow (N_1 + 1, N_2) \rightarrow (N_1, N_2 + 1) \rightarrow (N_1 + 1, N_2 + 1)$$

To understand the Coulomb blockade oscillations of a coupled dot system we begin by analyzing a symmetric DQD. The electrostatic potential of the DQD can be written as

$$\begin{aligned} E_{DQD} &= \frac{1}{2C_\Sigma(1-\alpha^2)}[(C_{g1}V_{g1} - N_1 e)^2 + (C_{g2}V_{g2} - N_2 e)^2 \\ &\quad +2\alpha(C_{g1}V_{g1} - N_1 e)(C_{g2}V_{g2} - N_2 e)], \end{aligned} \tag{1.86}$$

where $\alpha = C_{int}/C_\Sigma$. First let us assume that there is no electrostatic coupling between the dots so that $\alpha = 0$. If we plot the above formula for a common gate voltage $V_{g1} = V_{g2}$, we get a series of parabolas as shown in Fig. 1.24. It is interesting to note that when the total electron number is even the minimum energy is zero while if it is odd the minimum energy is greater than zero. That is, there is an even odd dependence of the free energy. Transport occurs at only

those points where two parabolas corresponding to adjacent N values cross. When no inter-dot coupling exists one would see a series of equally spaced conductance oscillation as in the case of a single dot. For $\alpha \sim 1$ the even-odd dependence in the total free energy is lifted. In this case the DQD behaves as a big single dot and again one would see periodic oscillation in conductance when the gate voltage is swept. In this case the period is defined by the total gate capacitance of the single big dot. Of particular interest is the intermediate regime for which to the inter-dot barrier is not fully open but not fully closed i.e. $0 < \alpha < 1$. In this regime researchers have already shown both theoretically and experimentally that the conductance peaks are split and, the splitting depends on the inter-dot coupling [37–39] as illustrated in Fig. 1.24.

## 1.5 The RF-SET as a quantum amplifier

As discussed by various researchers the RF-SET is a fast and highly sensitive electrometer operating near the quantum limit. Here we discuss the noise characteristics of the RF-SET. From here onwards the back action of SET is discussed in the context of qubit readout since RF-SET has been regarded as a potential readout device for charge qubits. It is therefor very important to characterize and minimize this back action to prevent loss of information in charge based quantum information processing schemes.

Since the SET is a quantum mechanical device, it is subject to quantum mechanical uncertainty relations: a few such relations are summarized in Table 1.1 [23]. Assuming that the SET is a linear amplifier the uncertainty relations pertaining to this situation is $S_v(\omega)S_I(\omega) \geq \frac{\hbar}{2}$ where $S_I(\omega)$ and $S_V(\omega)$ are the spectral

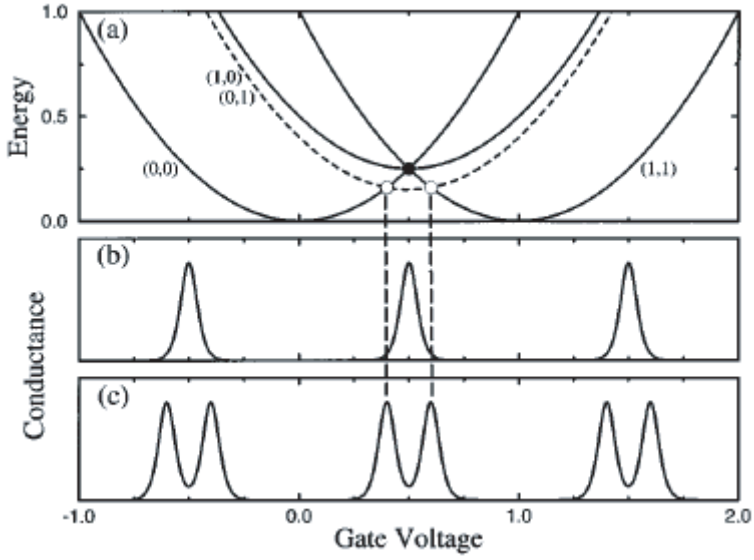


Figure 1.24 (a) A plot of the free energy of the coupled dot system versus the common gate voltage. (b) The conductance through the double dot system when the inter-dot coupling is negligible. (c) The conductance through the dot when the inter-dot coupling is substantial [40] .

densities of current and voltage noises of the amplifier respectively as illustrated in Fig. 1.25.

A few parameters which appear in this discussion quite often are as follows:

- $\tau_m$: The time needed to distinguish two qubit charge states.
- $\Gamma_{\rm mix}$: When performing measurements on a qubit the measurement not only

Table 1.1 Constraints imposed by the quantum mechanical uncertainty relations.

| System | Parameter | Back-action | Uncertainty relation |
|---|---|---|---|
| Heisenberg microscope | $\Delta x$ | $\Delta p$ | $\Delta x \Delta p \geq \hbar/2$ |
| Electronic amplifier | $S_V$ | $S_I$ | $(S_V S_I)^{1/2} \geq \hbar\omega/2$ |
| Qubit read-out | $T_m$ | $\Gamma_\phi$ | $T_m \Gamma_\phi \geq 1/2$ |

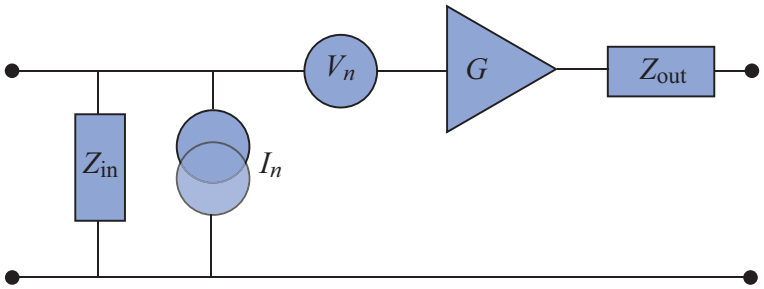


Figure 1.25 Equivalent circuit of a linear voltage amplifier. $Z_{\text{in}}$ is the input impedance and $Z_{\text{out}}$is the out put impedance. $V_n$ and $I_n$ are the voltage and current noise sources associated with the amplifier; adapted from [23].

dephases the qubit but may also cause transitions between two qubit states resulting in loss of information. This process is called mixing..

- $1/\tau_\phi$: The dephasing rate of the charge qubits.

The SET dynamics are noisy due to the stochastic nature of transport through it. The measurement time $\tau_m$ is determined by fluctuations in the SET current, in other words, $\tau_m$ is the time needed to distinguish two different dc currents corresponding to two different charge states at the SET input. In addition, fluctuations in the island charge induce a fluctuating voltage on the system which is coupled to the DQD through a capacitance $C_c$. In the next section we discuss a method to characterize the back action noise of SET experimentally.

## 1.6 Double quantum dot broad-band spectrum analyzer

DQDs can form an artificial two level system. Each dot in a DQD system can be tuned in such a way that only one level contributes to the transport [41].

Fig. 1.26 shows a schematic of a DQD energy diagram. Here $\mu_L, \mu_R, E_L$, and $E_R$ are the Fermi levels on the source and drain, and the energy levels on the left and right dots respectively. $\epsilon$ is the difference between the energy levels $E_L$ and $E_R$. The separation and the coupling between the levels can be tuned independently by varying the appropriate gate voltages, so that a DQD is a fully tunable two level system [42].

For operation as a spectrum analyzer the dots are tuned in such a way that the energy levels in the dots fall between the Fermi energies of the leads. The total current $I_{\text{tot}}$ through this system can be written as a sum of two terms, the elastic and the inelastic currents, $I_{\text{el}}$ and $I_{\text{inel}}$ respectively:

$$I_{\text{tot}}(\varepsilon) = I_{\text{el}} + I_{\text{inel}} \tag{1.87}$$

The elastic current at T=0 results from elastic tunneling and has the well known Lorentzian line shape

$$I_{\text{el}}(\varepsilon) = \frac{eT_c^2\Gamma_R}{T_c^2(2+\frac{\Gamma_R}{\Gamma_L}) + \frac{\Gamma_R^2}{4} + (\frac{\varepsilon}{\hbar})^2} \tag{1.88}$$

The inelastic current involves either emission or absorption of energy quanta to or from the environment. These process are depicted in Fig. 1.26. The inelastic current depends on the transition rates $\Gamma_L$, $\Gamma_i$ and $\Gamma_R$ where $\Gamma_L$, $\Gamma_i$ and $\Gamma_R$ are the tunneling rates from the left lead to QD1, QD1 to QD2 and QD2 to the right lead respectively:

$$I_{\text{inel}}(\varepsilon) = \frac{e}{\hbar}[\Gamma_L^{-1} + \Gamma_i^{-1} + \Gamma_R^{-1}]^{-1}. \tag{1.89}$$

When the central tunnel barrier dominates the transport, i.e. $\Gamma_i \ll \Gamma_R, \Gamma_L$, the inelastic current is given by

$$I_{\text{inel}}(\varepsilon) \simeq \frac{e}{\hbar}\Gamma_i(\varepsilon) = \frac{e}{\hbar}T_c^2 P(\varepsilon) \tag{1.90}$$

where $P(\epsilon)$ is the probability of exchanging energy $\varepsilon$ with the environment and is given by

$$P(\varepsilon) = \frac{1}{2\pi\hbar}\int_{-\infty}^{\infty} Exp[J(t) + i\frac{\varepsilon}{\hbar}]dt \tag{1.91}$$

Here J(t) is the autocorrelation function of the phase operators and is a measure of the spectral density of voltage fluctuations.

$$J(t) = \frac{2\pi}{\hbar R_K}\int_{-\infty}^{\infty} \frac{S_v(\omega)}{\omega^2}(e^{-i\omega t} - 1)d\omega. \tag{1.92}$$

Here we are interested in the current fluctuations of the environment. Consider a situation where a current noise source with a spectral density of current fluctuations $S_I(\omega)$ in the environment is coupled to the DQD through a transimpedance $Z(\omega)$. Then the spectral density of voltage fluctuations seen by the DQD is given by

$$S_v(\omega) =\mid Z(\omega) \mid^2 S_I(\omega) \tag{1.93}$$

so that

$$J(t) = \frac{2\pi}{\hbar R_K}\int_{-\infty}^{\infty} \frac{\mid Z(\omega) \mid^2}{\omega^2} S_I(\omega)(e^{-i\omega t} - 1)d\omega. \tag{1.94}$$

From these equations one can say that the inelastic current through a suitably

tuned DQD carries information about the spectral density of current fluctuations in a device coupled to it. In our system we have a RF-SET electrostatically coupled to a DQD. One can characterize the current noise of the RF-SET island by measuring the inelastic current through the DQD [42].

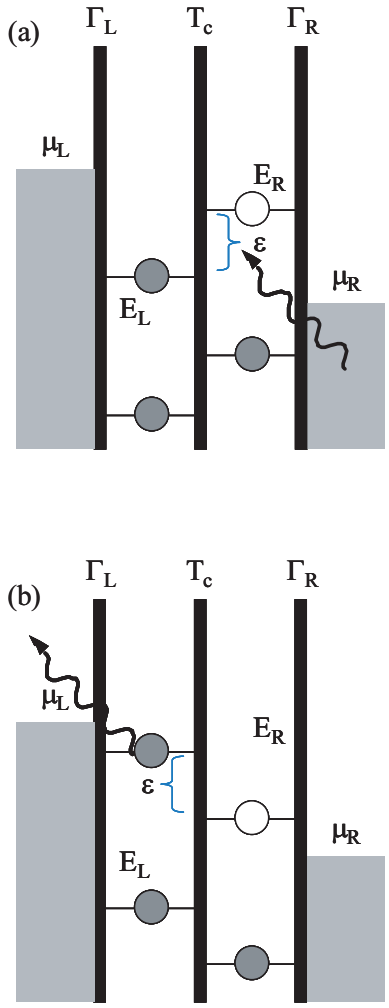


Figure 1.26 Inelastic transitions of a two level DQD system showing (a)$\varepsilon < 0$, absorption (b) $\varepsilon > 0$ emission

# Chapter 2

## Experimental Techniques

In this chapter various experimental techniques used during the sample fabrication and characterization are discussed; first the sample fabrication, second the low temperature techniques, third the sample wiring, and fourth the electrical characterization.

### 2.1 Sample fabrication

Experiments are performed on three different types of devices: RF-SETs, a QPC, and DQD/RF-SET systems. The RF-SET is a system of two Al/$AlO_x$/Al tunnel junctions whereas the quantum dots and QPCs are realized in a GaAs/AlGaAs heterostructure by the split gate technique. In general the sample fabrication process involves electron beam (e-beam) lithography, metallization by thermal evaporation, wet chemical etching and making ohmic contacts to the 2DEG by thermal annealing. First we discuss the individual fabrication processes and then explain the order in which they are combined to yield the final device.

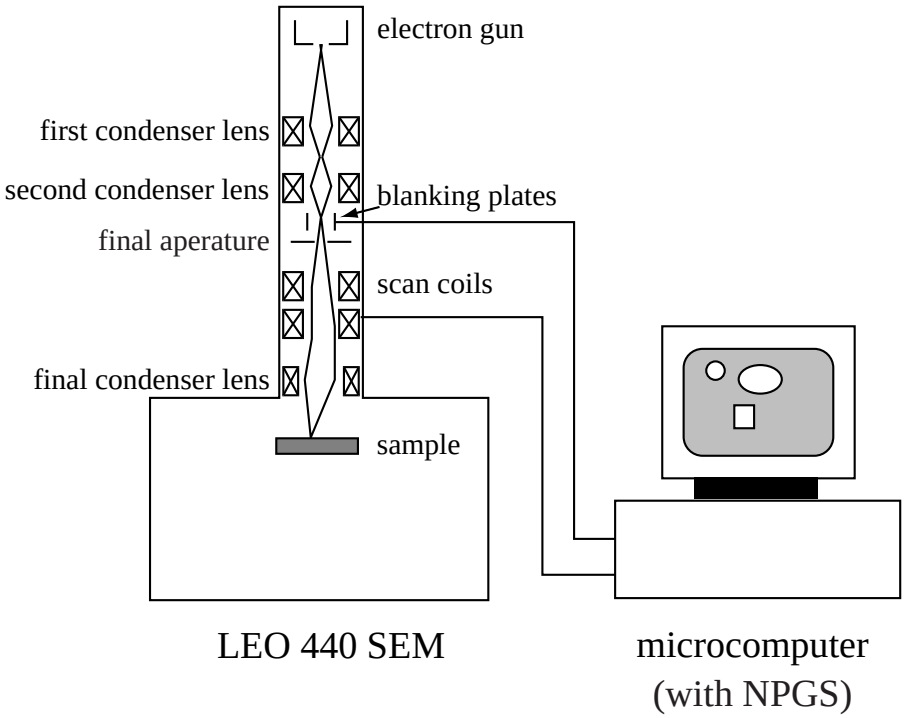


Figure 2.1 A schematic of the experimental setup of the electron beam lithography.

### 2.1.1 Pattern generation by e-beam lithography

Electron beam lithography depends on selective exposure of an electron beam resist which is sensitive to energetic electrons or ionizing radiation. In a positive resist the exposure weakens the resist by breaking the bonds binding the monomers. The resist in the exposed region can be dissolved by certain solvents, in a process called development. In this way the resist forms a stencil of the required pattern on the sample surface. A typical sequence of steps involved in this process is given below.

1. Cleave a small (4.5mm×3mm) chip from a GaAs/AlGaAs heterostructure

wafer.

2. Clean sample in acetone using ultrasound for 20 minutes. Rinse the sample in isopropanol afterwards, as acetone evaporates rapidly and may leave residue on the surface. Blow dry the sample with an air gun.

3. Mount the sample onto a resist spin coater. Apply a drop of 495K PMMA on the sample. Immediately start the spinner; spin @ 6000 rpm for 40s for the fabrication of Au electrodes defining quantum dots. For $Al/AlO_x/Al$ tunnel junctions spin PMMA-MAA @ 3000 rpm for 30s.

4. Bake on hot plate @ $180^0$C for 15 minutes. or @ $150^0$C for $Al/AlO_x/Al$.

5. Expose the chips to ultraviolet radiation for 3 minutes 30s for $Al/AlO_x/Al$.

6. Spin on a drop of 950K PMMA as explained in step 3 above.

7. Bake on hot plate @ $180^0$C for 15 minutes. or @ $150^0$C for $Al/AlO_x/Al$.

Once the above listed processes are carried out, the chips are ready to be patterned by electron beam lithography.

The pattern generation system consists of a scanning electron microscope (SEM) for which one can externally control the X and Y scan coils to write the desired pattern. First, the patterns are created using a CAD program and then 'run-files' are created with pattern generation software. This run-file controls the SEM to write the desired pattern on the chip. A schematic of this setup is illustrated in Fig. 2.1. Once the pattern is drawn, the sample is removed from the SEM sample chamber and developed. We use a 3:1 by volume mixture of isopropanol and methyl-isobutyl-ketone as the developer. The sample is developed

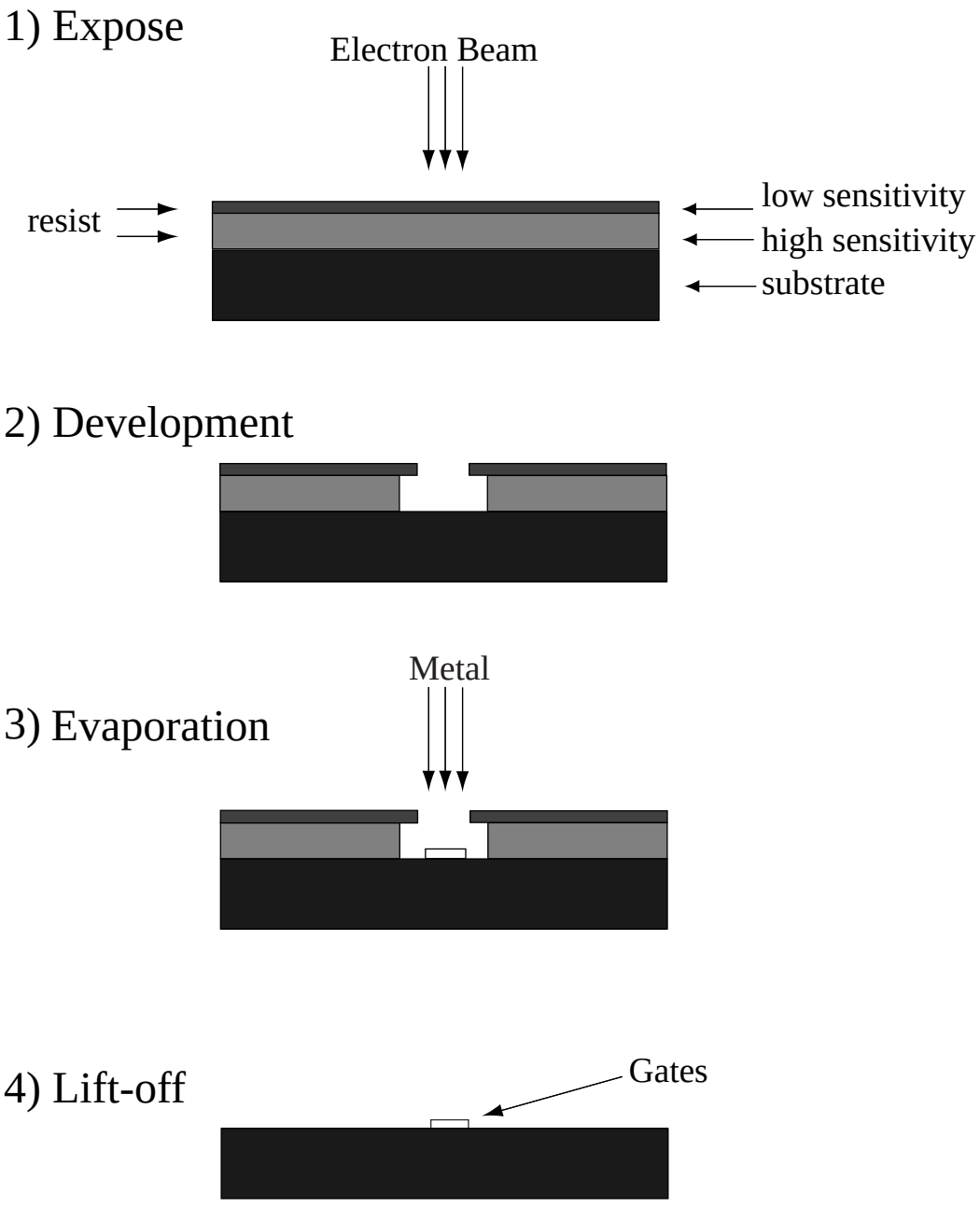


Figure 2.2 Schematic illustration of the fabrication of gold gates by electron-beam lithography.

in this solution for about 1 minute at $23^0$C followed by a 40s rinse in isopropyl alcohol. All of the gates defining the dots are made by Au evaporation as illustrated in Fig. 2.2 and the SET by Al shadow evaporation.

### 2.1.2 Shadow evaporation

The fabrication Al/$AlO_x$/Al involves the same electron beam lithography process described in the previous paragraph. The difference is in the two-level resist scheme and in the thermal evaporation of aluminum. In this scheme, a much larger undercut is formed in the bottom resist layer and a suspended resist bridge can be formed as shown in Fig. 2.3. A tunnel junction can be formed by first evaporating Al from one angle, introducing a small amount of $O_2$ to form a thin film of $AlO_x$ on the Al surface and then evaporating a second layer of Al from a different angle so that a thin $AlO_x$ layer is sandwiched between two Al layers as shown in Fig. 2.3.

### 2.1.3 Etching

The 2DEG beneath the SET behaves as a ground plane. The typical size of the SET contact pads is about $250\mu\text{m} \times 250\mu\text{m}$, so that the pad capacitance to the 2DEG is about 80pF. In contrast, the capacitance required for the optimum working conditions of RF-SET is about 0.3pF. To circumvent this problem we must deplete the 2DEG beneath the SET pads, typically by etching deep enough(about 50nm) that the donor electrons are trapped in surface states. The etchant is made by mixing a 1:1 by weight solution of citric acid in water and $H_2O_2$ in the ratio 30:1 by volume. This is a very weak etchant with an etch rate of approximately a

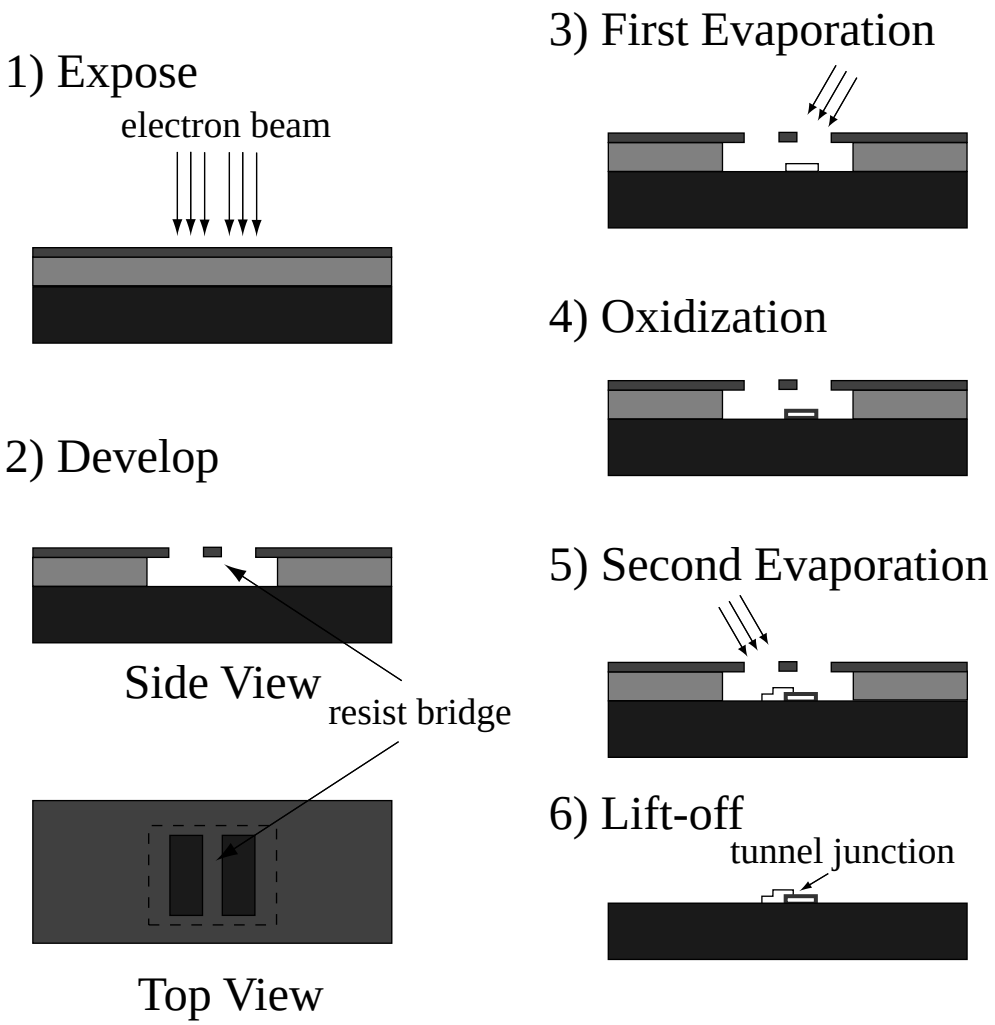


Figure 2.3 Schematic illustration of the fabrication of SET using electron beam lithography followed by shadow evaporation of aluminum.

few nm/sec. The region to be etched is first defined by e-beam lithography. After development, the sample is etched for about a minute followed by rinse in de-ionized water which gives about 50-60 nm etch depth. The etch depth is verified with the help of an atomic force microscope.

### 2.1.4 Ohmic contacts

We use an alloyed indium process to make ohmic contacts to the 2DEG. The main steps involved are listed below.

1. Clean sample as described in section 2.1.1.
2. Press In onto surface of sample using a moderately hot soldering iron so that the indium melts and sticks to the surface of the sample.
3. Place sample into tape heater oven. Flush oven with forming gas (20% $H_2$, 80% He) for 15 minutes. to purge air and moisture from the chamber.
4. Using a flow meter, set flow of forming gas to desired rate for baking, typically 70 ml/minutes.
5. Bake sample at $110^0$C for 1 minutes. to remove adsorbed water.
6. Ramp temperature to $400^0$C and hold at $400^0$C for 4 minutes.
7. Turn off heater. Leave forming gas flowing until sample reaches the ambient temperature.

Generally, at least four ohmic contacts are made on each sample to allow four probe $I$-$V$ measurements.

Having reviewed the individual steps, we can now explain the fabrication process of our device. Fig. 2.4 summarizes the essential steps involved in the fabrication of a DQD/RF-SET. The complete process requires four electron beam lithography steps. The first pattern is an alignment pattern as shown in Fig. 2.4(a). The subsequent three patterns should align to the alignment marks with an accuracy of 50-100 nm. The next step is etching. The 2DEG beneath all the large pads is etched away as described previously, and as shown in Fig. 2.4(b).

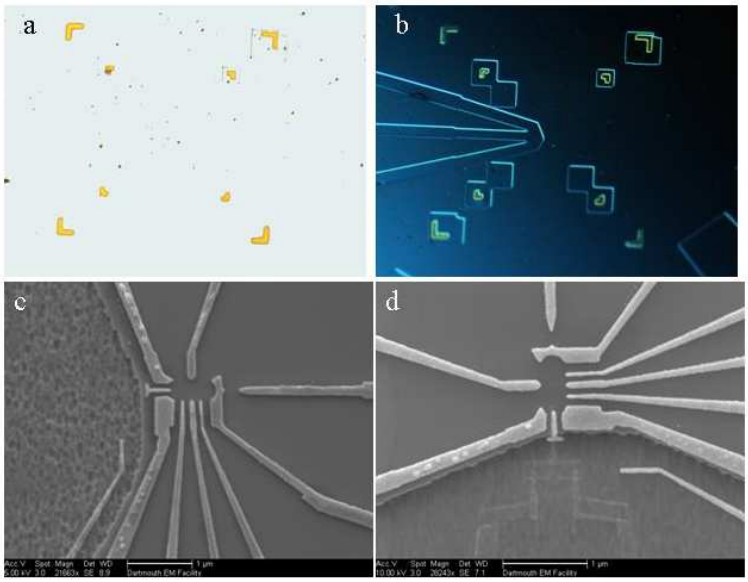


Figure 2.4 (a) Optical micrograph of the device after the fabrication of alignment marks. (b) Optical micrograph of the device after etching. (c) SEM micrograph of the sample after the fabrication of gold gates. (d) SEM micrograph of the final device after the fabrication of an SET.

Once the etching is performed, the next step is to make the ohmic contacts. After this, the gold gates and pads defining the quantum dots are made by electron beam lithography followed by thermal evaporation of gold. An SEM micrograph

of our sample after these steps is displayed in the Fig. 2.4(c). The final step in the sample fabrication process is the fabrication of the RF-SET. This is done by electron beam lithography followed by shadow evaporation of aluminum. Fig. 2.4(d) is the SEM micrograph of a completed sample.

## 2.2 Low temperature techniques

Observing various physical phenomena associated with mesoscopic physics requires that the experiments to be performed at low enough temperatures such that the energy scales associated with those dominates the thermal energy significantly. All the measurements discussed in this thesis are performed at temperatures $\approx 20$ mK range. Actual temperature of the electrons is higher than this and depends on the details such as filtering in the dc lines, the attenuators in the high frequency lines, and shielding of the sample. This section is devoted to a brief discussion on the achievement of low temperature, without which this report would be incomplete.

Fig. 2.5 is a bar chart representation of different refrigeration techniques used in various temperature ranges, of which the dilution refrigeration is the topic of discussion of this section. The most common way of cooling is by evaporation. The lowest temperature one can achieve by evaporative cooling is $\approx 250$ mK, by the evaporative cooling of $^3$He. The most common way of attaining temperature in the range of a few mK is by $^3$He and $^4$He dilution refrigeration[43, 44]. This technique forms the topic of discussion of this section since that is the technique used to achieve low temperature during all the experiments discussed in this report. The principles of dilution refrigeration can be best understood by going through some

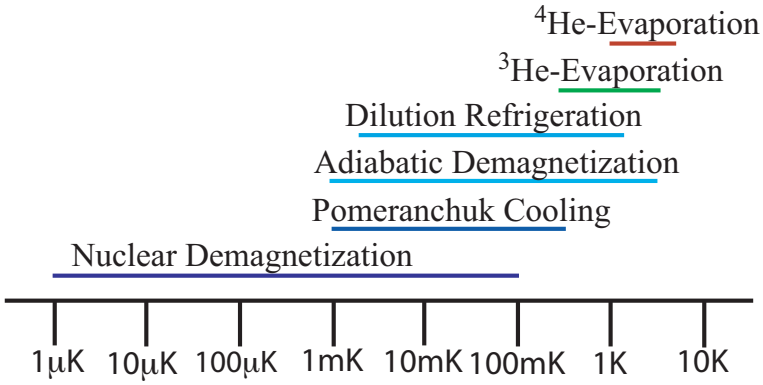


Figure 2.5 A bar chart listing of various techniques used to attain low temperature against various temperature ranges.

of the properties of $^3$He/$^4$He [44, 45], as illustrated in Fig 2.6.

The thermal properties of $^3$He and $^4$He are considerably different at low temperatures. Liquid $^4$He is a Bose liquid which undergoes a superfluid transition around 2.18K. Below 0.5K it is effectively in its quantum mechanical ground state. The liquid is thermally inert as very few phonons are excited, has very little entropy, and no viscosity. On the other hand, liquid $^3$He is a highly viscous Fermi liquid. Its heat capacity is approximately linear with the temperature T, which is rather high throughout the temperature range of interest for dilution refrigeration. From the phase diagram of $^3$He/$^4$He mixtures in Fig. 2.6 one can see that if a mixture of $^3$He and $^4$He is cooled below 0.7K with a $^3$He concentration exceeding 10%, the mixture will spontaneously phase separate in to a lighter $^3$He *rich phase* and a heavier $^4$He rich phase which is generally referred as the *dilute phase*. For a concentration of about 10% this phase separation happens about 0.4K. Below this temperature the rich phase floats over the dilute phase like

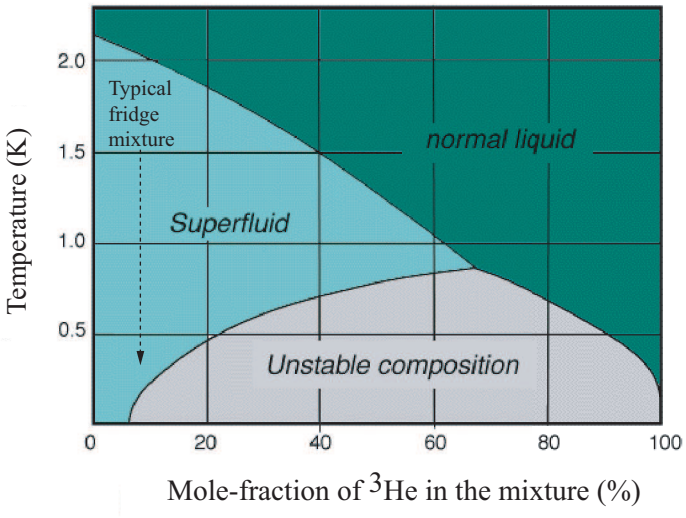


Figure 2.6 $^3$He/$^4$He phase diagram [46].

oil on water. As the temperature is lowered further the rich phase becomes almost 100% pure $^3$He. The dilute phase will contain about 6.6% of $^3$He. The details of this segregation depends on the quantum behavior of these two liquids. The rich phase corresponds to the liquid phase in an ordinary evaporation refrigerator where the $^3$He atoms are close together. Similarly the dilute phase corresponds to the vapor phase. When the $^3$He atoms are moved across the phase boundary downwards, cooling occurs as in the case of evaporative cooling. In conventional evaporative cooling the vapor pressure drops exponentially as T→0, which ultimately limits the cooling process. In contrast, the concentration of the $^3$He atoms in a dilution refrigerator remains constant at about 6.6% even below a few tens of mK. One can continuously pump $^3$He from the dilute phase without any change in the vapor pressure and continuously achieve cooling even down to a few mK.

This is the essential physics behind dilution refrigeration.

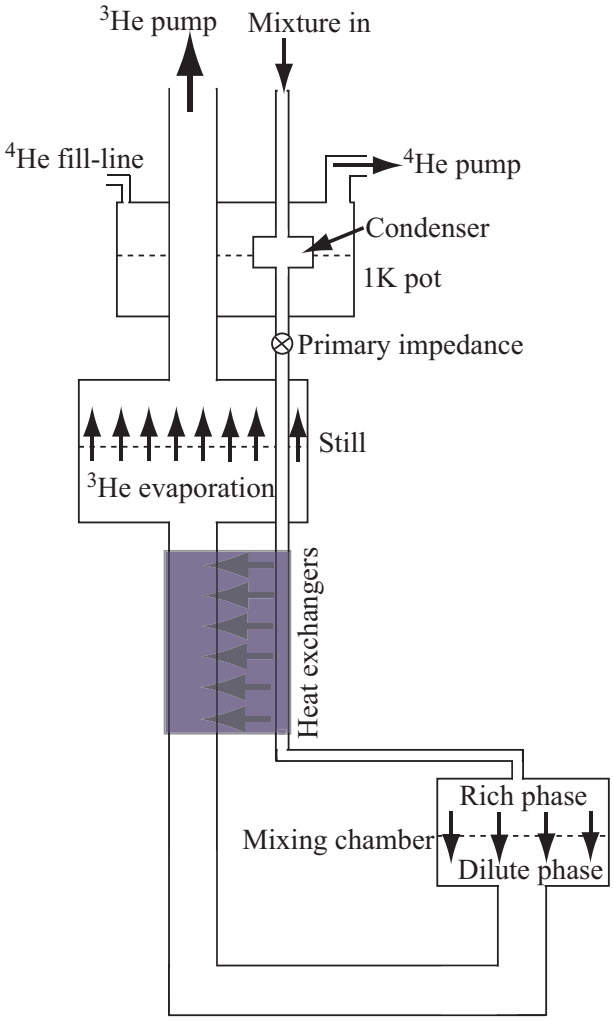


Figure 2.7 Schematic diagram of a dilution refrigerator.

Fig. 2.7 schematically represents the main parts of a dilution refrigerator. The function of the main parts can be understood as follows. First, a mixture of $^3$He/$^4$He with $^3$He concentration of about $15-20\%$ is pre-cooled to about 1.5K by passing the mixture through a small pot called 1K pot, which is cooled by normal

evaporative cooling of $^4$He liquid. A primary flow impedance right after the 1K pot ensures a higher pressure at the 1K pot so that the incoming mixture condenses on its way down to the mixing chamber. The mixture line and the heat exchangers are designed such that a high enough pressure is maintained throughout down to the mixing chamber so that the condensed mixture does not expand into the gaseous phase. This phase of the operation is called condensing. Once most of the available mixture is condensed then the mixture is made to circulate through the system. This is accomplished by the use of room temperature vacuum pumps. Right before circulation begins the mixing chamber is the warmest and the still is the coldest. Once the circulation is started the mixing chamber will start to cool down, which will also result in the phase separation of the mixture. Once phase separation occurs the dilute phase will extend up to the still. The vapor pressure will be entirely due to the $^3$He for reasons discussed earlier. The mixing chamber will proceed towards the base temperature as the still is being pumped.

## 2.3 Sample wiring

The RF-SET/DQD device is extremely sensitive to static electricity discharge. Fig. 2.8 depicts the effect of exposure to accidental static discharge while handling some devices.

Numerous precautions have to be taken to ensure a static discharge-free environment for the sample such as

1. Enclosing the sample in a metallic box (Faraday cage) whenever it is transfered from one place to other.

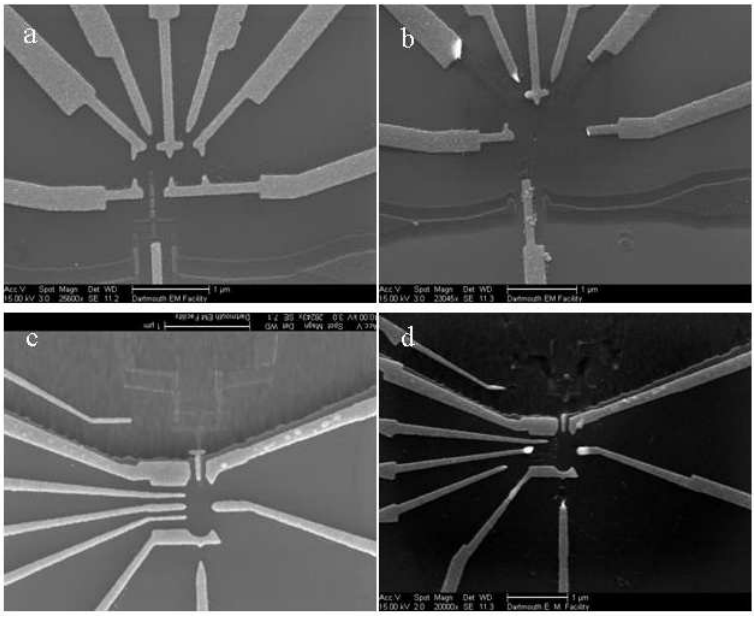


Figure 2.8 SEM micrographs depicting devices damaged by static electric discharge. (a) and (c) before and (b) and (d) after the discharge.

2. Using anti-static fans, mats, gloves, tweezers and grounding straps for hands while handling or wiring the sample.

3. Shorting the leads and pads of the devices to ground while wiring using a breakout box equipped with shorting (make before break) switches.

The pads connected to various electrodes on the device are wired onto a specially designed sample holder using either wire bonding or an indium sandwich technique. Fig. 2.9 (a) through (b) explains the indium sandwich technique step by step pictorially.

Once all the pads are wired the initial electrical checks for short circuits (for gate pads) and open circuits (for SETs and ohmic contacts) are done at room

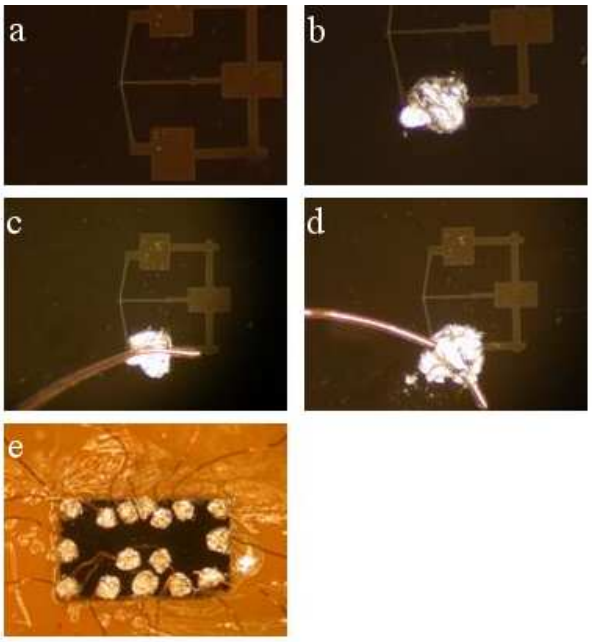


Figure 2.9 Sample wiring using Indium sandwich technique. (a) SET wiring pads. (b) Stick a small piece of fresh cut indium on to the pads using fine point anti-static tweezers. (c) Stick the wire on to the indium. (d) Press another small piece of indium on to the wire so that he wire is sandwiched between two Indium pieces. (e) A completed DQD/RF-SET device.

temperature. Then the sample holder containing the device is mounted onto the mixing chamber of a dilution refrigerator. Before buttoning up the inner vacuum can of the dilution fridge, the electrical checks are performed once again to make sure that the device has survived the transfer to the mixing chamber. Then the insert of the dilution fridge and cryostat are prepared to cool down towards 4K. The dc resistance of the SET and the pinch off voltage of the QPCs are checked again before operating the dilution fridge. On several occasions a positive voltage of about 300mV is applied to surface Schottky gates forming the

QPCs and dots while cooling down from room temperature to 4.2K for reasons discussed elsewhere.

## 2.4 Measurement techniques

This section deals with various dc, lock-in, and high frequency measurement techniques used to characterize the devices. Devices characterized using both high frequency and dc measurements are embedded in a tank circuit and require more careful, slightly different measurements, which also will be discussed.

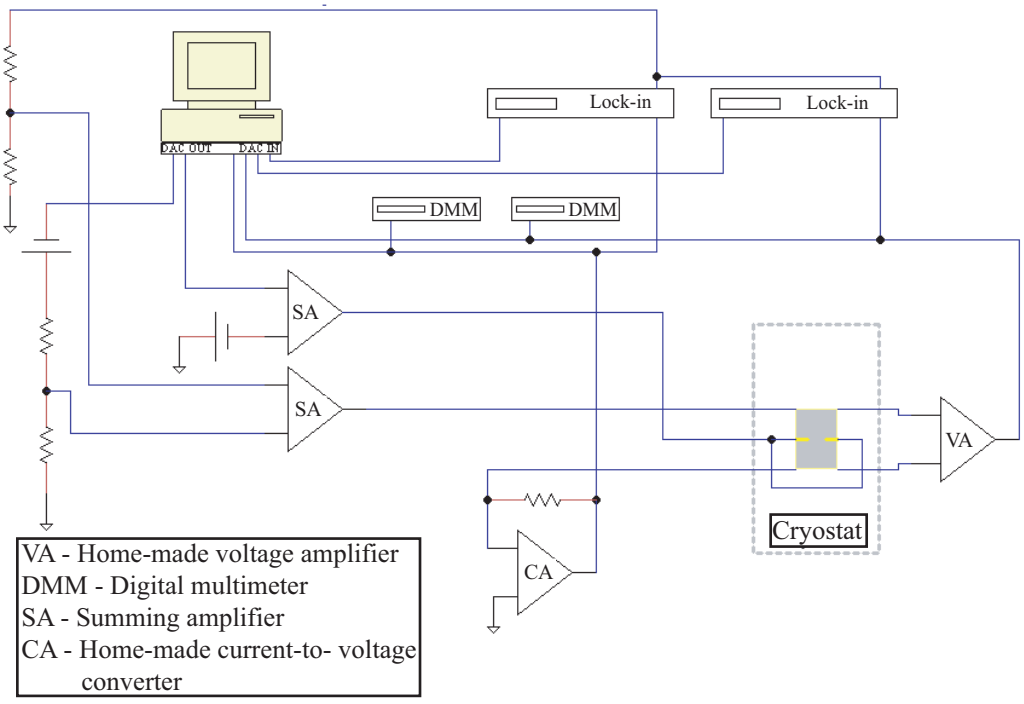


Figure 2.10 Schematic diagram of the $I$-$V$ measurement setup using four-probe method.

Fig. 2.10 is a schematic representation of basic four probe $I$-$V$ measurement set-up. The current through the sample and the voltage across it are measured using homemade low noise pre-amps. The ac and dc parts of the excitation with appropriate amplitude are added using a homemade summing amplifier before being fed to the ohmic contact of the sample. Return current is measured using a homemade current-to-voltage converter. The ac parts of the output of the voltage and current pre-amps are measured using lock-in amplifiers and the dc parts using digital multimeters. The bias/gate voltage sweeps were either generated by a homemade sweep box or by an NI 12-bit DAC PCI card. Output voltages of the pre-amps and lock-in amplifiers are always recorded using a computer controlled Labview-based data acquisition system. Extensive filtering is used at various stages to prevent noise from reaching the sample [32].

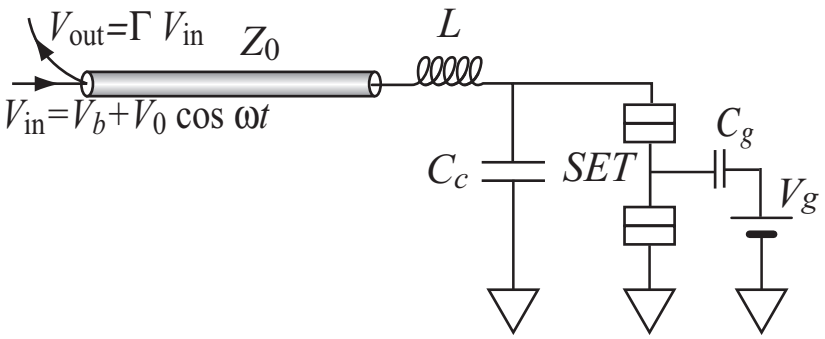


Figure 2.11 Schematic diagram of an SET embedded in a tank circuit.

Measurements on some of the devices, which are operated in both dc and high frequency regimes such as QPCs and SETs, are embedded in a tank circuit with a resonant frequency of about 1GHz. Fig. 2.11 is a schematic represents an SET

embedded in the tank circuit. One major difference in this situation compared to the previously discussed one is that the sample is grounded inside the cryostat. This makes it difficult to measure the returned current from the device as in the previous case. In principle, there are a few different ways to tackle this issue. One way is to measure the voltage across a known resistor in series with the sample from which one can determine the current through the circuit Fig. 2.12.

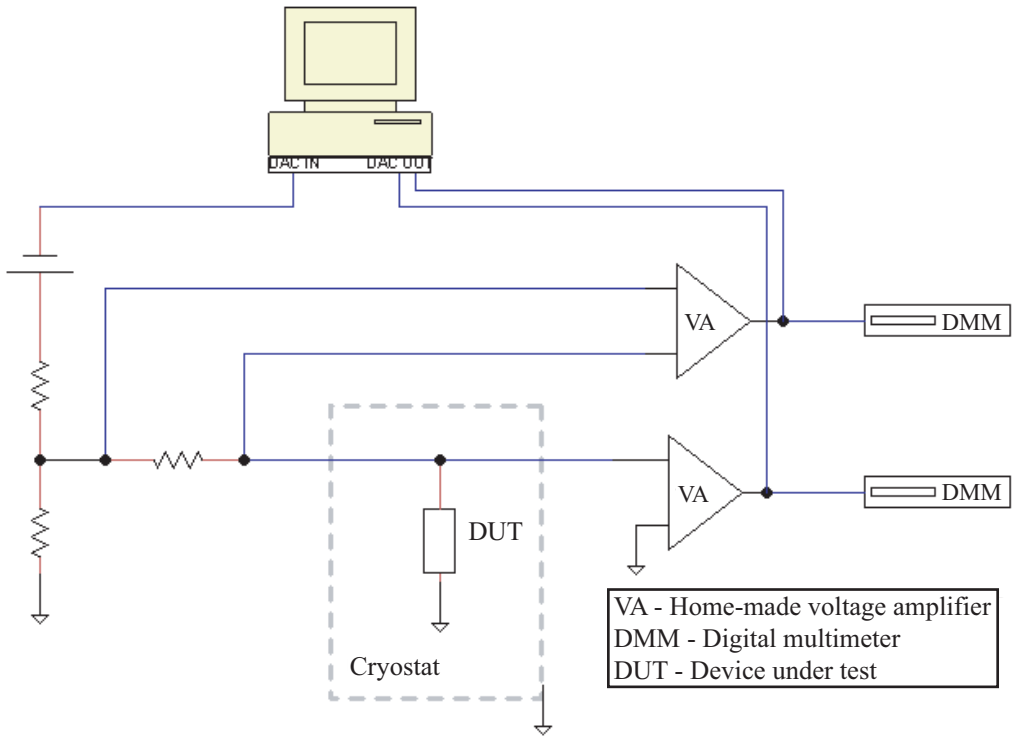


Figure 2.12 Schematic diagram of $I$-$V$ measurement setup for devices embedded in the tank circuit. The current measurement is accomplished by measuring the voltage across a standard resistor.

There are a few drawbacks to this technique. The sensitivity of the current measurement depends on the value of resistance in series with the sample. The

higher the resistance the higher the voltage drop produced across it for a given current. Inserting a high valued resistor compared to the resistance of the device will turn a voltage bias into a current bias. Also, using a large resistor will result in higher thermal noise in the system. Voltage noise in a system is proportional to the square root of the resistance, band width, and absolute temperature.

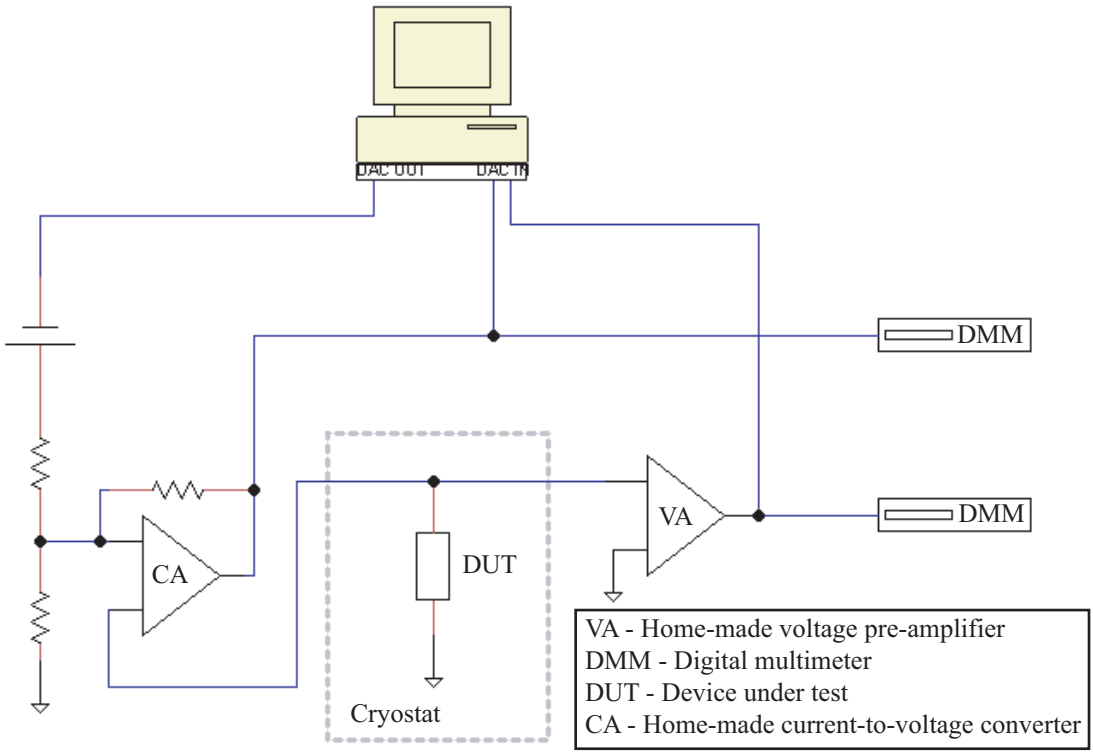


Figure 2.13 Schematic diagram of $I$-$V$ measurement setup for devices embedded in the tank circuit using a floating current amplifier.

Another way to take care of this issue is as shown in Fig. 2.13. A current-to-voltage converter is used in the floating mode in this case. This improves the

sensitivity and noise performance by quite a bit. One problem with this method is it tends to become unstable and also has trouble measuring current through high impedance devices such as an SET in the blockade regime; the current amplifier still registers some small current when the device is in the blockade regime. This could be due to some small leakage path to the ground when the amplifier is floated.

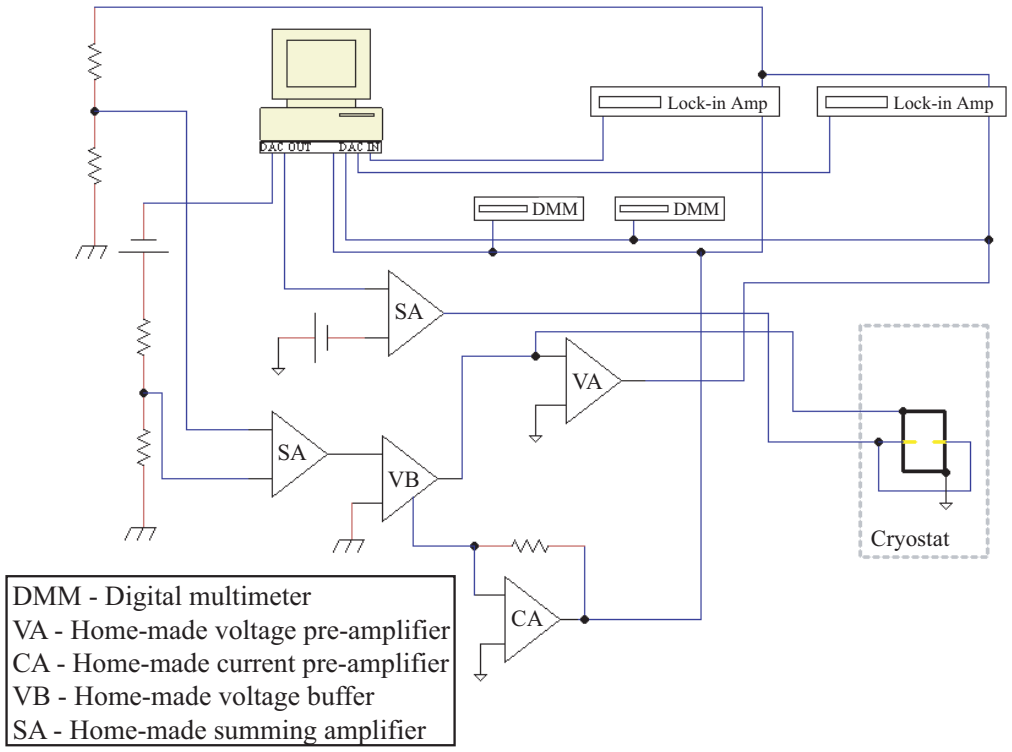


Figure 2.14 Schematic diagram of $I$-$V$ measurement setup for devices embedded in the tank circuit. In this setup the unity gain voltage buffer acts as a floating voltage source

The third way is as shown in Fig. 2.14. So far, this method is the most success-

ful in performing low noise dc or lock-in measurements on samples embedded in the tank circuit. Most of the data in this thesis was collected using this method. The heart of this measurement is the buffer right after the summing amplifier. The circuit common of the buffer is grounded through the current-to-voltage converter. This buffer acts as a floating variable voltage source. In this way one can use the current to voltage converter in the grounded mode for which it is most stable and least subject to leakage currents.

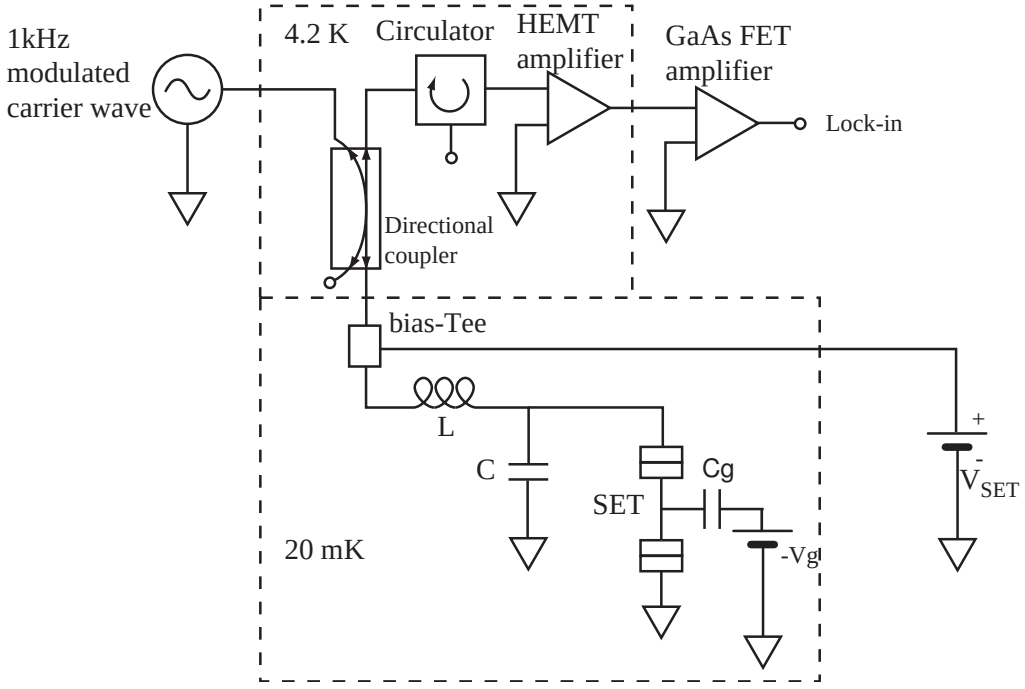


Figure 2.15 Schematic diagram of rf scan setup.

High frequency characterization of the device consists of performing rf-reflectometry on the sample which is embedded in a tank circuit, at or near the resonance. Fig. 2.15 is a schematic representation of the rf circuitry use to perform most of

the high frequency measurements. The first step is to determine the resonant frequency and the change in the reflectance as the device is taken into or out of the blockade. There are two ways to do this. One is to apply a 1kHz 100% amplitude modulated rf signal at the input port. The amplitude of reflected wave is recorded after demodulation using a diode. This measurement is performed as the frequency of the input signal is swept in the desired range. Two frequency sweeps are taken, one when the device is in the blockade and another when it is out of the blockade. An easier and faster way to perform the same measurement is to use a network analyzer. The resonant frequency and frequency of best response can be found out from two sets of frequency sweep data.

# Chapter 3

## Radio-Frequency Superconducting Single Electron Transistor

This chapter is devoted to a discussion of the measurements performed on radio-frequency superconducting single electron transistors (RF-SET). The sub-gap ($eV < 4\triangle$) JQP and DJQP features are subject to CB and charging effects. One can utilize this property of SSETs and operate the RF-SET in the sub-gap regime, which forms the subject of discussion of this chapter. Measurements are performed on a number devices with different junction resistances, but data from only a few relevant ones are presented in this chapter .

### 3.1 Optimizing the charge sensitivity of RF-SET

Our SSETs consists of two $Al/AlO_x/Al$ tunnel junctions in series and one or two metallic gates electrostatically coupled to it. Fabrication details are discussed in the previous chapter. All the measurements are performed in a $^3He/^4He$ dilution refrigerator with a base temperature of $\approx 20$ mK. The devices are characterized first in the dc mode, after which the high frequency studies are performed. The dc $I$-$V$ characteristics of one of the devices with a total junction resistance $R_n \approx 29k\Omega$ is shown in Fig. 3.1.

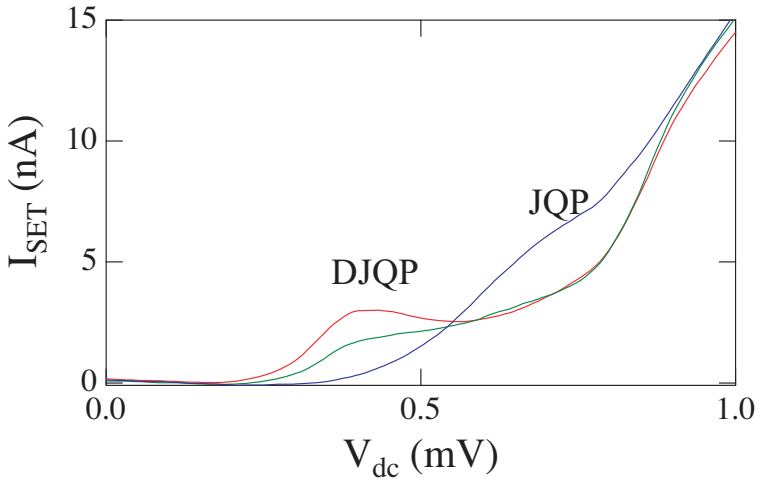


Figure 3.1 $I$-$V$ characteristics of SSET with $R_n = 29\text{k}\Omega$. Different curves correspond to different voltages on a nearby gate.

The charging energy can be determined from the position of DJQP feature in the $I$-$V$ curve from the relation $eV = 2E_c$. The superconducting gap for our devices is $\approx 200\mu$V. The main device parameters are, $E_c = 200\mu$V, Superconducting gap $\triangle = 200\mu$V and Josephson coupling $E_J = \frac{R_K}{R_n}(\frac{\triangle}{2}) = 78\mu$V

The next step is to find out the resonant frequency and the frequency of best response. Fig. 3.2 (a) is a plot of rf response of the sample versus frequency for small applied input power, $\approx$ 105 dBm, referred to the input port of the cryogenic amplifier, while SSET is in the CB (blue) and out of CB (red). The resonant frequency is about 1GHz, and the frequency of best response is around 980MHz. The impedance of the tank circuit deviates from 50$\Omega$ considerably as we move away from the resonance, so the frequency of best response might not be the frequency at which the difference between the two curves in Fig. 3.2 (a) is maximum. One has to explore around the resonance to find out the frequency of

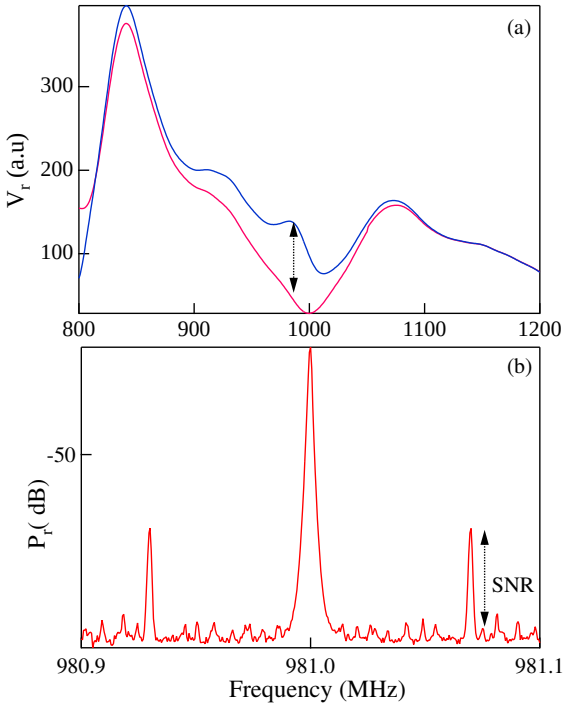


Figure 3.2 (a). Reflected rf voltage from the tank circuit while the SSET in CB (blue) and out of CB (red). The vertical dashed-line with arrows represents the frequency of best response. (b) Representative power spectrum of a reflected carrier wave amplitude modulated by a 70kHz voltage oscillation on a nearby gate.

best response.

The next step is to determine the charge sensitivity (CS) of RF-SET. Usually the SSET is biased around any of the sub gap current structures, and a small ac voltage is applied to one of the nearby gates. Amplitude of the ac gate excitation in $e$ induced on the SSET island is calibrated from the CBO taken by sweeping the same gate. Usually, a voltage oscillation of about 0.1 $e$ rms or lower at a frequency of about 100 kHz is applied on to gate. As a result, the conductance

(resistance) of the SSET also will oscillate at the same frequency as that of the gate signal. With this operating condition the rf reflected power spectrum is recorded. Since the reflectivity of the tank circuit is a linear function of the change in SSET resistance the reflected rf signal will be amplitude modulated by the gate signal, which will show up as side peaks in the reflected power spectrum as shown in Fig. 3.2 (b). The center peak is the input signal, and the side peaks are created by the oscillating gate voltage. The CS is given by

$$\delta q = \frac{\triangle q}{\sqrt{BW}10^{\mathrm{SNR}/20}} e/\sqrt{\mathrm{Hz}} \tag{3.1}$$

where $\triangle Q$ is the charge oscillation induced on the SSET island in $e$ and SNR is the signal-to-noise ratio of the side peak in Fig. 3.2(b). From Eq. 3.1 we can see that the CS is a function of the SNR. The input rf power, dc bias and the dc gate voltage are optimized to find the operating point of best SNR. Generally an amplitude modulated signal is given by [47],

$$\begin{aligned} V \;=\; & \underbrace{A\cos\omega_c t}_{\text{carrier signal}} + \\ & \overbrace{\frac{Am}{2}\cos(\omega_c+\omega_m)}^{\text{right side-peak}} + \\ & \underbrace{\frac{Am}{2}\cos(\omega_c-\omega_m)}_{\text{left side-peak}} \end{aligned} \tag{3.2}$$

where $A$ is the amplitude of the carrier wave, $0 < m < 1$ is the modulation index and $\omega_c$ and $\omega_m$ are the frequencies of the carrier wave and gate modulation. From

Eq. 3.2, the SNR and CS are proportional to the modulation index $m$ and the amplitude of the carrier wave $A$. The first question one would like to ask at this point is over what range in $A$ Eq. 3.2 holds, ie, how large a carrier wave amplitude one can apply?

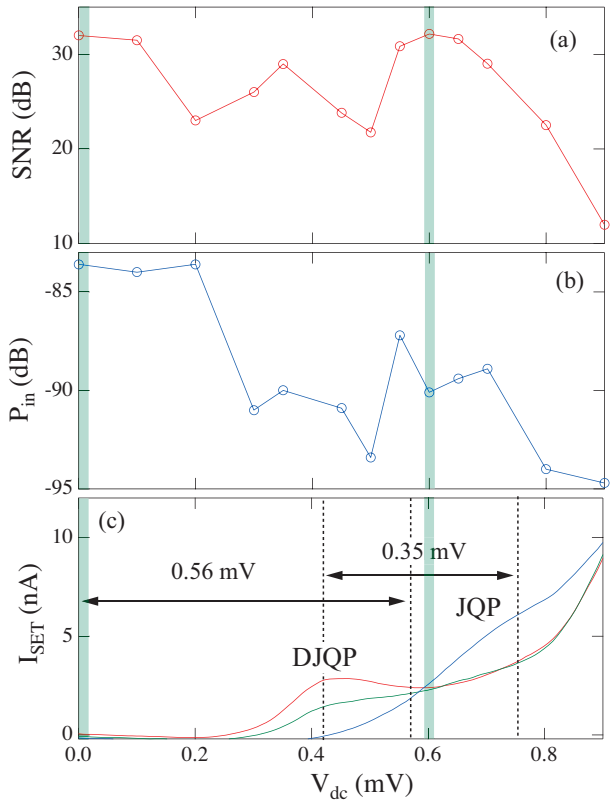


Figure 3.3 (a) SNR v/s $V_{\rm dc}$ with the input rf power optimized for best SNR at each operating point (b) Optimized rf input power v/s $V_{\rm dc}$ to get the best SNR in (a). (c) $I$-$V$ characteristic of the SSET showing the different sub-gap features. Shaded regions represent the operating points with best SNR.

Fig. 3.3 (a) is a plot of the SNR at different SSET dc bias conditions and Fig. 3.3 (b) is the corresponding input rf power, referred to the input stage of the cryogenic amplifier, optimized to give the best SNR. The shaded region cor-

responds to the points of best SNR. One can notice that the optimized input rf power is very different at these two points. This can be explained with the help of Fig. 3.3 (c), the $I$-$V$ curve of the SSET. The rf voltage which rides over the dc voltage has an averaging effect on the $I$-$V$ characteristic. It moves the SSET bias back and forth around the dc bias at a rate set by the the carrier frequency within a voltage range given by the peak-to-peak carrier-wave amplitude and the $Q$ of the tank circuit. The rf voltage makes the SSET spend more time towards the extreme points of the voltage oscillation than at the center of oscillation set by the dc bias. This is analogous to the fact that a simple pendulum spends more time at its extreme points than in the middle. A general rule of thumb to optimize the SNR is to cause the SSET to spend more time at the bias voltages where the charging effects are maximum. If the rf amplitude is increased further, then the rf voltage makes the SSET swing past the best response points and will start including contributions from regions where there are no charging effects. This results in a reduction in SNR. When the SSET is biased at the middle of the gap (shaded region on the right side of Fig. 3.3), to get the best sensitivity one has to turn up the rf amplitude to $\approx 560\mu V$ . At this operating condition the charging effects of the DJQP features contribute to the SNR. At the second point of best CS ( the shaded region in the middle of Fig. 3.3) a similar SNR was obtained for a much lower rf bias $\approx 350\mu V$. In this case the contribution is more or less equally from both the DJQP and JQP regions. A further increase in the rf bias reduced the SNR . This is probably due to the fact that the time spent by the SSET is more towards the left side of the DJQP and right side of JQP features where the charging effects are not as significant as they are between the two features.

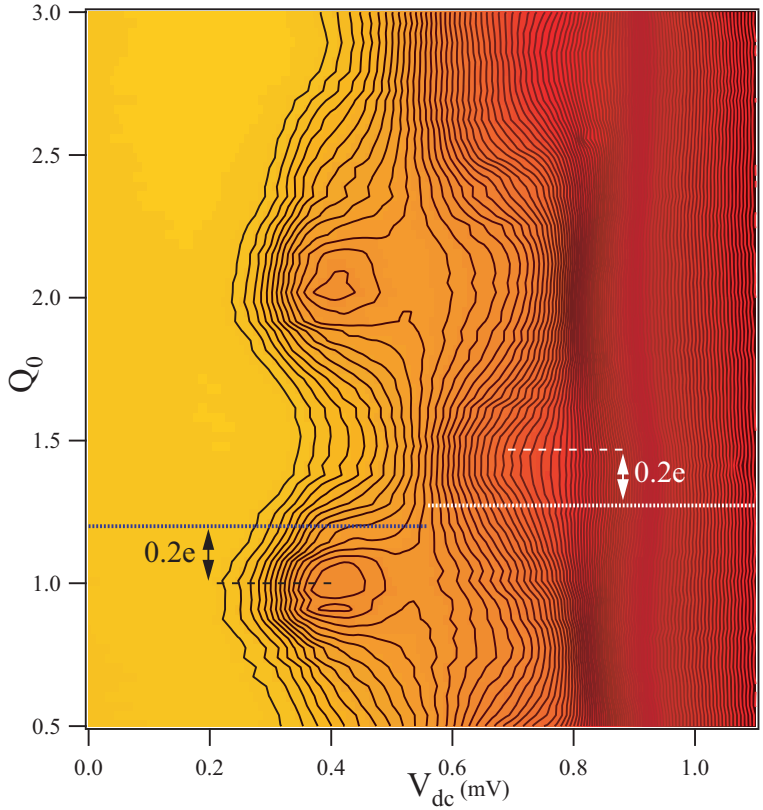


Figure 3.4 False-color plot of dc current through SSET in the $V_{\rm dc} - Q_0$ plane. Blue dash-line represents the gate voltage at which the SNR is maximum on the DJQP side and the white dashed-line on the JQP side of the $I$-$V$ characteristic.

Fig. 3.4 is a false-color plot of the SSET current in the $V_{\rm dc}$-$Q_0$ plane. The gate voltage $V_g = \frac{Q_0}{C_g}$ of best response is marked by a blue dashed line on the DJQP side of the $I$-$V$ curve and by a white dashed line on the JQP side. The position of this line on the $Q_0$ axis depends on how sharp the CBO are, but occurs where the slope of the CBO is a maximum. The point of best SNR switches from the DJQP side to the JQP side half way between the DJQP and JQP features. When the SSET is biased in between the DJQP and JQP feature the CS does not seen too

much affected whether the gate voltage sits on the blue line or the white line. In the next section the effect of quantum fluctuations on the performance of RF-SET is discussed.

## 3.2 Effect of quantum fluctuations on the performance of radio-frequency superconducting single electron transistor*

The radio-frequency single electron transistor (RF-SET) is a highly sensitive, fast electrometer, and has been suggested as a potentially quantum-limited linear amplifier suitable for measurements of individual electronic charges [23, 24, 48, 49]. Recent investigations have addressed use of the RF-SET as an electrometer [24, 25, 50], a readout device for charge based qubits [26, 51, 52], and a sensor for real-time electron counting experiments [27]. Linearity is a fundamental assumption of theoretical discussions of the quantum limits of amplifiers [23, 53]. Nonetheless, there has been no detailed investigation of the range of linear response for the RF-SET.

Most theoretical studies of RF-SET performance focus on normal metal SETs, either in the sequential tunneling [23, 54, 55] or cotunneling regimes [49], while most experiments are performed using a superconducting SET (SSET)[25–27, 50]. Transport in the SSET can be divided into two regimes, depending on the relative sizes of the bias voltage $V_{dc}$ and superconducting gap $\Delta$: above-gap ($eV_{dc} > 4\Delta$), dominated by Coulomb blockade of quasiparticles, and subgap ($eV_{dc} < 4\Delta$), dom-

*adapted from [32]

inated by DJQP and JQP cycles [33, 34]. While the best charge sensitivities are found for above-gap operation [25] , the SSET back-action—the rate at which it dephases a measured system—is largest there [23, 48, 52] . Recent work has focused on subgap operation for which back-action is significantly reduced, and shot noise is non-Poissonian [48, 51, 56]. Theoretical studies of quantum fluctuations in the SSET have been limited to above-gap cotunneling of quasiparticles[57]. We find that linearity and subgap quantum charge fluctuations in superconducting RF-SETs are intimately related: as quantum fluctuations strengthen, linearity and signal-to-noise ratio (SNR) improve, while charge sensitivity remains excellent.

Our SSETs consist of a small island connected to macroscopic leads via two Al/$AlO_x$/Al tunnel junctions J1(2) with normal state resistances $R_{1(2)}$ as illustrated in Fig. 3.5(a). We have fabricated and characterized three samples, S1, S2, and S3 with total resistance $R_n = R_1 + R_2$ of 58, 38 and 24k$\Omega$; an electron micrograph of S2 is shown in Fig. 3.5(b). Results similar to those described here were previously observed in four other samples. The samples were mounted on the mixing chamber of a dilution refrigerator at its base temperature of 20mK. High-frequency noise was excluded by $\pi$-type filters at room temperature, and both copper powder and lossy transmission line filters in the cryostat. Total attenuation for frequencies above 1GHz was $\geq$ 70 dB, of which $\geq$ 20dB was at the mixing chamber temperature. A Nb chip inductor $L \approx$120nH together with the parasitic capacitance $C_p \approx$0.2pF of the SET contacts constituted a tank circuit with resonant frequency $f_{LC} \approx$1GHz and quality factor $Q \approx 16$. We measured the samples' current-voltage ($I$-$V$) characteristics in an asymmetric voltage-biased

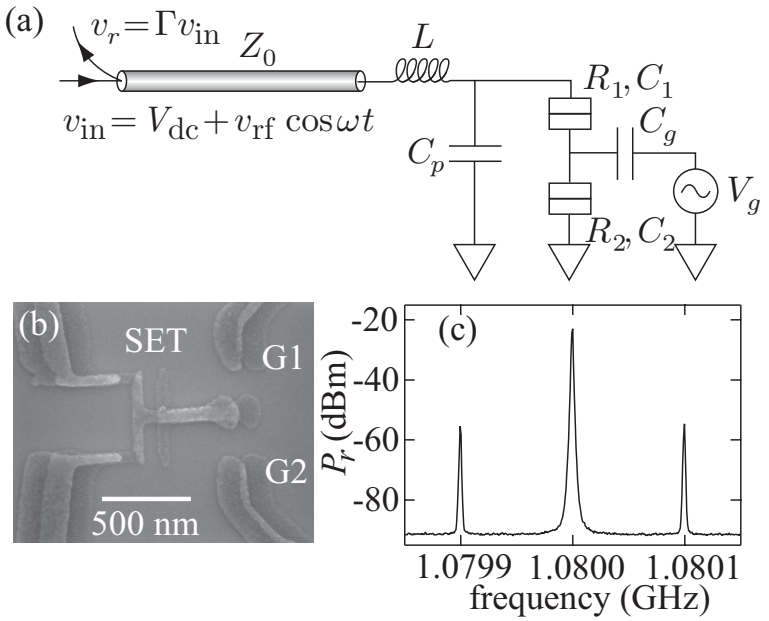


Figure 3.5 (a) Schematic diagram of RF-SET operation. A voltage $v_{\rm in}$ consisting of dc and rf biases $V_{\rm dc}$ and $v_{\rm rf}$ is incident on a tank circuit comprising an inductor $L$, a capacitor $C_p$, and the SET, with junction resistances and capacitances $R_{1(2)}$ and $C_{1(2)}$. A charge oscillation $q_0 cos\omega_m t$ modulates the reflection coefficient $\Gamma$ of the tank circuit and the reflected voltage $v_r$. (b) Post-measurement electron micrograph of S2. Gates G1 and G2 were used vary the SET offset charge. (c) Power spectrum of $v_r$ for $q_0 = 0.063$e rms and $\omega_m/2\pi = 100$ kHz. The charge sensitivity and SNR of the RF-SET were determined from the sideband power and noise floor; the latter, dominated by the white noise of a cryogenic amplifier, was independent of sample, bias, and offset charge.

Table 3.1 Sample parameters. Resistances are in kΩ, energies in $\mu$eV, and areas in $10^{-3}\mu\text{m}^2$.

| Device | $R_n$ | $\Delta$ | $E_c$ | $E_J$ | $\alpha$ | $A_{tot}$ | $E_c^o$ | $E_c^s$ |
|---|---|---|---|---|---|---|---|---|
| S1 | 58 | 200 | 230 | 22 | 0.78 | 4.1 | 254 | — |
| S2 | 38 | 200 | 250 | 34 | 1.08 | 3.4 | 291 | 258 |
| S3 | 24 | 190 | 162 | 54 | 2.65 | 5.0 | 218 | 162 |

configuration [Fig. 3.5(a)] by varying the dc bias voltage $V_{dc}$ in the absence of an rf excitation. Details of rf operation are discussed elsewhere [24, 25]. The SET offset charge $Q_0 + q_0\ cos\omega_m t$ consisted of a dc component $Q_0$ that set the overall working point and an ac component of amplitude $q_0$ that modulated the reflected voltage $v_r$. Power spectra of $v_r$ as shown in Fig. 3.5(c) were used to determine the charge sensitivity $\delta q$ and SNR.

In Fig. 3.6, we show $I$-$V$ characteristics of the samples for different $Q_0$, with $q_0 = 0$. For S1, we observe clear above-gap ($V_{dc} \geq 800\mu$V current modulation corresponding to Coulomb blockade of QP tunneling [Fig. 3.6(a)]. The sub-gap features corresponding to the JQP cycles are sharp and clearly distinguished. As illustrated in Fig. 3.7, the simplest JQP cycle consists of resonant tunneling of a Cooper pair through one junction and two QPs through the other, transporting two electrons through the SET. The cycle can occur only when the transition $0 \rightarrow 1$ ($1 \rightarrow 0$) is allowed, ie., for $eV_{dc} > E_c + 2\Delta$ where $E_c = e^2/2C_\Sigma$ is the charging energy of the SET and $C_\Sigma = C_1 + C_2 + 2C_g$ its total capacitance. While the JQP cycle is forbidden at lower bias, at $Q_0/e = n_g \approx \frac{1}{2}$ and $eV_{dc} = 2E_c$ Cooper pair tunneling is resonant at both junctions and the double JQP (DJQP) cycle becomes possible. The fact that sequential tunneling cannot occur via either

cycle for $2E_c \leq eV_{dc} \leq E_c + 2\Delta$ is reflected in S1 by a sharp drop in current at $V_{\rm dc} \approx 630\mu$V just below the JQP feature.

As $R_n$ decreases, so does current modulation for $eV_{\rm dc} > 4\Delta$, consistent with suppression of the Coulomb blockade by QP cotunneling [57] : the modulation is reduced for S2, and nearly absent for S3 [Fig. 3.6(b) and (c)]. In contrast, features corresponding to the JQP cycles still exist but become progressively less sharp. Since these cycles involve both Cooper pair and QP tunneling, we hypothesize that subgap quantum fluctuations of quasiparticles are strong, while quantum fluctuations of Cooper pairs remain weak. Since, to the best of our knowledge, no theoretical description of subgap quantum charge fluctuations in the SSET exists, we provide simple arguments supporting our hypothesis.

We first compare with known results for above-gap transport. We define [57] a parameter $\alpha \equiv \frac{\Delta}{E_c}\frac{\pi\hbar}{e^2}(R_1^{-1} + R_2^{-1}) = \frac{8E_J}{E_c}$ characterizing the strength of quantum fluctuations for QPs, assuming $R_{1(2)} = R_n/2$ and using the Ambegaokar-Baratoff relation for the Josephson coupling energy $E_J = \frac{\Delta}{4}\frac{R_k}{R_n}$ where $R_k = \frac{h}{e^2}$. Quantum fluctuations are negligible for $\alpha \ll 1$. Determining $E_c$ from the location of the DJQP peak and $E_J$ from the total junction resistance we calculate $\alpha$ as in Table 3.1. None of our samples satisfies $\alpha \ll 1$, although for S1 ($\alpha = 0.78$) some above-gap Coulomb modulation survives. The progressively weakening modulation for S2 ($\alpha = 1.08$) and S3 ($\alpha = 2.65$), is consistent with previous results[57].

Cotunneling as described in [57] occurs only for $V_{dc} > 4\Delta/e$: it results in two QP excitations and transfers a single electron through the SET. Other virtual processes, however, remain important for $V_{dc} < 4\Delta/e$. For normal SETs, $E_c$ is renormalized by quantum charge fluctuations: for example, near $n_g = 0$, the

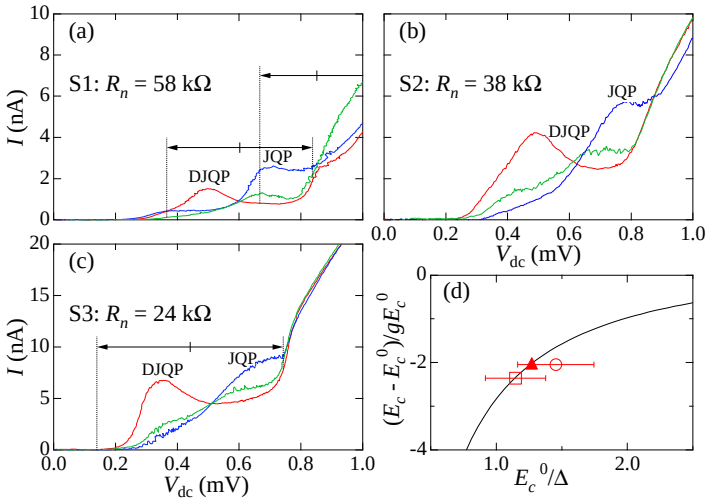


Figure 3.6 $I - V$ characteristics for (a) S1 (b) S2 and (c) S3 (note scale change), were chosen for $Q_0$ showing the DJQP process (red or gray), the JQP process (blue or dark gray), and an intermediate value of $Q_0$ (green or light gray). The arrows and vertical hash mark show the peak-to-peak rf amplitude $2Qv_{\rm rf}$ and dc bias $V_{\rm dc}$ for optimal RF-SET operation. (d) Variation in the measured charging energy $E_c$ relative to the bare charging energy $E_c^o$ for S1 (solid triangle), S2 (circle) and S3 (square). Error bars indicate uncertainty in $E_c^o$. Solid line: theoretical prediction.

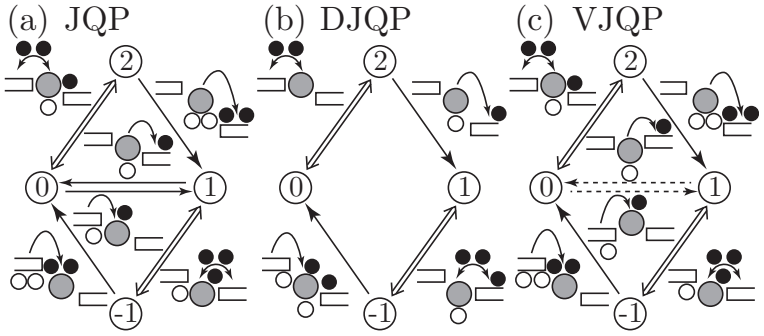


Figure 3.7 Various JQP cycles. Here J2(1) is on the left (right) and $V_{dc} > 0$. Solid (empty) circles indicate quasielectrons (quasiholes) created during a cycle. The grey circles (white rectangles) indicate the SET island (leads) and their vertical separation the free energy difference for the transition. Cooper pair, quasiparticle, and virtual tunneling are indicated by double, single, and dashed arrows. (a) JQP cycle. Beginning in the state $n = 0$ ($n = 1$), where n is the number of excess electrons on the SET, the transition $0 \rightarrow 1$ ($1 \rightarrow 0$) is allowed, bringing Josephson tunneling through J1(2) into resonance. Cooper pair tunneling $1 \Leftrightarrow -1$ ($0 \Leftrightarrow 2$) is interrupted by QP tunneling through the opposite junction $-1 \rightarrow 0$ ($2 \rightarrow 1$), completing the cycle. (b) DJQP cycle. When Josephson tunneling is resonant for both J1 and J2, transport occurs via the sequence $0 \Leftrightarrow 2$, $2 \rightarrow 1$, $1 \Leftrightarrow -1$, $-1 \rightarrow 0$. (c) Proposed VJQP cycle. If the transition $0 \rightarrow 1$ ($1 \rightarrow 0$) is forbidden, it may still occur virtually. The remaining JQP transitions are allowed for relevant $V_{\rm dc}$.

effective charging energy $E_c \approx E_c^0(1-4g)$ where $g = R_K/\pi^2 R_n$ is the dimensionless parallel conductance of the tunnel junctions and $E_c^0$ the bare charging energy; similar renormalization occurs in SSETs [50, 58]. Calculating the first-order energy shift due to transitions $n \to n \pm 1$, we find the renormalized charging energy

$$E_c^s = E_c^0(1 + g\frac{\Delta}{E_c^0}\{\Gamma[\frac{E_c^0}{\Delta}(1+2n_g)] + \Gamma[\frac{E_c^0}{\Delta}(1-2n_g)]\}) \tag{3.3}$$

where $\Gamma(x) = \int_0^\infty K_1^2(u)e^{-xu}\,du$ and $K_1(u)$ is a Bessel function.

Using the expression for $E_c^s$, we find empirically that $E_c^0 = 254\mu$eV gives the measured $E_c$ for S1. We measure the total geometric junction area $A_{tot}$ for the samples with an estimated accuracy of $\pm 20\%$, obtaining the values in Table 3.1. Setting $E_c^0 = e^2/2C_\Sigma^0$ where $C_\Sigma^0 = C_1^0 + C_2^0 + 2C_g$ and using $2C_g \approx 80$aF, we obtain $C_1^0 + C_2^0 = 195$aF as the total unrenormalized junction capacitance for S1. Scaling this result according to $A_{tot}$ we find $C_\Sigma^0$, $E_c^0$ and finally $E_c^s$ for S2 and S3 [Table 3.1]; agreement is excellent given the uncertainties in $A_{tot}$. Due to slightly heavier oxidation, S1 has both larger $R_n$ and $A_{tot}$ than S2. Since $R_n$ varies exponentially with oxide thickness and $C_1^0 + C_2^0$ only linearly, the simple scaling with $A_{tot}$ used here seems reasonable. Fig. 3.6(d) shows the relative difference between $E_c$ and $E_c^0$ scaled by $1/g$. The results agree with theory to within our experimental accuracy, and are consistent with the presence of subgap quantum fluctuations of QPs in our samples.

Virtual QP tunneling may also play a role in subgap transport, as suggested by the softening of the JQP cycle cutoff in S2 and S3. To illustrate such effects more clearly we show a plot of the $I(V_{dc}, n_g)$ surface for S2 in Fig. 3.8(a).

The JQP resonances along the $0 \Leftrightarrow 2$ and $1 \Leftrightarrow -1$ lines and the DJQP peak at their intersection are clearly visible, but there is no sharp cutoff of the JQP process below the $1 \rightarrow 0$ ($0 \rightarrow 1$) thresholds. To rule out extrinsic effects such as self-heating or high frequency noise, we show in Fig. 3.8(b) a simulation of the current in S2 based on sequential tunneling [59] at an elevated temperature and including photon-assisted tunneling due to an electromagnetic environment with effective temperature $T_{\rm env}$=1K. Despite the extreme conditions the QP tunneling thresholds are clearly visible in the simulation, and the SSET current drops nearly to zero between the JQP and DJQP features. The absence of QP thresholds in Fig. 3.8(a) is intrinsic to the sample and calls for an explanation outside of the sequential tunneling picture.

We therefore propose a process that could allow transport along the Cooper pair resonance lines between the JQP and DJQP features as illustrated schematically in Fig. 3.7(c). If below threshold the transition $1 \rightarrow 0$ ($0 \rightarrow 1$) occurs virtually, the transitions $0 \Leftrightarrow 2$ and $2 \rightarrow 1$ ($-1 \Leftrightarrow 1$ and $1 \rightarrow 0$) are allowed, completing what we call the virtual JQP (VJQP) cycle. Similar "shake-up" processes have been discussed for normal-metal tunnel junction systems [60]. Two QP excitations are created, but two electrons are transferred through the SET, so that the VJQP process is allowed for $eV > 2\Delta$. The energy barrier $E_b$ for $1 \rightarrow 0$ ($0 \rightarrow 1$) vanishes at threshold and climbs to $E_b \approx E_c + 2\Delta$ at the DJQP peak. The process can be neglected if the allowed QP tunneling rate $\Gamma_{qp}$ is small compared to the inverse dwell time of the virtual quasiparticle: $\Gamma_{qp} \ll E_b/\hbar$. Using $\Gamma_{qp} = 4\Delta/e^2 R_n$, this becomes $R_n \gg \frac{R_K}{\pi}\frac{2\Delta}{E_b}$, which is violated for a range of voltages between the DJQP and JQP features. A detailed theoretical analysis is

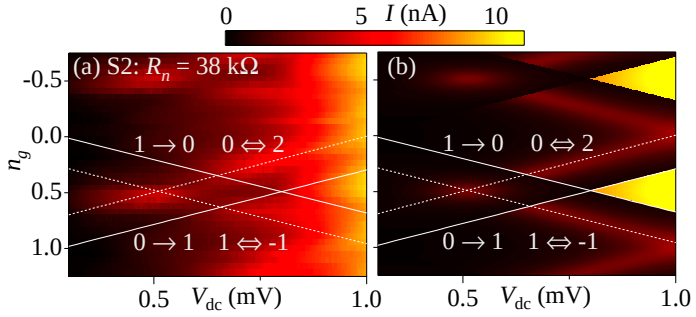


Figure 3.8 False color images of $I(V_{\rm dc}, n_g)$ for (a) S2 at T=20mK (b) a simulation at T=200mK assuming an electromagnetic environment with impedance $R_{\rm env} = 50\Omega$ and temperature $T_{\rm env} = 1K$. Cooper pair resonance lines $0 \Leftrightarrow 2$ $(-1 \Leftrightarrow 1)$ and QP tunneling thresholds $1 \rightarrow 0$ $(0 \rightarrow 1)$ are indicated by the dashed and solid lines.

required to determine the contribution of the VJQP cycle to transport.

In contrast to the QP thresholds, features associated with Cooper pair tunneling are visible in both the data and the simulation, suggesting that the number of Cooper pairs is well defined. For the JQP process at resonance, the Cooper pair tunneling rate is $\Gamma_{cp} \approx E_j^2/\hbar\Gamma_{qp} = \frac{\pi}{8}\frac{E_j}{\hbar}$ [31]. Demanding that energy broadening due to Cooper pair tunneling be small compared to the typical energy barrier $4E_c$ for virtual tunneling gives $2\hbar\Gamma_{cp}/4E_c = \frac{\pi}{16}\frac{E_J}{E_c} \ll 1$, which is easily satisfied even for S3. For S2 and S3, then, quantum fluctuations are significant for QPs but small for Cooper pairs.

We now turn to rf operation. Optimal operating conditions were selected as follows: a small charge oscillation $q_0 \approx 0.006e$ rms was applied and the SNR determined from the power spectrum of $v_r$ as in Fig. 3.5(c). Subgap operation (all samples) and above-gap operation (S1) were optimized over dc bias $V_{dc}$, rf bias

$v_{rf}$ and offset charge $Q_0$. We measured SNR versus input amplitude $q_0$ for each optimization and determined the charge sensitivity $\delta q$ using $\delta q = \frac{q_0}{\sqrt{\mathrm{BW}}} 10^{-\mathrm{SNR}/20}$ where the resolution bandwidth BW=1kHz and SNR is in dB [25].

The optimized biases for S1 and S3 are indicated in Fig. 3.6 and the results of the $\delta q$ and SNR measurements in Fig. 3.9. For S1 the best $\delta q = 9 \times 10^{-6} e/\sqrt{\mathrm{Hz}}$ was found for $V_{dc} = 860\mu V$, consistent with previous results [25]. Linearity, however, was poor: as $q_0$ increases, the measured SNR rapidly becomes sublinear, and $\delta q$ worsens [Fig. 3.9(a)]. Since $\delta q$ does not saturate even for $\delta q_0 = 4.5 \times 10^{-3} e$ rms it is unclear how small $\delta q_0$ must be to achieve linear response. For subgap operation ($V_{dc} = 600\mu$V) of S1 [Fig. 3.9(b)], we find $\delta q \approx 1.3 \times 10^{-5} e/\sqrt{\mathrm{Hz}}$, with SNR nearly linear to $q_0 \geq 0.01e$ rms. Since $\delta q$ appears close to saturation at $\delta q_0 = 3.1 \times 10^{-3} e$ rms we may have approached linear response.

For S3 the best operating point occurred at $V_{dc} = 440\mu$V [Fig. 3.9(c)], between the DJQP and JPQ features with $\delta q \approx 1.2 \times 10^{-5}$, better than that for subgap operation of S1. Moreover, linearity was vastly improved: the SNR remains linear and $\delta q$ nearly flat to $q_0 = 0.038e$ rms indicating that we have achieved linear response in this sample. For S2 (data not shown) the best $\delta q \approx 1.2 \times 10^{-5}$ also occurred subgap, and the SNR was linear to $q_0 \approx 0.02e$ rms.

We can now make some general statements about the effects of quantum fluctuations on RF-SET operation. For samples with smaller $\alpha$ such as S1, transport is fairly well described by the sequential tunneling picture: $I$-$V$ characteristics are sharp and vary strongly with $Q_0$, giving rise to excellent charge sensitivity. The same sharpness, however, prevents good linearity, since a large $q_0$ necessarily moves the SET far from optimal operation. For samples with larger $\alpha$ such as

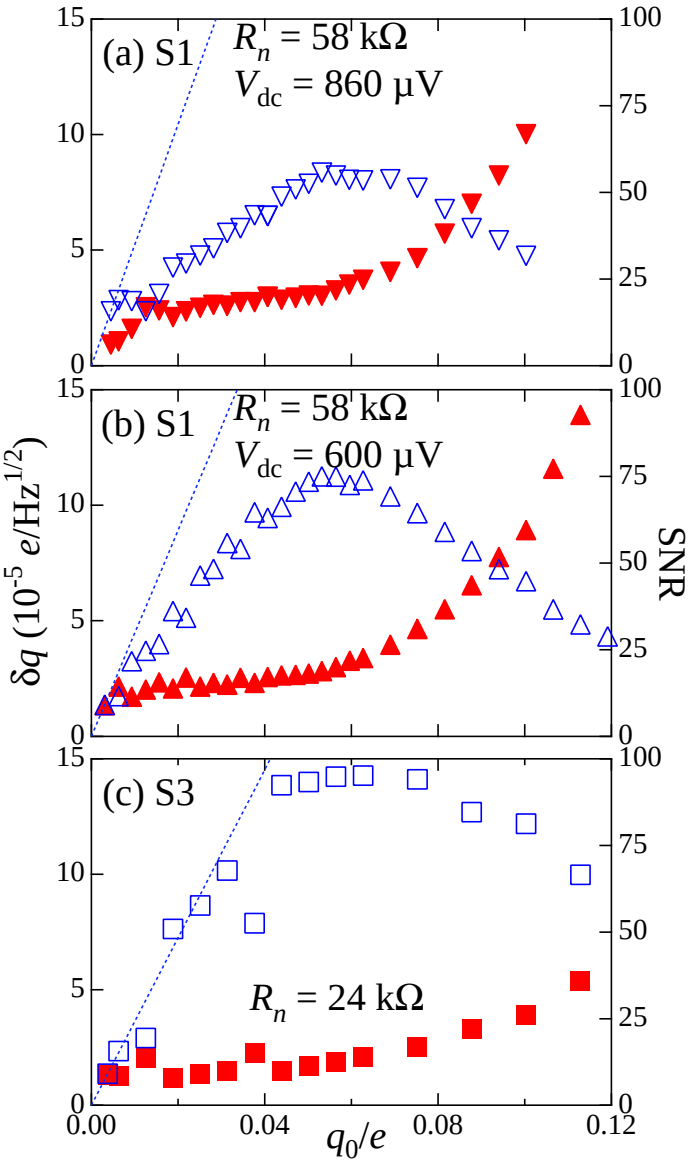


Figure 3.9 Charge sensitivity $\delta q$ and SNR (linear scale) versus $q_0$ in $e$ rms for (a) S1, above gap, (b) S1, subgap, and (c) S3, subgap. Charge sensitivity (solid red symbols) is plotted on the left axis and SNR (open blue symbols) on the right. For reference, the SNR for linear response is plotted as the dashed lines for $\delta q$ measured at the smallest $q_0$.

S3, quantum fluctuations cause at least two important effects. First, the subgap features are smoothed and broadened, improving linearity: *e.g.*, in S3 there is no "dead spot" between the DJQP and JQP features for which the SSET current is roughly independent of $Q_0$. Second, the smaller $R_n$ simplifies impedance matching between the RF-SET and the 50$\Omega$ coaxial line.

In conclusion, we have investigated the influence of quantum charge fluctuations on the charge sensitivity and SNR of RF-SETs. We find that RF-SETs with $\alpha \geq 1$–2 (strong quantum fluctuations) show both good linearity and good charge sensitivity. In contrast, RF-SETs with $\alpha < 1$ (weak quantum fluctuations) show poor linearity and only modestly better charge sensitivity. These findings assume particular importance given interest in the RF-SET as a potentially quantum-limited linear amplifier. We have achieved linear response only for subgap operation in samples with $\alpha \geq 1$ for which quantum fluctuations of quasiparticles are substantial.

# Chapter 4

## Radio-Frequency Quantum Point Contact Charge Sensor

The QPC, though one of the very simplest devices, is one of the most extensively studied. QPCs are the building blocks of the split-gate family of devices such as quantum dots realized in 2DEG heterostructures. They have been widely used as charge sensors and have been proposed as a potential candidate for the read-out of quantum bits (qubits) in quantum dot based quantum computation schemes [61–64]. Their ease of integration with split-gate quantum-dot based qubits makes them an attractive candidate over the faster, more sensitive RF-SETs. Even after decades of research, however, transport properties of QPCs such as the 0.7 structure [65–67] are not completely understood. There is a renewed interest to study noise in transport caused by the particle nature of electrons, the shot noise [68]. Due to the fact that the shot noise is subject to quantum statistics and many body interactions in a system, studying the shot noise can reveal more information about a system. Furthermore, the ultimate charge sensitivity of any sensor is limited by its noise properties. The study of shot noise [69] may therefore also reveal whether or not the QPC charge sensor can reach the quantum limit of measurement [23, 53, 70, 71].

Unlike RF-SETs, standard QPC sensors are not fast enough to detect the charge dynamics on time scales of $\approx 1\mu$s. Even though the intrinsic device band width is well in excess of hundreds of GHz, operational bandwidth is limited to a few tens of kHz by the bandwidth of the room temperature electronics and the wires and cables connecting the QPCs to room temperature electronics. In this chapter, the operation of a QPC charge sensor in the in the rf mode (RF-QPC) analogous to the RF-SET is discussed [24, 25, 32].

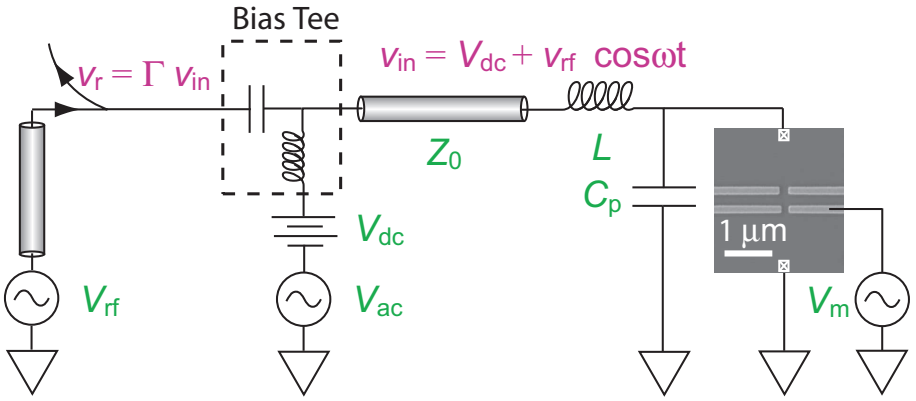


Figure 4.1 Schematic circuit diagram of RF-QPC showing the $LC$ tank circuit and the QPC. Both dc/low-frequency and rf bias can be applied to the sample with the use of a bias tee. A sinusoidal modulation can be applied to either of the gates to modulate the QPC conductance for charge sensitivity measurements.

The QPC is fabricated in a piece of GaAs/AlGaAs heterostructure containing a 2DEG located 100 nm beneath the surface, with a nominal sheet density of $1.3 \times 10^{11}\text{cm}^{-2}$ and mobility $7.4 \times 10^{6}\text{cm}^2/\text{Vs}$. The QPC is formed by applying negative voltage to the surface gates. All the measurements are performed in a dilution refrigerator with a base temperature of $\approx$ 20mK. A positive bias of approximately 300mV is applied to the surface gates while cooling the sample

from room temperature through LHe temperature to minimize charge noise in the device and also to reduce the pinch off voltage. The QPC is embedded in a tank circuit as shown in the Fig. 4.1. The tank circuit consists of a superconducting Nb inductor with $L \approx 130$nH and parasitic capacitance $C_p \approx 0.3$pF, due to the macroscopic leads and pads of the sample. This circuit configuration allows one to do both the dc/low-frequency transport and rf reflectometry . The reflected signal from the sample is amplified with a cryogenic HEMT amplifier with a noise temperature $T_n \approx 2.3$K and also by room-temperature microwave amplifiers. A cryogenic circulator isolates the the tank circuit from the cryogenic amplifier.

Conductance measurements are carried out on the QPC using the low frequency lock-in methods as illustrated in Fig. 2.14. A $20\mu$V ac signal at 13Hz is applied to the ohmic contacts while the voltage across and the current through the device is recorded as the voltage on the QPC gates is swept.

Fig. 4.2 (a) is a plot of the QPC conductance versus the gate voltage. Clear, well-formed plateaus of step size $2e^2/h$ are observed, which is a signature of a high-quality QPC. The inset of Fig. 4.2 (a) corresponds to a similar measurement taken after shining an LED on the sample. This will return all the carriers to the well that have been frozen out by the positive bias applied while cooling and also release more carriers from the DX centers, as indicated by the increased pinch off voltage and number of plateaus. Fig. 4.2 (b) is a plot of QPC conductance in the $V_{\rm dc}$-$V_g$ plane. Plateaus in this plot appears as dense regions where many curves accumulate. The peak in the conductance at zero bias, usually referred to as zero bias anomaly (ZBA), has been a topic of discussion [72, 73] and is present only at lower temperature.

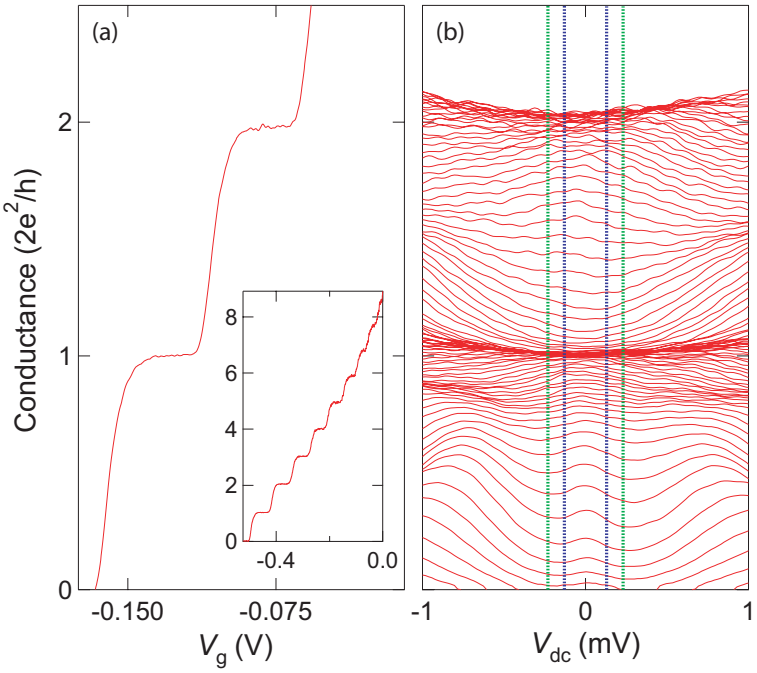


Figure 4.2 (a) Conductance of the QPC vs gate voltage showing well defined plateaus. Inset: Conductance vs gate voltage after shining an LED on the sample. (b) Non-linear transport data showing the differential conductance as a function of $V_{\rm dc}$ and the gate voltage.

Once the dc characterization is performed, the next step is to find out the resonant frequency of the tank circuit and the frequency at which the response is maximized. Fig. 4.3 is a plot of the reflected rf $v_r$ from the tank circuit versus frequency while the QPC conductance is about $0.5G_0$ (red curve) and when the QPC is completely pinched off (blue curve). The resonant frequency as is the maximum response is found to be $\approx$ 800MHz. To determine the charge sensitivity, the conductance of the QPC is modulated by applying a sine wave excitation on to one of the QPC gates so as to cause a modulation in $\triangle G$ the conductance of $\triangle G/G_{QPC} \approx 2.7\%$. This modulation is comparable to a variation in the con-

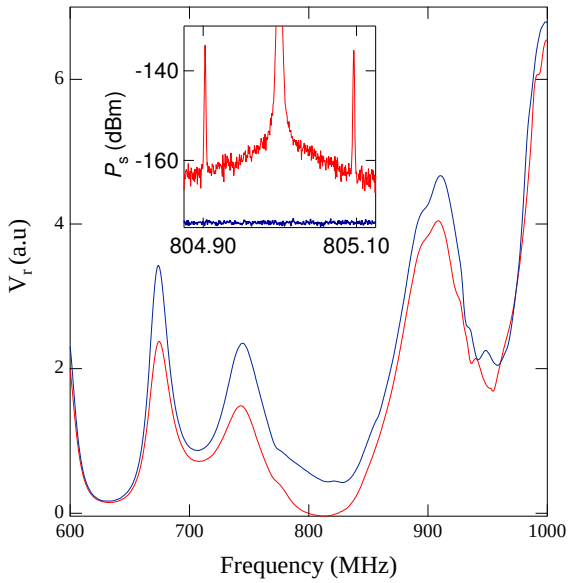


Figure 4.3 Reflected rf voltage from the tank circuit while the QPC is pinched off (blue) and while the conductance $\approx 0.5G_0$ (red). Inset: Representative power spectrum of reflected carrier wave amplitude modulated by a 97kHz voltage oscillation on one of the QPC gates. The blue curve represents the noise floor of the cryogenic HEMT amplifier.

ductance due to charge motion in a nearby quantum dot. A power spectrum of the resulting reflected wave referred to the input of the cryogenic amplifier is shown as an inset in Fig. 4.3. The reflected power spectrum shows sidebands displaced from the carrier wave by the modulation frequency $\pm$97kHz which is a clear signature of amplitude modulation. The charge sensitivity of the RF-QPC $\approx 5\times10^{-4}e/\sqrt{\text{Hz}}$, referred to a typical quantum dot. The noise floor in the charge sensitivity measurement is roughly -160 dBm, significantly above the white noise floor of the HEMT amplifier (-165dBm for this resolution bandwidth), shown as the blue curve in the inset to Fig. 4.3. To see the noise floor of the RF-QPC more

clearly the bandwidth of the noise measurement is increased to roughly 10 MHz, as shown in Fig. 4.4 (a).

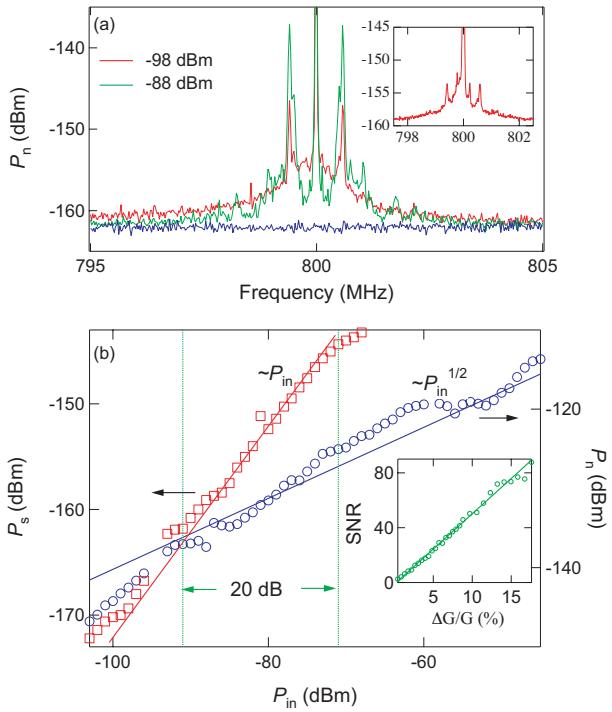


Figure 4.4 (a) Reflected noise power spectrum for $P_n = -98$dBm (red) and -88dBm (green) curve. The blue curve shows the noise floor of the cryogenic HEMT amplifier. Inset: The asymmetry observed for low input powers while the electron concentration/pinch-off voltage was very low. (b) A plot of the noise power integrated over a frequency band of 4.8MHz (blue open circles) and charge oscillation signal $P_s$ induced by a sinusoidal oscillation on one of the QPC gate (red open squares) vs input power $P_{\rm in}$. The red and blue straight lines are a guide to the eye. Inset: Linearity of RF-QPC amplifier; plot of SNR vs input conductance modulation.

In the vicinity of the carrier wave there is a clear increase in the noise above the HEMT amplifier white noise. This increased noise is clearly frequency dependent, being largest closest to the carrier wave, and increasing in magnitude as the input

power $P_{in}$ is raised. For the lowest input power of about -103dBm referred to the input of the cryogenic amplifier the overall noise spectrum is asymmetric as shown in the inset of Fig. 4.4(a) . As the input power is increased two things happen: the asymmetry vanishes, and a redistribution of the power in the frequency spectrum takes place. The noise floor closer to the carrier wave rises, while the noise floor away from carrier wave lowers as illustrated by the red ( $P_{in}$=-98dBm) and green ( $P_{in}$=-88dBm) curves in Fig. 4.4(a). The intrinsic bandwidth of the resonant circuit can cause a rise in the noise floor within the resonance. But, the bandwidth is too large ($\approx$ 60MHz) and cannot account for the observations made in Fig. 4.4(a). If this was the case, then the power spectrum would change with the carrier frequency. Yet, according to our observations, the power spectrum retains its shape as long as the carrier frequency is within the resonance. The blue curve in Fig. 4.4(a) is the noise floor of the cryogenic amplifier shown for reference.

To characterize the reflected power spectrum, the integrated noise power $P_n$ in a 4.8MHz band above the carrier frequency, and the power $P_s$ due to a conductivity modulation are measured versus the input power $P_{in}$ as shown in Fig. 4.4 (b). As expected for amplitude modulation, $P_s$ varies linearly with $P_{in}$ over roughly three decades in input power. In contrast, $P_n$ varies as $\sqrt{P_{in}}$ for roughly five decades in $P_{in}$. This immediately eliminates any form of modulation noise including some random charge fluctuations in the substrate, as the source of $P_n$. Furthermore, amplitude modulation always generates a symmetric power spectrum, unlike what has been observed. The inset of Fig. 4.4 (b) is a plot of the SNR of the RF-QPC versus the percentage change in conductance due to a sinusoidal voltage on one of the QPC gates. The RF-QPC sensor has excellent linearity over a wide range

of input signal amplitude.

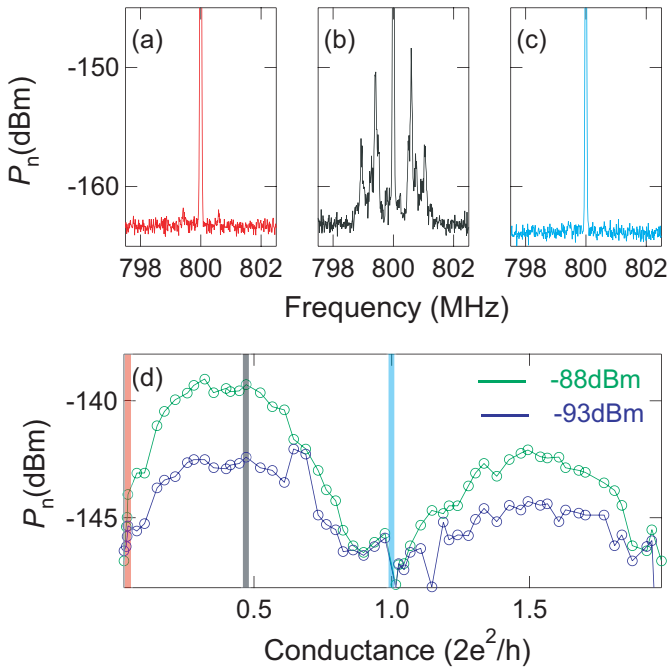


Figure 4.5 (a) The noise power spectra while the QPC is completely pinched off, (b) while the conductance is $\approx 0.5G_0$ and, (c) while the conductance is $2e^2/h$. (d) Integrated noise power from $P_{\text{in}}$=-93dBm (blue) and for -88dBm (green). The amplitude of the rf bias at these two input powers are highlighted by blue and green vertical dashed-lines in Fig. 4.2 (b).

According to the theory of photon assisted shot noise (PAS) [74, 75], the noise power spectra $S_I$ of QPC subject to an ac driving voltage is given by

$$S_I = \frac{2e^2}{h} \sum_{n=-\infty}^{\infty} J_n^2(eV_{ac}/\hbar\omega_0) \sum_i T_i(1-T_i)$$
$$\{(\hbar\omega + n\hbar\omega_0 + eV)coth[\frac{\hbar\omega + n\hbar\omega_0 + eV}{2k_BT}] +$$

$$(\hbar\omega + n\hbar\omega_0 - eV)coth[\frac{\hbar\omega + n\hbar\omega_0 - eV}{2k_BT}]\} \tag{4.1}$$

where $\omega$ and $\omega_0$ are the drive and measurement frequencies, $T_i$ is the transmission probability of $i$th channel, $V_{ac}$ is the ac bias across the QPC, and $J_n(x)$ is a Bessel function of the first kind. Acoording to Eq. 4.1 PAS strongly depends on the transmission probability of the QPC: the noise power will be a minimum when the channels are completely open or fully closed and maximum for a half-open channel. A measurement of the integrated noise power versus the QPC conductance is given in Fig. 4.5 (d). Fig. 4.5 (a)-(c) are representative noise power spectra when the QPC is pinched-off (red) when the QPC conductance $\approx 0.5G_0$ and when the QPC conductance is $2e^2/h$. From this it is easy to see that the behavior of the noise power $P_n$ depends on the device characteristics and qualitatively follows the theory of photon assisted shot noise: the noise is largest between the plateaus and drops down below the cryogenic amplifier noise floor on the plateaus.

In conclusion, rf operation of a QPC charge sensor in a mode similar to that used for RF-SETs has been successfully implemented. Unlike the existing rf measurements [25, 27, 32] where the detector sensitivity was determined by noise of a secondary amplifier, the sensitivity of RF-QPC is determined by the non-equilibrium device noise of the QPC itself.

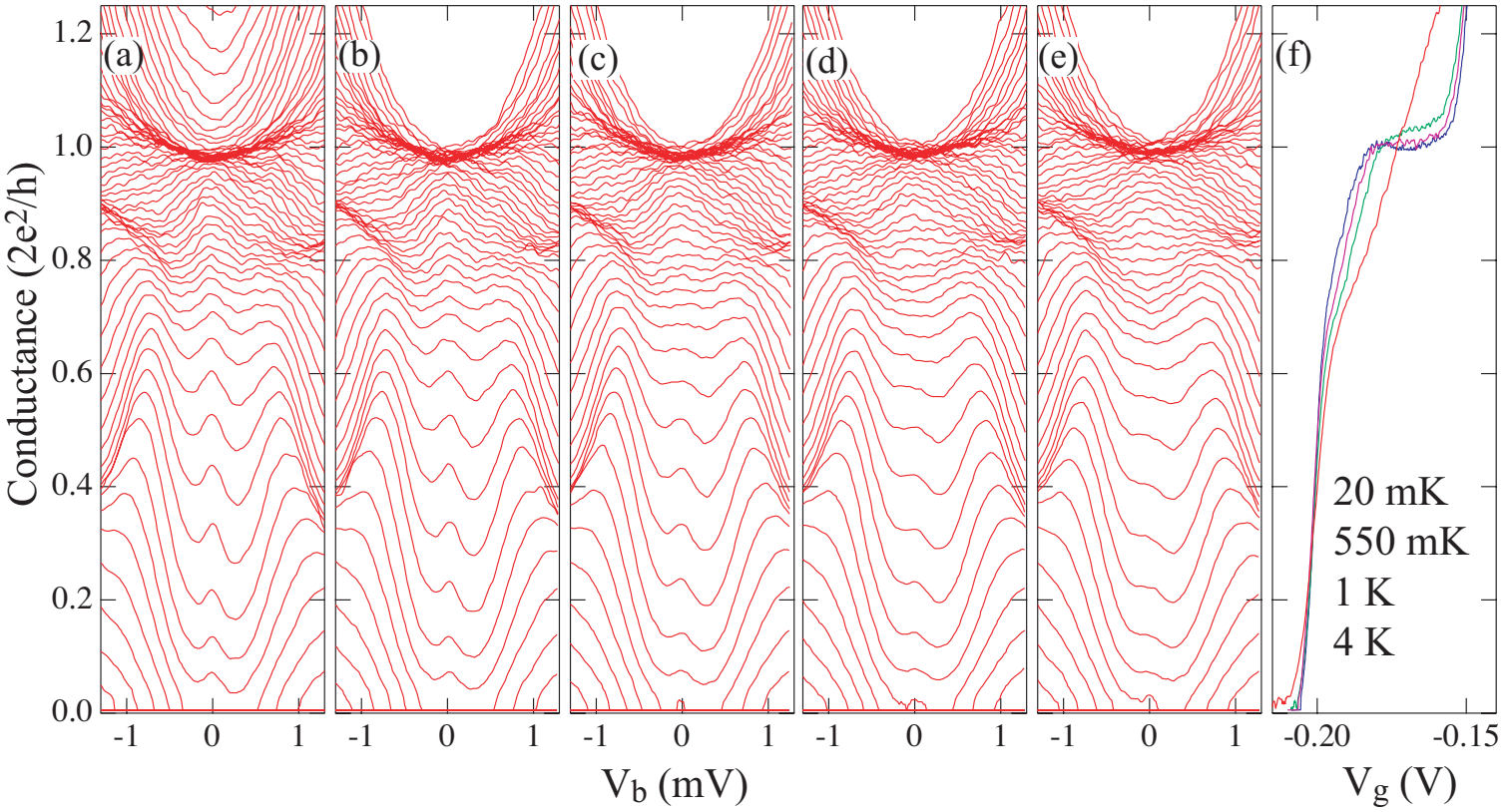


Figure 4.6 Nonlinear transport through the QPC at (a) 25 mK, (b) 115 mK, (c) 255 mK, (d) 420 mK, and (e) 550 mK showing differential conductance as a function of drain source voltage $V_{\rm dc}$ for various gate voltages. (f) Conductance vs gate voltage at zero bias for various mixing chamber temperatures as indicated in the plot. The gradual disappearance of the ZBA and the strengthening of 0.7 shoulder with rise in temperature can be noticed.

The temperature dependence of the QPC noise characteristics and the transport properties are discussed next. Fig. 4.6 represents QPC nonlinear conductance at various mixing chamber temperatures. The main observation that one can make from these plots is the behavior of the ZBA versus temperature. The ZBA gradually fades away as the temperature is increased. Fig. 4.6(f) represents QPC conductance versus gate voltage taken at various mixing chamber temperatures. The shoulder below the last plateau, the 0.7 structure, becomes more prominent as the temperature is increased. By looking at Fig. 4.6 one can come to the conclusions that the 0.7 structure and the ZBA are closely linked to each other and that they are complementary. The high bias regions are not affected very much by the rise in temperature. Fig. 4.7 (a) is a plot of the nonlinear transport data from extracted from Fig. 4.6 (a) through (e) showing the behavior of ZBA around the $0.5G_0$ conductance for various mixing chamber temperatures.

The QPC noise power spectrum for $P_{in} = -98$dBm referred to the cryogenic amplifier for various temperatures is given in Fig. 4.7 (b). The noise power spectrum shows very strong asymmetry at lower temperatures. As the temperature increases to around 500mK the asymmetry completely vanishes. Furthermore, broadband noise seen around the carrier wave also vanishes considerably by this temperature. Both the asymmetry and the broadband noise are completely washed out when the temperature reaches around 775mK. The ZBA also disappears at around the same temperature as evident from Fig. 4.7 (a). The inset shows the conductance at zero bias at 25mK and also at 550mK.

Fig. 4.8 (a) is a plot of the nonlinear transport data at selected conductance points at 25mK (blue) and at 550mK (red). Fig. 4.8 (b) and (c) and the noise

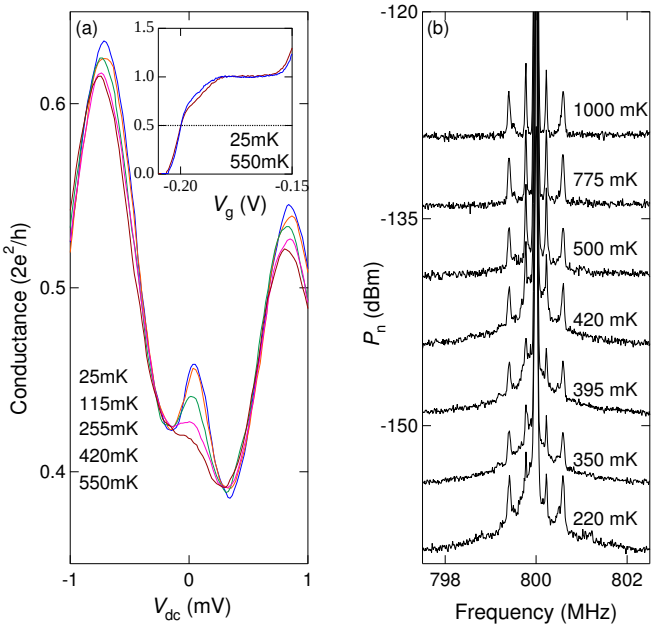


Figure 4.7 (a) Nonlinear transport: Conductance versus the source drain voltage $V_{\rm dc}$ extracted from Fig. 4.6 for QPC conductance $\approx 0.5G_0$ at various mixing chamber temperatures. Inset: QPC conductance showing the pinch-off and the first plateau at 25mK (blue) and 500mK (brown). (b) QPC noise spectra for $P_{\rm in}$=-103dBm for various mixing chamber temperatures.

power integrated over a narrow frequency band of 150kHz very close to the carrier wave versus $P_{in}$ at 20 mK and 550 mK respectively. For input powers of about ≈-98dBm the $P_n$ at 25mK is higher than that at 550mk. This observation is consistent with that of Fig. 4.7(b) and 4.4(a). To put it briefly, close to the carrier frequency the noise power at lower input powers is higher than that at higher input powers. Also, the noise power at a mixing chamber temperature of 20mK is higher than that at 550mK. From the above observations one can make a few statements about the noise characteristics.

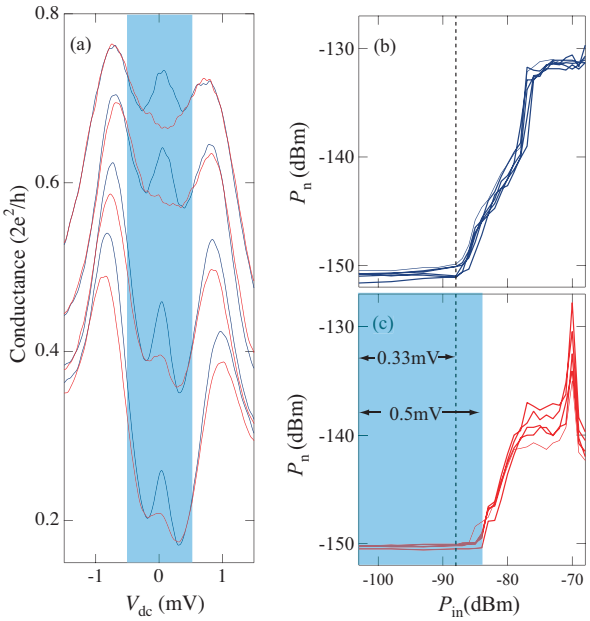


Figure 4.8 (a) Plot of the QPC conductance vs the source drain bias $V_{\rm dc}$ at a few selected gate voltages, at 25mK (blue) and at 550mK (red). (b) The noise power integrated over a narrow band of 150kHz close to the carrier wave vs $P_{\rm in}$ at 550mK. (c) The noise power integrated over a narrow band of 150kHz close to the carrier wave vs $P_{\rm in}$ at 25mK

- The observed noise properties are more prominent at lower temperatures where the ZBA anomalies are present.
- The noise characteristics do not seem to have any thermal origin since they are weaker or almost absent at higher temperature.
- As the thermal energy difference between 22mK and 500mK is not very significant, emergence of the noise at lower temperature suggests that its origin is likely quantum mechanical in nature.

To further investigate this problem one would need to carryout magnetic field studies of the noise. Our present experimental setup will not allow us to successfully carryout such a study since the superconducting chip inductor in the tank circuit will turn normal at field of a couple of hundreds of mT. In conclusion, the study of the high-frequency QPC transport allows one to probe the device with a very small rf bias and without driving a dc current through the device, while all of the existing studies involve driving a substantial current through the device which might washout delicate features. Features such as ZBA and 0.7 structure cannot be reached once the QPC is away from the zero bias. By the use of carefully tuned on-chip impedance matching circuit one can probe the device more effectively.

# Chapter 5

## Double Quantum Dot System Coupled to Superconducting Single Electron Transistor for Back-Action Studies

The experiments discussed in this chapter are an attempt to implement the ideas discussed in Section 1.6. Both the SET and QPC are charge detectors having the potential to operate at or close to the quantum limit. A study of the noise characteristics alone can not determine whether the device is operating at the quantum limit; a characterization of the back-action is also necessary. The product of charge sensitivity and back action must be $\geq \hbar$ as discussed in Table 1.1. A DQD system when properly tuned can be used as a spectrum analyzer for high frequency noise associated with its electromagnetic environment [42], which is the main idea behind the experiments discussed in this chapter.

### 5.1 The story so far

A brief re-visit to the previous measurements on a DQD/RF-SET device is required to keep the continuity [76]. Fig. 5.1 is an SEM micrograph of DQD/RF-SET device. The SSET is electrostatically coupled to one of the dots, QD1. Flaws

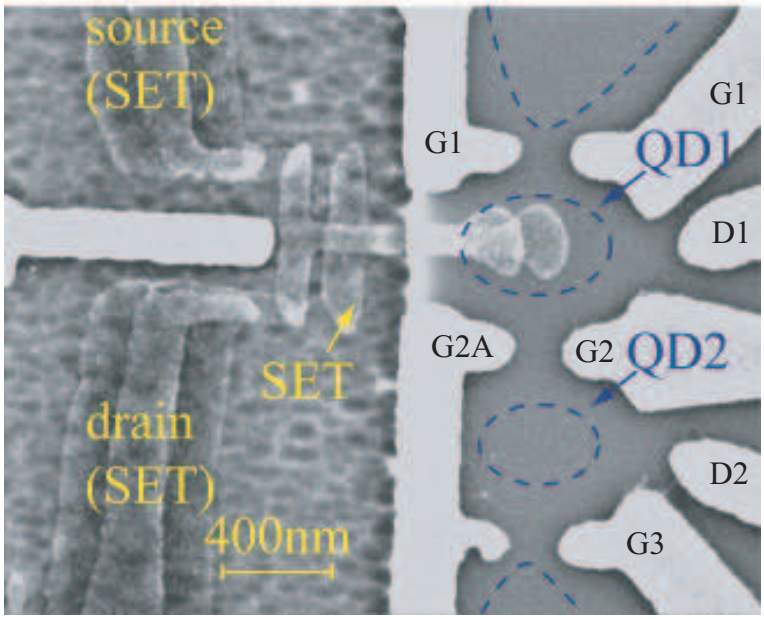


Figure 5.1 SEM micrograph of DQD/RF-SET device.

in the dot gates prevented us from performing a measurement of the resonant tunneling current through the DQD system. The lithographic sizes of the dots are of the order of 650 nm in diameter. Once all the gates are energized the sizes of the dots are of the order of 450nm in diameter. To reach the single particle regime the dots must be significantly smaller, of the order of 250nm or so in diameter, requiring substantially higher voltages on all the gates defining the tunnel barriers and the gates. This results in very thick tunnel barriers and practically no current through the dots, even if the 0D levels are aligned. The gap between the bottom electrodes G1 and G2A on the QD1 requires a much higher voltages than that on the top ones for the formation of a reasonable dot. But this makes the tuning of the QD2 difficult because the G2A is common to

both dots and it does not actually require such a higher voltage on that gate to exhibit a reasonably good dot behavior. Second, the gates of the dots are very much coupled to the QPCs forming the tunnel barriers. This made it very difficult finding nice working conditions on the DQD since a small change in the voltage on one gate would affect all the tunnel barriers and would shift the working point significantly. Due to all these problems we were not able to use the DQD as a spectrum analyzer to study the back-action of the RF-SET.

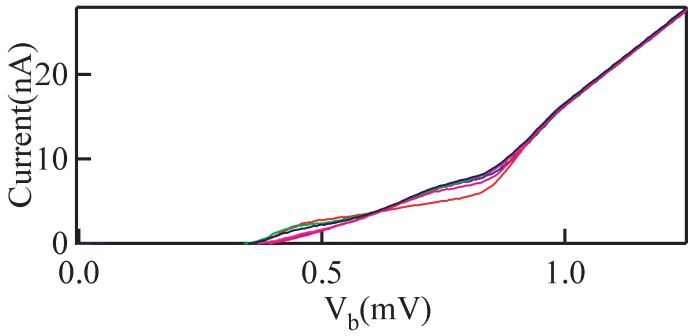


Figure 5.2 $I$-$V$ characteristics of SSET shown in Fig. 5.1.

We did, however, observe other interesting effects of the SET back action on the DQD system. Fig. 5.2 is plot of the SET $I$-$V$ characteristics.

Fig. 5.3 shows a series of Coulomb blockade oscillation of the DQD with the SET at various biases. Comparing those to the one at zero bias one can see the effect of SET bias on the DQD performance. When the SET is at the center of the gap the current through the DQD is very small and the peak splitting is clearly visible. As we move to higher bias, the DQD current is substantially higher and the shape of the peaks also changes. Moreover there is a small decrease in the

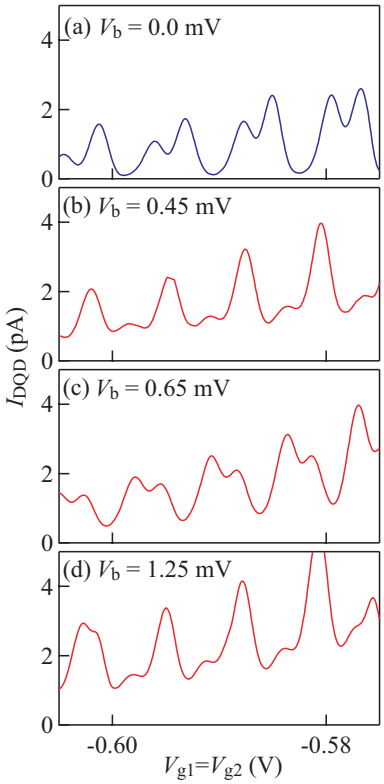


Figure 5.3 Current through the DQD vs the voltage on the common gate. while SET bias is (a )0.0mV, (b) 0.45mV, (c) 0.65mV, (d)1.25mV.

period of the oscillations. The increase in the current through the DQD suggests that there is some kind of inelastic process going on in the DQD environment. Recalling the fact that fractional peak splitting depends on the inter-dot coupling, it seems possible that the electron dynamics in the DQD is affected by the current through the SET. In addition, the disappearance in the fractional peak splitting is not monotonic. It comes and goes as the SET bias is varied. Although we can not make any quantitative statements about this effect, it is clear that the DQD is sensitive to the current through the SET.

## 5.2 New experiments on DQD/RF-SET system *

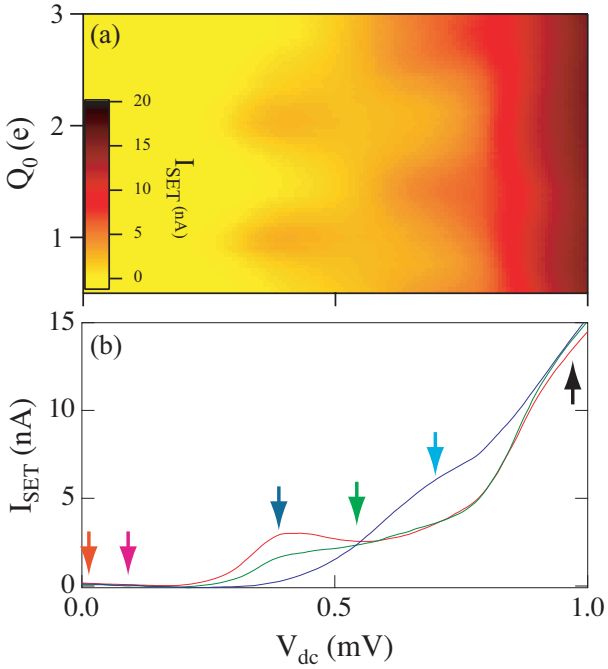


Figure 5.4 (a) A plot of current through the SET in the $V_b$-$V_g$ plane. (b) $I$-$V$ characteristics of the SET shown in Fig. 5.8. The arrow-marks are color-coded with the curves in the inset to Fig. 5.6.

Fig. 5.4 represents the $I$-$V$ characteristics of the SSET in the new DQD/RF-SET device. The inset shows a false-color plot of the current through SSET in the $V_b$-$V_g$ plane.

Fig. 5.5 (a) is a cartoon of a DQD system in the few electron regime. Fig. 5.5 (b) and (c) are plots of the current through the quantum dots QD1 and QD2 respectively versus dc bias. The step like behavior is a signature of the presence

*A brief discussion of this work can be found in [77]

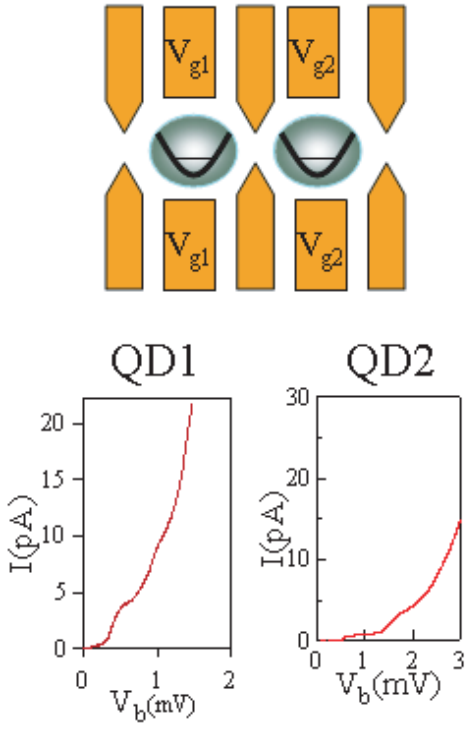


Figure 5.5 (a) A cartoon showing a few electron DQD. (b) $I$-$V$ characteristics of QD1 showing the 0D levels. (c) $I$-$V$ characteristics of QD2 showing the 0D levels.

of 0-D levels in the dots which is a primary requirement to observe the resonant tunneling current [78].

Fig. 5.6 is a plot of the resonant tunneling current through the DQD as the gate of QD1 is swept while SSET is biased at the center of the superconducting gap. A sharp Lorentian like peak in the current is due to the resonant tunneling of electrons through the DQD system. The inset shows similar measurements performed while the SSET is at various biases as represented by the arrows in

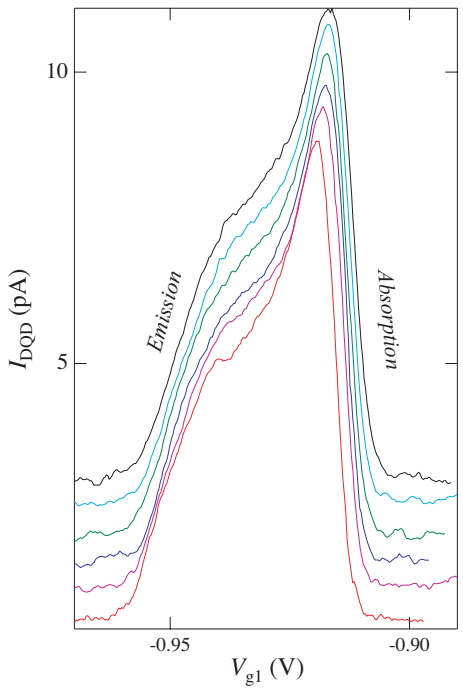


Figure 5.6 Resonant tunneling current through DQD: dc current through the DQD vs QD1 gate voltage while the SET is biased at various operating voltages as represented by the arrows in Fig. 5.4. The curves are color-coded with the arrows in Fig. 5.4 and are offset in the y-axis for clarity.

Fig. 5.4. The arrows in Fig. 5.4 and the curves shown in the inset to Fig. 5.6 are color coded for clarity. The current through the DQD does not seem to be affected by the SSET operating conditions, which is in stark contrast with the observations discussed in the previous section. One main reason could be the lack of proper coupling between the SSET and the DQD.

We measured the CB oscillations of the SET by sweeping the D1, when the QD1 is formed, as shown in Fig. 5.7(c). The data exhibit doubly periodic oscillations[79]. The faster oscillations are due to the single electron charging of the QD1 while the slower ones are due to the direct coupling of the gate to the SET.

Fig. 5.7(b) shows the result of a similar measurement performed on the device depicted in Fig. 5.1. The relative strength of the faster oscillation is a direct measure of the coupling between the QD1 and SET.

Comparing Fig. 5.7(b) and (c) it is clear that the coupling is relatively weak for the device which is in agreement with the data shown in Fig. 5.6. An SEM micrograph taken after the experiment shown in Fig. 5.8 reveals that there is indeed a break in antenna coupling the QD1 and the SSET.

In conclusion the resonant tunneling current through the DQD was measured successfully but the lack of coupling prevented the measurement of the noise characteristics and back-action of the SET. The steeper absorption side of the spectra shown in Fig. 5.6 indicates that the electromagnetic environment of the DQD is relatively noise free and the major source of noise is the SET.

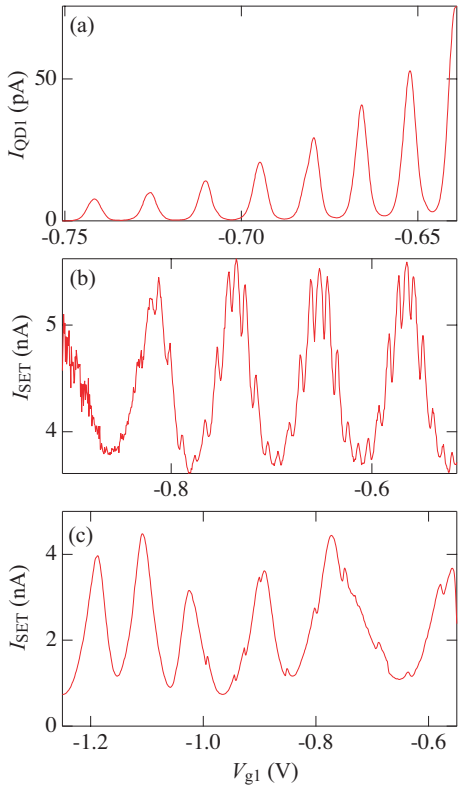


Figure 5.7 (a) CB oscillations of QD1. (b) Current through the SET vs the voltage on gate D1 while the QD1 is formed for the device shown in Fig. 5.1.(c) Current through the SET vs the voltage on gate D1 while the QD1 is formed for the device shown in Fig. 5.1. The faster oscillations are due to the single electron charging of the QD1 while the slower ones are due to the direct coupling of the gate to the SET.

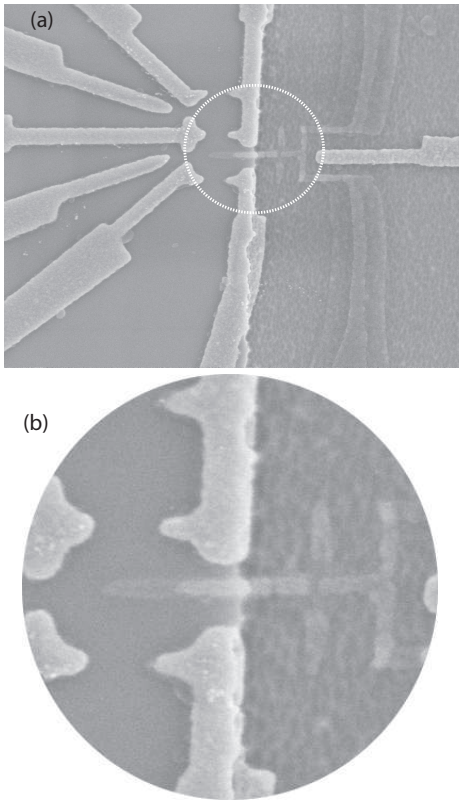


Figure 5.8 (a) SEM micrograph of the DQD/RF-SET device. (b) An enlarged view of the SET island which shows a break in the antenna coupling the QD1 and the SET.

# Chapter 6

## Conclusion and Future Works

Quantum charge measurement and the study of back action is a very important problem both from the fundamental physics and technological point of view. Both SET and QPC are regarded as potential candidates to readout the charge states of qubits in the solid state implementation of quantum computers. The non-equilibrium noise characteristics of SETs and QPCs can be very different and depend on the operating conditions of the device. The method of studying the transport properties of the device by rf reflectometry as discussed in Ch.4, opens up a completely new avenue which was not accessible by the conventional $I$-$V$ measurements. To study the noise characteristics by the conventional $I$-$V$ measurement one has to drive an appreciable amount of dc current through the system which requires the device to be away from zero bias which is not useful in the study of features such as ZBA and 0.7 structure etc.

As discussed in Ch. 5. to study whether the device is operating at the quantum limit or not one needs to quantify both the back action and the noise/sensitivity. The initial experiments on DQD/RF-SET gave qualitative evidence of SET back action. In the later experiment the coupling between SET and DQD was not good enough and the transport through the DQD was not affected by the SET operating condition. One prime requirement to measure the resonant tunneling

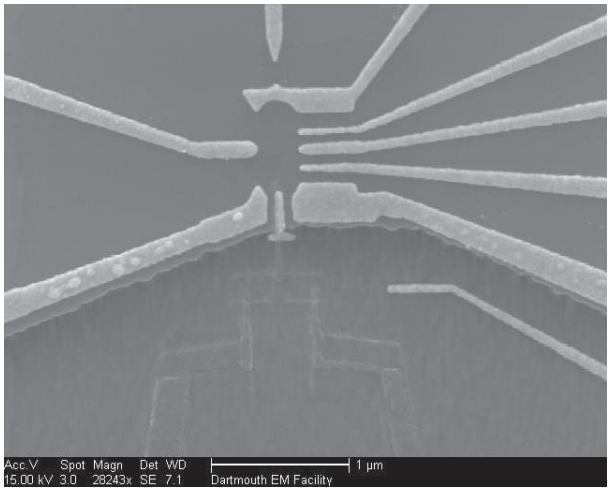


Figure 6.1 An SEM micrograph of the DQD system with integrated SET and QPC charge sensors.

current is to form a few electron double quantum dot with reasonably thin tunnel barriers to the leads. This led to a few modifications in the sample design such as the use of a shallower 2DEG heterostructure and a complete redesign of the surface gates forming the DQD. Fig. 6.1 shows an SEM micrograph of the new DQD device coupled to two integrated charge sensors. This device can be used for a variety of experiments such as the study of real-time dynamics of electrons in the DQDs and the study of back action of SET and QPC using the DQD.

## Bibliography


[1] E Corcoran et al. Diminishing dimensions. *Sci. Am.*, November:122, 1990.

[2] T. Ando et al. Electronic properties of two-dimensional systems. *Rev. Mod. Phys.*, 54:437, 1982.

[3] M.A. Kastner. Artificial atoms. *Physics Today*, 46:24, 1993.

[4] M. A. Kastner. The single-electron transistor. *Rev. Mod. Phys.*, 54:849, 1992.

[5] S. Datta. *Electronic Transport in Mesoscopic Systems*. Cambridge University Press, Cambridge, 1995.

[6] John H. Davies. *The Physics of Low-dimensional Semiconductors*. Cambridge University Press, Cambridge, 1998.

[7] C. R. Bolognesi. InAs channel HFETs : current status and future trends. *URSI International Symposium on Signals, Systems, and Electronics*, page 56, 1998.

[8] D. V. Lang and R. A. Logan. Trapping characteristics and a donor-complex (DX) model for the persistent-photoconductivity trapping center in $Te-$doped $Al_xGa_{1-x}As$. *Phys. Rev. B.*, 19:1015, 1979.

[9] P. M. Mooney. Deep donor levels (DX centers) in iii-v semiconductors. *J. Appl. Phys.*, 67:R1, 1990.

[10] S. Adachi. GaAs, AlAs, and $Al_xGa_{1x}$ as material parameters for use in research and device applications. *J. Appl. Phys.*, 58:R1, 1985.

[11] J. Singh. *Semiconductor Devices: An Introduction*. McGraw-Hill, Inc., New York, 1994.

[12] S. M. Sze. *Physics of Semiconductor Devices*. Wiley, New York, 1969.

[13] E. F. Schubert et al. Dopant distribution for maximum carrier mobility in selectively doped $Al_{0.30}Ga_{0.70}As$/GaAs heterostructures. *Appl. Phys. Lett.*, 54:1350, 1989.

[14] A. D. Stone and A. Szafer. What is measured when you measure a resistance?The Landauer formula revisited. *IBM J. Res. Dev.*, 32:384, 1988.

[15] D. A. Wharam et al. One-dimensional transport and the quantisation of the ballistic resistance. *J. Phys. C*, 21:L209, 1988.

[16] C. G. Smith et al. The transition from one- to zero-dimensional ballistic transport. *J. Phys. C*, 21:L893, 1988.

[17] B. J. van Wees et al. Quantum ballistic and adiabatic electron transport studied with quantum point contacts. *Phys. Rev. B.*, 43:12431, 1991.

[18] T. Chakraborty. *Quantum Dots: A Survey of Properties of Artificial Atoms*. North-Holland, North-Holland, 1999.

[19] L. P. Kouwenhoven et al. Few-electron quantum dots. *Rep. Prog. Phys.*, 64:701, 2001.

[20] S. M. Reimann et al. Electronic structure of quantum dots. *Rev. Mod. Phys.*, 74:1283, 2002.

[21] L. P. Kouwenhoven et al. *Electron Transport in Quantum Dots,* Nato ASI *conference proceedings.* Kluwer, Dordrecht, 1997.

[22] H. van Houten et al. *Single Charge Tunneling,* Ed. by H. Grabert and M. H. Devoret. Plenum, New York, 1992.

[23] M.H. Devoret and R.J. Schoelkopf. Amplifying quantum signals with the single-electron transistor. *Nature*, 406:1039, 2000.

[24] R. J. Schoelkopf et al. The radio-frequency single-electron transistor ($RF-SET$): A fast and ultrasensitive electrometer. *Science*, 280:1238, 1998.

[25] A. Aassime et al. Radio-frequency single-electron transistor: Toward the shot-noise limit. *Appl. Phys. Lett.*, 79:4031, 2001.

[26] A. Aassime et al. Radio-frequency single-electron transistor as readout device for qubits: Charge sensitivity and backaction. *Phys. Rev. Lett.*, 86:3376, 2001.

[27] W. Lu et al. Real-time detection of electron tunneling in a quantum dot. *Nature*, 423:422, 2003.

[28] Christoph Wasshuber. *Computational Single Electronics.* Springer-Verlag, New York, 2001.

[29] S. L. Pohlen. *Computational Single Electronics.* Ph.D Thesis, Harvard University, 2000.

[30] V. Ya. Aleshkin et al. *Physica B*, 165-166:949, 1990.

[31] D. V. Averin et al. *JETP Lett.*, 50:367, 1989.

[32] M. Thalakulam et al. Sensitivity and linearity of superconducting radio-frequency single-electron transistors: Effects of quantum charge fluctuations. *Phys. Rev. Lett.*, 93:066804, 2004.

[33] T. A Fulton et al. Observation of combined Josephson and charging effects in small tunnel junction circuits. *Phys. Rev. Lett.*, 63:1307, 1989.

[34] A. Maassen van den Brink et al. Combined single-electron and coherent-Cooper-pair tunneling in voltage-biased Josephson junctions. *Phys. Rev. Lett.*, 67:30, 1991.

[35] P. Hadley et al. 3e tunneling processes in a superconducting single-electron tunneling transistor. *Phys. Rev. B.*, 58:15317, 1998.

[36] W. G. van der Wiel et al. Electron transport through double quantum dots. *Rev. Mod. Phys.*, 75:1, 2003.

[37] K. A. Matveev et al. Tunneling spectroscopy of quantum charge fluctuations in the coulomb blockade. *Phys. Rev. B.*, 53:1034, 1996.

[38] K. A. Matveev et al. Coulomb blockade of tunneling through a double quantum dot. *Phys. Rev. B.*, 54:5637, 1996.

[39] F. R. Waugh et al. Single-electron charging in double and triple quantum dots with tunable coupling. *Phys. Rev. Lett.*, 75:705, 1995.

[40] John M. Golden and Bertrand I. Halperin. Relation between barrier conductance and coulomb blockade peak splitting for tunnel-coupled quantum dots. *Phys. Rev. B.*, 53:3893, 1996.

[41] T. Fujisawa et al. Spontaneous emission spectrum in double quantum dot devices. *Sceince*, 282:932, 1998.

[42] R. Aguado et. al. Double quantum dots as detectors of high-frequency quantum noise in mesoscopic conductors. *Phys. Rev. Lett.*, 84:1986, 2000.

[43] A. C. Anderson. Elementary dilution refrigeration. *Rev. Sci. Instrum.*, 41:1446, 1970.

[44] O. V. Lounasmaa. Dilution refrigeration. *J. Phys. E; Sci. Instrum.*, 12:668, 1979.

[45] Guy K. White and Philip Meeson. *Experimental Techniques in Low-Temperature Physics*. Oxford Science, Oxford, 2002.

[46] Physics department at university of washington. www.phys.washington.edu/users/vilches/LOWTEMP/.

[47] D. M. Pozar. *Microwave Engineering*. John-Wiley, New Jersey, 2005.

[48] A. A. Clerk et al. Resonant cooper-pair tunneling: Quantum noise and measurement characteristics. *Phys. Rev. Lett.*, 89:176804, 2002.

[49] A. Maassen van den Brink. Quantum-efficient charge detection using a single-electron transistor. *Europhys. Lett.*, 58:562, 2002.

[50] K. W. Lehnert et al. Quantum charge fluctuations and the polarizability of the single-electron box. *Phys. Rev. Lett.*, 91:106801, 2003.

[51] K. W. Lehnert et al. Measurement of the excited-state lifetime of a microelectronic circuit. *Phys. Rev. Lett.*, 90:027002, 2003.

[52] Yu. Makhlin et al. Quantum-state engineering with Josephson-junction devices. *Rev. Mod. Phys.*, 73:357, 2001.

[53] Carlton M. Caves. Quantum limits on noise in linear amplifiers. *Phys. Rev. D.*, 26:1817, 1982.

[54] A. N. Korotkov and M. A. Paalanen. Charge sensitivity of radio frequency single-electron transistor. *Appl. Phys. Lett.*, 74:4052, 1999.

[55] G. Johansson et al. Full frequency back-action spectrum of a single-electron transistor during qubit readout. *Phys. Rev. Lett.*, 88:046802, 2002.

[56] M. S. Choi et al. Shot noise for resonant Cooper pair tunneling. *Phys. Rev. Lett.*, 87:116601, 2001.

[57] D. V. Averin et al. Resonant tunneling through a macroscopic charge state in a superconducting single electron transistor. *Phys. Rev. Lett.*, 78:4821, 1997.

[58] P. Joyez et al. Strong tunneling in the single-electron transistor. *Phys. Rev. Lett.*, 79:1349, 1997.

[59] W. Lu et al. Charge transport processes in a superconducting single-electron transistor coupled to a microstrip transmission line. *Phys. Rev. B.*, 65:060501, 2002.

[60] D. V. Averin et al. Ultimate accuracy of single-electron dc current standards. *J. Appl. Phys.*, 73:1297, 1993.

[61] J. M. Elzerman et al. Few-electron quantum dot circuit with integrated charge read out. *Phys. Rev. B.*, 67:161308, 2003.

[62] J. M. Elzerman et al. Single-shot read-out of an individual electron spin in a quantum dot. *Nature*, 430:431, 2004.

[63] J. R. Petta et al. Coherent manipulation of coupled electron spins in semiconductor quantum dots. *Science*, 309:2180, 2005.

[64] S. Gustavsson et al. Counting statistics of single electron transport in a quantum dot. *Phys. Rev. Lett.*, 96:076605, 2006.

[65] K.J. Thomas et al. Possible spin polarization in a one-dimensional electron gas. *Phys. Rev. Lett.*, 77:135, 1996.

[66] A. Kristensen et al. Bias and temperature dependence of the 0.7 conductance anomaly in quantum point contacts. *Phys. Rev. B.*, 62:10950, 2000.

[67] D. J. Reilly. Phenomenological model for the 0.7 conductance feature in quantum wires. *Phys. Rev. B.*, 72:033309, 2005.

[68] L. DiCarlo et al. Shot-noise signatures of 0.7 structure and spin in a quantum point contact. *Phys. Rev. Lett.*, 97:036810, 2006.

[69] Ya. M. Blanter and M. Buttiker. Shot noise in mesoscopic conductors. *Physics Reports*, 336:1, 2000.

[70] A. N. Korotkov. Output spectrum of a detector measuring quantum oscillations. *Phys. Rev. B.*, 63:085312, 2001.

[71] Alexander Shnirman and Gerd Schon. Quantum measurements performed with a single-electron transistor. *Phys. Rev. B.*, 57:15400, 1998.

[72] S. M. Cronenwett et al. Low-temperature fate of the 0.7 structure in a point contact: A Kondo-like correlated state in an open system. *Phys. Rev. Lett.*, 88:226805, 2002.

[73] S. M. Cronenwett. *Ph. D Thesis*. Harvard University, Harvard, 2001.

[74] G. B. Lesovik and L. S. Levitov. Noise in an ac biased junction: Nonstationary Aharonov – Bohm effect. *Phys. Rev. Lett.*, 72:538, 1994.

[75] M. H. Pedersen and M. Buttiker. Scattering theory of photon-assisted electron transport. *Phys. Rev. B.*, 58:13006, 1998.

[76] Madhu Thalakulam. *M. S Thesis*. Rice University, Houston, 2004.

[77] A. J. Rimberg et al. Real-time electron counting in semiconductor nano structures. *Proc. SPIE*, 5790:254, 2005.

[78] N. C. van der Vaart et al. Resonant tunneling through two discrete energy states. *Phys. Rev. Lett.*, 74:4702, 1995.

[79] W. Lu et al. Single-electron transistor strongly coupled to an electrostatically defined quantum dot. *Appl. Phys. Lett.*, 77:2746, 2000.